Stony Brook University

Threshold Resummation in Pair Production

A Dissertation Presented

by

Leandro Giordano Almeida

to

The Graduate School

in Partial Fulfillment of the Requirements

for the Degree of

Doctor of Philosophy

in

Physics

Stony Brook University

May 2010

Stony Brook University

The Graduate School

Leandro Giordano Almeida

We, the dissertation committee for the above candidate for the Doctor of Philosophy degree, hereby recommend acceptance of this dissertation.

George Sterman – Dissertation Advisor
Distinguished Professor, C. N. Yang Institute for Theoretical Physics

Abhay Deshpande – Chairperson of Defense
Professor, Department of Physics and Astronomy

Marivi Fernandez-Serra
Assistant Professor, Department of Physics and Astronomy

Amarjit Soni
Senior Scientist, Physics Department,
Brookhaven National Laboratory

This dissertation is accepted by the Graduate School.

Lawrence Martin
Dean of the Graduate School

Abstract of the Dissertation

Threshold Resummation in Pair Production

by

Leandro Giordano Almeida

Doctor of Philosophy

in

Physics

Stony Brook University

2010

In performing perturbative calculations in Quantum Chromodynamics, large logarithmic corrections can arise from processes involving soft and collinear quanta. These corrections can be resummed to all orders, allowing us to improve our control over cross section calculations associated with exclusive and inclusive processes. In this thesis, we show how such logarithmic corrections can appear in perturbative calculations in Quantum Chromodynamics. We then proceed to apply these resummation methods at next-to-leading logarithmic accuracy to heavy quark pair production and light hadron pair production. We show how to incorporate consistently cuts in rapidity and transverse momentum of the observed particles, together with resummation. This allows us to compare our next-to-leading logarithmic calculations directly to experiments by placing the precise experimental cuts associated with the measurements of these processes. We will also examine the phenomenological features associated with the logarithmic corrections. Specifically, we will look how we can apply this to the study jet mass distributions. We will compare jet mass distribu-

tion from jets initiated from light quarks to those initiated by top quarks. This will then allow us to build jet shape observables that will let us distinguish between the two.

Contents

List of Figures

List of Tables

Chapter 1

Introduction

1.1 QCD

Quantum Chromodynamics (QCD) provides a cornucopia of ideas on which is based our knowledge of hadronic physics. It gives a description of all hadronic matter in a picture of fermionic fields interacting through a $SU(3)$ gauge theory.

The idea that hadrons are bound states of localized objects was first introduced in an effort to explain the regularities associated with spectroscopy and decays of hadronic states [1]. Eventually, this lead to the concept of quarks as building blocks of hadrons, and it was christened "the quark model". Later this was augmented with the quantum number color [2]. The quark model gave a distinct understanding of the quantum numbers needed to describe hadronic matter. Hadrons were held together by the strong force, whose fundamental field was dubbed the gluon. Quarks are not observed as free particles, however, a property known as confinement.

A series of experiments, which scattered leptons off hadrons with large momentum transfer, were designed precisely to probe the substructure of nucleons. The subsequently observed phenomena were congruent with a description in terms of charged constituents of hadrons that behave as though essentially free at distances below the hadronic scale (see below.) This seemed at odds with the idea that quarks are confined.

Soon after, however, it was shown that $SU(3)$ gauge theories interacting with quark fields possess the property of asymptotic freedom, described below, which accounted for this behavior and contained the important features that describe strong interactions [3]. Though precise calculation of hadronic states are beyond the means of analytic computational methods, simulations based on lattice extensions of gauge theories have correctly calculated masses of the

light hadronic states [4]. They have also shown the correct properties of phase transition associated with confinement [5]. This theory constitutes what we call Quantum Chromodynamics.

Quantum Chromodynamics is summarized by the following SU(3) gauge invariant Lagrange density,

$$\mathcal{L} = \sum_{r}^{N_f} \bar{\psi}_i^r (i\gamma^\mu D_\mu^{ij} - \delta^{ij} m_r)\psi_j^r - \frac{1}{4} F_{\mu\nu}^a F^{\mu\nu a}, \tag{1.1}$$

and where the covariant derivative D_μ and the field strength $F_{\mu\nu}$ are given in terms of the gluon fields A_μ^a by

$$D_\mu^{ij} = \delta^{ij}\partial_\mu - i\, g_s\, T_{(f)}^{a,ij} A_\mu^a \quad F_{\mu\nu}^a = \partial_\mu A_\nu^a - \partial_\nu A_\mu^a - i\, g_s\, f^{abc}\, [A_{\mu,b}, A_{\nu,c}]\,. \tag{1.2}$$

Here we have color indices $i = 1, \ldots, N_c = 3$ for the quarks, $a = 1, \ldots, N_c^2 - 1$ for the gluons. The $T_{(f)}$ are generators for the gauge group in the fundamental representation, and f_{abc} are the generators in the adjoint representation. Thus the quarks are fermionic fields in the fundamental representation of the gauge group. The interaction among the fields is controlled universally by the coupling constant g_s, in terms of which we also define

$$\alpha_s = g_s^2/(4\,\pi). \tag{1.3}$$

This Lagrangian has, as noted previously, an $SU(3)$ gauge symmetry. It also has an approximate global $U(N_f)_{\mathrm{L+R}}$ symmetry which may be enlarged when the masses go to zero. We won't discuss flavour symmetries, which are beyond the scope of this thesis. All processes discussed from now on will be flavour universal, unless otherwise stated, except for dependence on the quark masses.

To develop perturbation theory, we must fix the gauge freedom. One way to do so is by choosing a physical gauge, by adding the following term to the Lagrange density,

$$\mathcal{L}_{\mathrm{gauge}} = -\frac{1}{2\xi}\,(n \cdot A^a)^2\,. \tag{1.4}$$

Here ξ denotes the gauge parameter and $n^2 > 0$, $n^2 < 0$, or $n^2 = 0$. We often use a gauge where $n^2 = 0$ and take the limit $\xi \to 0$. Starting with a path integral, one also needs to fix the measure associated with the functional integration. This leads to the inclusion of ghosts that ensure that physical observables are only affected by physical polarizations [6–9]. However, with a physical gauge there are no direct couplings between the ghosts and the physical fields, hence its name.

Another class of gauges, which is commonly used, is the covariant gauges. They are defined by the following term added to the Lagrange density:

$$\mathcal{L}_{\text{gauge}} = -\frac{1}{2\xi} \left(\partial \cdot A^a\right)^2 . \tag{1.5}$$

In this case, one needs to add new fields, which interact with the gluon through the density

$$\mathcal{L}_{\text{gh}} = \partial_\mu b_a \left(D^\mu_{ab}\right) c_b, \tag{1.6}$$

where c_b and b_a are the ghost and anti-ghost field respectively, and D^μ_{ab} is the covariant derivative defined in Eq. (1.2), in the adjoint representation.

Once we fix the gauge freedom in Eq. (1.1), with the term (1.4), or (1.5) and (1.6), we can obtain the diagrammatic rules for the perturbative expansion of QCD from the gauge fixed Lagrange density. The full list of such rules and how one properly obtains them from the action with the above Lagrange density can be found in [7].

1.2 Renormalization of Local Field Theories

The perturbative expansion of interacting quantum fields allows us to compute n-point Green functions of the associated fields order-by-order in α_s. One quickly finds, however, that the integrals that define these Green functions are divergent in 4-dimensional field theories. These divergences come in two varieties, short distance and long distance. Short distance divergences are from regions in momentum space where the momenta of virtual modes are large, and thus are called Ultraviolet (UV) divergences. Long distance divergences are usually associated with the low momentum regions of these virtual modes and therefore are called Infrared (IR) divergences. Their nature and presence will be discussed in Sec. 1.4. In this section, we will discuss UV divergences and sketch how to accommodate them.

At the tree level, UV divergences do not occur because of momentum conservation. At higher orders, however, there is extra freedom in the momenta of virtual modes. This leads individual diagrams to develop divergences that spoil the calculation of Green functions and physical observables. Removing these divergences from the theory is a process that goes by the name of renormalization, and can be summarized as a two step process.

First we make the diagrams finite by modifying the integrals, a procedure called regularization. One can, for example, cut off the momenta at some high scale, or put the theory on a lattice with a fixed spacing. Ideally, this should

be done in a manner that preserves the symmetries of the Lagrange density and that can be systematically applied at higher orders in α_s. The most common regularization for perturbation theory is dimensional regularization. In dimensional regularization one defines the Lagrange density in $d = 4 - 2\epsilon$ dimensions, and the UV divergences of the theory show up as poles in ϵ. Schematically, the results for different loops have the following UV pole structure:

$$\begin{aligned} \text{One loop:} \quad & \frac{B^{(1)}}{\epsilon} + A^{(1)}, \\ \text{Two loops:} \quad & \frac{C^{(2)}}{\epsilon^2} + \frac{B^{(2)}}{\epsilon} + A^{(2)}. \end{aligned} \tag{1.7}$$

For a detailed discussion see References [7–9] and references therein.

After regularization, one redefines the parameters and fields of the theory at a particular mass scale μ, to absorb these divergences. The finite terms (the A's in Eq. (1.7), that are absorbed by the renormalization, and the scale, at which scale this redefinition is performed are called the renormalization scheme and renormalization mass, respectively. Here we will focus on dimensional regularization. We will make use of the $\overline{\text{MS}}$ scheme [7, 8]. In this scheme, we absorb the ϵ poles in Eq. (1.7) and a factor of $\ln(4\pi/e^{\gamma_E})$ from the finite terms, with γ_E Euler's constant.

We say a theory is renormalizable if one can continue with this procedure order by order in α_s without introducing new parameters or local operators to the theory or inducing couplings between physical and unphysical modes, thus preserving unitarity. QCD and the other components of the Standard Model are renormalizable in this sense.

The new Lagrange density with the redefined parameters and fields is called the renormalized Lagrange density, $\mathcal{L}_R$, while the one before renormalization is called the Bare Lagrange density, $\mathcal{L}_0$. For the gauge fixed Lagrange density, we can write the renormalized Lagrange density by introducing a set of renormalization constants, Z_i, defined by:

$$\begin{array}{lll} A^a_{\mu,0} = \sqrt{Z_3} A^a_{\mu,R}, & c^a_0 = \sqrt{Z_3} c^a_R, & \psi_0 = \sqrt{Z_2}\psi_R \\ g_0 = Z_g g_R, & \xi_0 = Z_3 \xi_R, & m_0 = Z_m m_R. \end{array} \tag{1.8}$$

The quantities with the subscript 0 are bare, and those with R are renormalized. In the $\overline{\text{MS}}$ scheme, the renormalization constants depend only on g_R and ϵ. We will not use mass dependent schemes, a discussion of which can be found in [8]. One can show that with this minimal set of renormalization constants one can remove all divergences that appear in the gauge fixed Lagrange density, order-by-order in α_s (see [7–9] and citations therein for details of the proof.)

The renormalized coupling g_R in Eq. (1.8) depends on the renormalization scale, μ. We can determine this dependence or "running," as follows. First note that the action is dimensionless, thus the dimension of the Lagrange density is $[\mathcal{L}] = \text{mass}^d$. By inspection of our Lagrange density in Eq. (1.1), we find $[A] = \text{mass}$, $[\psi] = \text{mass}^{\frac{d-1}{2}}$ and $[g] = \text{mass}^{\epsilon}$ We replace the dimensionfull coupling by a dimensionless one, via

$$g_R \to g_R(\mu)\mu^{\epsilon}. \tag{1.9}$$

Given our definition of the renormalization constants, we have

$$g_R = \mu^{-\epsilon}\frac{g_0}{Z_g(g_R)}. \tag{1.10}$$

We can now define a function that summarizes the running of the coupling,

$$\begin{aligned}
\beta(g_R;\epsilon) &\equiv \frac{\mathrm{d}g_R}{\mathrm{d}\ln\mu} \\
&= \left(-\epsilon - \frac{\mathrm{d}\ln Z_g(g_R)}{\mathrm{d}\ln\mu}\right) g_R \\
&= -g_R\,\epsilon - \beta_0\frac{g_R^4}{(4\pi)^2} - \beta_1\frac{g_R^6}{(4\pi)^4} + \ldots
\end{aligned} \tag{1.11}$$

The coefficients of β_i can be obtained from the perturbative calculations of Z_g. The "β function" is known up to four loops [10] in QCD.

We can solve the differential equation in Eq. (1.11) with $\epsilon = 0$ to find the scale dependence of $g_R(\mu)$, which we give to two loop level in terms of $\alpha_s(\mu)$,

$$\begin{aligned}
\alpha_s(\mu) &= \frac{\alpha_s(\mu_0)}{\left(1+\frac{\beta_0}{2\pi}\alpha_s(\mu_0)\log\left(\frac{\mu}{\mu_0}\right)\right)}\left(1+\frac{1}{4\pi}\frac{\beta_1}{\beta_0}\frac{\alpha_s(\mu_0)}{\left(1+\frac{\beta_0}{(2\pi)}\alpha_s(\mu_0)\log\left(\frac{\mu}{\mu_0}\right)\right)}\right. \\
&\quad \left.\times\log\left(1+\frac{\beta_0}{2\pi}\alpha_s(\mu_0)\log\frac{\mu}{\mu_0}\right)\right) + \mathcal{O}\left(\alpha_s(\mu_0)^3\right).
\end{aligned} \tag{1.12}$$

The first two coefficients are given by,

$$\beta_0 = \left(\frac{11}{3}C_A - \frac{2}{3}N_f\right), \qquad \beta_1 = \frac{34}{3}C_A^2 - 2C_F N_f - \frac{10}{3}C_A N_f, \tag{1.13}$$

where $C_A = N_c = 3$, $C_F = (N_c^2-1)/(2N_c)$, and N_f represents the number of flavours with masses below the scales μ_0 and μ. Since β_0 and β_1 are positive (In the Standard Model the maximum $N_f = 6$), we have exactly the behavior

we expect from an asymptotically free theory: as we increase the scale the coupling decreases. We also learn at what scales perturbation theory is not applicable, because it is clear that if $\alpha_s(\mu)$ is close to 1, we can not expand in it.

1.3 Application of Perturbative QCD to Deep Inelastic Scattering

The fact that QCD is asymptotically free allows us to make practical use of perturbative field theory, particularly in scattering experiments where there is a large momentum transfer. Nonetheless, we are stuck with fact that quarks can only be found in nature within color singlet states, that is, they are confined. We believe that confinement comes from the low momentum scales (*i. e.* long distances), where asymptotic freedom does not help. Therefore any computation of scattering that we perform in QCD has to take into account that the observed initial and/or final states that participate in any scattering are hadrons, color singlet bound states of quarks and gluons.

Factorization theorems provide us with a framework with which to compute such cross sections. They allow to us to systematically separate long distance effects from short distance physics where perturbative QCD is applicable, *i. e.*, when there is a large momentum transfer. Long distance effects are associated with the infrared regime of the theory, and thus are not perturbatively calculable. These theorems separate such effects into non-perturbative functions that describe the distribution of partons in a hadron. Deep-inelastic scattering of leptons on hadrons is a good example to show how factorization occurs and to allow us to compute cross sections for such processes.

Deep-inelastic scattering is illustrated by the following process,

$$l(k) + H(P) \to l(k') + X(P_X), \tag{1.14}$$

where l is a lepton with incoming and outgoing momenta k and k' respectively, and H is some specific initial hadronic state with momentum P, usually a nucleon. X represents any of a multitude of hadronic final states with a total invariant mass of $P_X^2 = M_X^2 \gg M_H$, where M_H is the mass of the initial hadrons. For charged leptons both electromagnetic (EM) and weak interactions are possible. In the EM case, Quantum Electrodynamics at the lowest order, $\mathcal{O}(\alpha_{\rm em})$, is a good approximation. The differential cross section

for such process at α_{em} is proportional to

$$\begin{aligned}
2\omega_k \frac{d\sigma}{d^3k'} &= \frac{\alpha_{em}^2}{s}\sum_X \int_{-\infty}^{\infty} d^4x \int_{-\infty}^{\infty} d^4y\, e^{-i(k-k')\cdot y} e^{-i(P-P_X)\cdot x} \\
&\quad \times |\, \langle\, l^{\pm}(k), H(P)\,|\, J_{lep}^{em,\mu}(y) A_{\mu}^{\rm em}(y) A_{\nu}^{\rm em}(x) J_{had}^{em,\nu}(x)\,|\, l^{\pm}(k'), X(P_X)\,\rangle\,|^2 \\
&= -\frac{\alpha_{em}^2}{s(q^2)^2}\sum_X g_{\mu\nu} \int_{-\infty}^{\infty} d^4x \int_{-\infty}^{\infty} d^4y\, e^{-i(k-k')\cdot y} e^{-i(P-P_X)\cdot x} \\
&\quad \times |\, \langle\, l^{\pm}(k)|J_{lep}^{em,\mu}(x)|l^{\pm}(k')\,\rangle\,|\, \langle\, H(P)\,|\, J_{had}^{em,\nu}(y)\,|\, X(M_X^2)\,\rangle\,|^2 \\
&= -\frac{\alpha_{em}^2}{s(q^2)^2} L^{\nu\mu}(k,k') W_{\nu\mu}(Q,P), \qquad (1.15)
\end{aligned}$$

where $A_{\mu}^{\rm em}$ are the photon gauge fields and $J_{lep}^{em,\mu}(x)$ and $J_{had}^{em,\nu}(x)$ are the electromagnetic currents for the leptons and for the quarks, respectively. We define $L_{lep}^{\mu\beta}$ to be the leptonic tensor representing the matrix element for two leptonic currents and similarly $W^{\mu\rho}$ to be the hadronic tensor. The leptonic matrix elements can be calculated reliably in QED. We can extract the hadronic tensor from the above and sum over the hadronic final states, giving

$$W^{\mu\rho}(Q,P) = \frac{1}{4\pi}\int d^4y \mathrm{e}^{iq\cdot y}\,\langle\, H\,|J_{had}^{em,\mu}(y)\, J_{had}^{em,\rho}(0)\,|\, H\,\rangle\,. \qquad (1.16)$$

The factorization theorem for this process states that for large $Q^2 = -q^2$, the hadronic tensor can be written as

$$W^{\mu\nu} = \sum_a \int_x^1 \frac{d\xi}{\xi} f_{a/H}(\xi,\mu_F) C_a^{\mu\nu}(\xi/x, Q, \mu, \mu_F, \alpha_s(\mu)) + \mathcal{O}(Q^{-2}), \qquad (1.17)$$

where $f_{a/H}$ is the distribution of parton a in hadron H, with momenta ξP, and where C_a describes the perturbative short-distance corrections to the electromagnetic current. The scale μ_F, represents the scale at which $f_{a/H}$ is defined.

Corrections to the above factorization are suppressed by powers of Q^2. Note the sum over partons a, since a hadron is constituted not only of its valence quarks but also of quark and anti-quark pairs and of the gauge field quanta themselves. Thus the sum includes $a = \{$quarks, anti-quarks, gluons$\}$, and if we reach high enough momentum transfers, then even heavy quarks, like the charm, must be included in the initial state [11]. This is exactly the kind of factorization of momentum scales we hope to achieve in general, and indeed such factorization theorems have been proven and tested in a multitude of processes [12]. We now turn to a discussion of the nature of factorization proofs.

1.4 Factorization

As discussed in the previous section, the statement of factorization reduces to the assertion that we can separate long distance (non-perturbative) from short distance (perturbative) physics in a manner in which they are incoherent. Specifically one would like to prove that this factorization is possible order-by-order in α_s. Though we will not prove such factorization in detail here, we will try to provide the necessary steps to understand how this is done.

In order to proceed, one would like to understand the role of momentum regions in scattering processes. More specifically, we would like to understand the nature of IR divergences, since they are closely related with the infrared sector of momentum space, and thus non-perturbative physics. In this section we follow closely [7, 13].

1.4.1 The Nature of Infrared Divergences

In general a Green function for external particles with momenta $\{p_j\}$ can be written in the form,

$$G(\{p_j\}) = \prod_{r=1}^{loops} \int d^n k_r \prod_{i=1}^{lines} \left(\left(l_i^2 - m_i^2 + i\epsilon \right)^2 \right)^{-1} N(k_r, p_j) \qquad (1.18)$$

where N represents the numerator momentum structure. Each line carries a momenta l_i and mass m_i. Applying Feynman parameterization,

$$\begin{aligned} \prod_{i=1}^{N} A_i^{-a_i} &= \left(\prod_{j=1}^{N} \frac{1}{\Gamma[a_j]} \right) \Gamma \left[\sum_{f=1}^{N} a_f \right] \prod_{i=1}^{N} \int d\alpha_i \, \alpha_i^{a_i - 1} \\ &\quad \times \delta \left(1 - \sum_{r}^{N} \alpha_r \right) \left(\sum_{b=1}^{N} \alpha_b A_b \right)^{-\sum_{c=1}^{N} a_c}, \end{aligned} \qquad (1.19)$$

leads to the following form for the Green function,

$$G(\{p_j\}) = \prod_{i}^{lines} \int_0^1 d\alpha_i \delta(\sum_i \alpha_i - 1) \prod_{r}^{loops} \int d^n k_r \frac{N(k_r, p_j)}{D(\alpha_i, p_j, k_r)^{-lines}}. \qquad (1.20)$$

Here the function D combines the denominator momentum structure. It is given by

$$D(\alpha_k, k_l, p_i) = \sum_{j}^{lines} \alpha_j \left[l_j^2(k,p) - m_j^2 \right] + i\epsilon, \tag{1.21}$$

where l_j represents the momemtum of line j.

Infrared divergences in a Feynman diagram are possible when its integrand is singular. We therefore concern ourselves with the zeros of Eq. (1.21). Since the integrand is, however, an analytic function of its parameters, this is not a sufficient condition. We can simply deform the contours in Eq. (1.20) associated with the loop momentum integration, to bypass such poles if they are isolated in the complex momentum plane or in α_i.

There are two instances in which contour deformation may not be possible: first, when the pole coincides with the end point of the contour integration, and second, when multiple poles coalesce and pinch the contour. We can easily find when the momenta are pinched because Eq. (1.21) is always quadratic in the loop momenta. The following conditions are necessary for a pinch to occur,

$$D(\alpha_i, k_\mu, p_r) = 0, \qquad \frac{\partial}{\partial k^\mu} D(\alpha_i, k_\mu, p_r) = 0. \tag{1.22}$$

These two conditions are summarized by the Landau equations :

$$\begin{array}{c} \text{either } \ \alpha_j = 0 \quad \text{ or } \quad l_j^2 = m_j^2, \\ \text{and } \ \sum_j \epsilon_{jm} \alpha_j l_j^\mu(k,p) = 0, \end{array} \tag{1.23}$$

where j runs over all on-shell lines within each loop, and ϵ_{jm} is either 1 or -1 depending whether the loop momentum m is flowing with or against the momentum of line j. The solutions that satisfy Eqs. (1.23) are characterized by sets $\{\alpha, k\}$. These points form surfaces in $\alpha - k$ space referred to as a pinch surface.

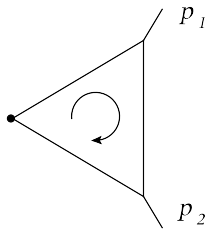

Figure 1.1: Scalar Triangle

As an example, we analyze the triangle diagram in a generic scalar theory, Figure 1.1. It is summarized by the following integral,

$$\int \frac{d^d k}{(2\pi)^d} \frac{1}{(k^2+i\epsilon)((k+p_1)^2+i\epsilon)((k-p_2)^2+i\epsilon)}. \tag{1.24}$$

The Landau equations corresponding to Eqs (1.23) for this integral are:

$$\begin{aligned} \alpha_1 k^2 + \alpha_2 (k+p_1)^2 + \alpha_3 (k-p_2)^2 + i\epsilon &= 0, \\ \alpha_1 k^\mu + \alpha_2 (k+p_1)^\mu + \alpha_3 (k-p_2)^\mu &= 0. \end{aligned}$$

These relations have the following non-trivial solutions:

$$\begin{array}{ll} k^\mu = 0 & \alpha_2 = \alpha_3 = 0, \\ k = y p_2 & \alpha_2 = 0 \text{ and } \alpha_1 = -\alpha_3 \frac{(1-y)}{y}, \\ k = y p_1 & \alpha_3 = 0 \text{ and } \alpha_1 = \alpha_2 \frac{(1+y)}{y}. \end{array} \tag{1.25}$$

These solutions separate the pinch surfaces into three distinct regions of momentum space, the soft region, where the all components of the loop momenta go to zero, and two collinear regions, where the loop momenta are proportional to one of the outgoing momenta.

The pinch surfaces corresponding to eqs. (1.25) can be described by a reduced diagram where off-shell propagators are shrunk to points. As observed by Coleman and Norton [16], each of these reduced diagrams describes a physical process, where the left over propagators describe the propagation of free, physical particles. With this nice physical picture we can often write the most general reduced diagrams for a scattering process.

The set of such diagrams is particularly simple for DIS and related processes [14, 15]. We will generally denote a collinear or "jet" subdiagram as J and soft subdiagrams as S. The possible pinch surfaces associated with the DIS process are shown in Figure 1.2, where H represents the hard coefficient where all momenta is off-shell by at least Q^2. The J_i's represent the collinear pinch surfaces associated with final state hadrons in X and are connected to other J_i's and H by finite-energy on-shell particles. Finally, the region S represents the soft gluons ,and quark loops, and can connect to the collinear regions and possibly the hard scattering. The physical picture here presents a initial Hadron with momentum P producing a jet collinear to it, J_1. We can also have an arbitrary number of jets J_i emerging from the scattering. The jets can be connected by an arbitrary number of soft gluons, S.

Next we would like to bound the integrals near the pinch surfaces to see their potency and thus find the regions of momentum that will produce leading

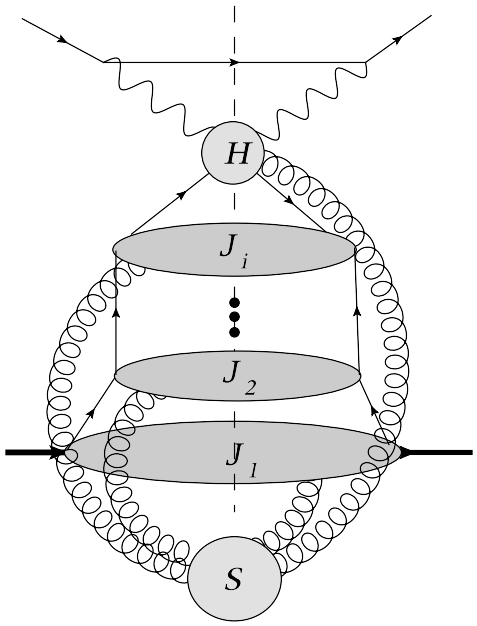

Figure 1.2: General pinch surfaces associate with the process of Eq. (1.14).

contributions in scattering amplitudes.

1.4.2 IR Power Counting

Now the above conditions above for infrared divergences are simply necessary conditions. The potential divergence of a diagram may be much smoother than anticipated. Therefore, it is possible after integration through the pinch surfaces no large contributions may be found. It is always possible that the diagrams unphysical modes lead to unphysical poles, which cancel in a gauge invariant sum of diagrams.

Infrared power counting [14], will lead to an estimate of the degree of divergence of a particular diagram. We will determine the behavior of the reduced diagrams' momentum integrals for both internal and external states as they approach the pinch surfaces.

One way to determine this behavior is to make the integrands, associated with the diagram, homogenous functions of variables that vanish at the pinch surface. We refer to this variables are the "normal" variables of the pinch surface. Let $\{\kappa\}$ denote the normal variables to the pinch surface and $\{l\}$ the remaining "instrinsic" variables that parametrize the pinch surface. A general

Green function near a pinch surface γ is then given by

$$G_\gamma(Q) = \int_\gamma \prod_{b=1} dl_b \int_\gamma \prod_{a=1}^{D_\gamma} d\kappa_a \frac{N(\kappa_a, l_b, Q)}{D(\kappa_a, l_b, Q)}, \tag{1.26}$$

where l represents the intrinsic variables while κ represents the normal variables. The numerator polynomials which depend on the intrinsic and normal variables and on the general physical scale Q, is given N, similarly D is the denominator associated with propagators of the fields present in the diagram. The parameter D_γ represents the number of normal variables. By scaling the normal variables by a parameter λ, such that $\kappa_b = \lambda_\gamma \kappa'_b$, we insert unity in the Green function in Eq. (1.26),

$$\int_0^{\lambda^2_{max}} \frac{d\lambda_\gamma^2}{\lambda_\gamma^2} \delta \left(1 - \sum_{a=1}^{D_\gamma} \kappa_a^{'2} \right) = 1. \tag{1.27}$$

Under this scaling, the numerator and denominators will have some dominant terms in the limit of $\lambda \to 0$. These terms have the following powers

$$N(\kappa_a, l_b, Q) = \lambda_\gamma^n \left[\bar{N}(\kappa'_a, l_b, Q) + \mathcal{O}(\lambda_\gamma) \right] \tag{1.28}$$

$$D(\kappa_a, l_b, Q) = \lambda_\gamma^d \left[\bar{D}(\kappa'_a, l_b, Q) + \mathcal{O}(\lambda_\gamma) \right] \tag{1.29}$$

The power behavior of the integral at the pinch surface is then given by

$$G_\gamma = \int_0^{\lambda_{max}} d\lambda_\gamma \frac{1}{\lambda_\gamma^{p_\gamma}} \Delta_\gamma(\kappa'_a, l_b, Q) \tag{1.30}$$

where p_γ ,

$$p_\gamma = d + 1 - D_\gamma - n, \tag{1.31}$$

such that for $p_\gamma = 1$ the integrals J is logarithmic divergent, and Δ_γ is the rest of the integrand from Eq. (1.26) where the numerator and denominator polynomials only have the terms with the leading dependence in λ_γ, *i. e.*, the first terms in Eqs. (1.28) and (1.29). Now we could in principle find additional pinch surfaces in Δ_γ, if these are among the original set of pinch surfaces then we can bound it eventually on with this basis of pinch surfaces. We can then bound the entire integral through this method.

Therefore we can build cross-sections that, though are not free of pinch surfaces, are defined in such a way that the pinch surfaces are not strong enough to produce IR poles.

One can then obtain the power of the leading contribution to the physical process, and show that in properly defined observables, the worst divergences are logarithmic. In the next chapter we will show how these leading regions, can lead to the resummation of logarithmic corrections.

Chapter 2

Threshold Resummation

2.1 Resummation from Factorization

In this chapter we will discuss how resummation of many logarithmic corrections is possible. We will follow closely to the discussions of Refs. [13, 18, 19]. The connection between resummation and factorization is analogous to the renormalization group properties of physical cross sections.

For example, a general unrenormalized Green function of n fields ψ_0, is related to the renormalized Green function with n fields ψ_R by

$$G_0(p_i, g_0) = (Z_\psi^{1/2}(g_R(\mu).\epsilon))^n G_{\rm ren}(p_i, \mu, g_R(\mu)), \tag{2.1}$$

where μ_R is the renormalization scale. Given that $\mathcal{L}_0$ does not depend on the renormalization scale, the unrenormalized Green functions should also be independent it. This leads to following equation

$$\frac{d\ln G_{\rm ren}}{d\ln \mu_R} = -n\,\gamma_\psi(g_R(\mu_R)), \tag{2.2}$$

where γ_ψ are the anomalous dimensions of the fields ψ

$$\gamma_\psi \;=\; \frac{1}{2}\frac{d\ln Z_\psi}{d\ln \mu_R}. \tag{2.3}$$

Since in an $\overline{\rm MS}$ scheme

$$\mu\frac{d}{d\mu} = \mu\frac{\partial}{\partial\mu} + \beta(\alpha_s)\,\frac{\partial}{\partial\alpha_s}, \tag{2.4}$$

and Z_ψ depends on μ only through $\alpha_s(\mu)$, we have

$$\gamma_\psi = \frac{1}{2}\beta(\alpha_s)\frac{\partial \ln Z_\psi}{\partial \alpha_s}. \tag{2.5}$$

Combining this reasoning with the observation that a physical cross section should be independent of the factorization scale, we can obtain a similar relation for the deep-inelastic scattering cross section.

Consider the hadronic tensor in Eq. (1.17). For simplicity we suppress Lorentz indices and the sum over parton types. Integrating Eq. (1.17) with the following moment, and choosing $\mu_F = \mu_R = \mu$, gives

$$\begin{aligned} \tilde{W}(N, Q^2) &= \int_0^1 dx x^{N-1} W(x, Q^2) \\ &= \tilde{f}(N, \alpha_s(\mu), \mu)\tilde{C}(N, \mu, \alpha_s(\mu), Q^2). \end{aligned} \tag{2.6}$$

Since $\tilde{W}$ is a physical observable, it is independent of μ, and we find the following consistency equations for $\tilde{C}$ and $\tilde{f}$,

$$\left(\mu_F \frac{d}{d\mu} - \gamma_N(\alpha_s)\right) \ln \tilde{C} = 0, \tag{2.7}$$

$$\left(\mu_F \frac{d}{d\mu} + \gamma_N(\alpha_s)\right) \ln \tilde{f} = 0. \tag{2.8}$$

The anomalous dimension $\gamma_N(\alpha_s)$ can depend only on N and g_R because these are the only variables on which C and f share in common. We will proceed to show how such derivations, in more exclusive observables with more physical scales, lead to the resummation of logarithmic corrections in these exclusive cross sections.

2.2 Logarithmic Corrections

Physical cross section can be factorized into different regions of momentum space as described in Section 1.4. This allows us to give the leading contributions to the cross section by convolutions of functions associated with the corresponding momentum regions. This factorization is well illustrated for Drell-Yan scattering

$$H_A(P_A) + H_B(P_B) \to \gamma^*(Q^2) \tag{2.9}$$

where H_A and H_B are the two hadrons with momenta P_A and P_B respectively, and γ^* is an off-shell singlet gauge boson with an invariant mass Q^2. The factorization is given by the following convolution

$$\begin{aligned}\frac{d\sigma_{H_1\,H_2\to\gamma^*}}{dQ^2} &= \sum_{a,b}\int dx_1\,dx_2\; f_{a/H_1}(x_1,\mu_F,\alpha_s(\mu_R)) \\ &\qquad \times f_{b/H_2}(x_2,\mu_F,\alpha_s(\mu_R))\frac{d\hat{\sigma}_{a\,b\to\gamma^*}}{dQ^2}(\hat{\tau},Q^2/\mu,\hat{s}/\mu\alpha_s(\mu_R)), \\ &= \int_\tau^1 d\hat{\tau}\int dx_1\,dx_2\; f_{a/H_1}(x_1,\mu_F,\alpha_s(\mu_R))\, f_{b/H_2}(x_2,\mu_F,\alpha_s(\mu_R)) \\ &\quad \times\frac{d\hat{\sigma}}{dQ^2}(\hat{\tau})\delta(x_1x_2-\hat{\tau}),\end{aligned} \tag{2.10}$$

where $\hat{s}=x_1x_2S$, $\tau=Q^2/S$ and $\hat{\tau}=Q^2/\hat{s}$. The parton distribution functions are "universal", *i. e.*, the same as in Eq. (1.17) for DIS.

The cross section $d\hat{\sigma}/dQ^2$ in Eq. (2.10) is infrared safe, but for $\hat{\tau}\to 1$ there is no phase space for gluon radiation into the final state. This mis-cancellation shows up in "plus distributions," which occur in $d\hat{\sigma}/dQ^2$ as terms like

$$\alpha_s^k\left[\frac{\ln^l(1-\hat{\tau})}{(1-\hat{\tau})}\right]_+, \tag{2.11}$$

where $0\le l\le 2k-1$, and where $[f(x)]_+$ is defined by,

$$\int_0^1 dx[f(x)]_+g(x)=\int_0^1 f(x)(g(x)-g(0)). \tag{2.12}$$

Therefore, the logarithmic plus distribution in Eq. (2.11), though large, are still finite when integrated with smooth functions, like the parton distribution functions. The limit $\hat{\tau}\to 1$ is called partonic threshold. This threshold $\hat{\tau}=1$ is always present even when $\tau\ll 1$. These threshold enhanced logarithmic contributions are the one we will be resumming.

2.3 Threshold Resummation of Drell Yan

We will proceed to give a view of resummation from the point of view of Drell-Yan Scattering. In this process we can identify a "weight function", which measures the distance to partonic threshold,

$$w=1-\frac{Q^2}{\hat{s}}\equiv 1-\hat{\tau}. \tag{2.13}$$

As above Q^2 is the mass of the off-shell electroweak boson produced, and $\hat{s} = (x_a P_A + x_b P_B)^2$. Thus as $w \to 0$, we approach the threshold limit. We note again that even when $Q^2 \ll (P_A + P_B)^2$, we always encounter parton threshold in the factorized cross section (2.10).

Consider a specific contribution to $d\hat{\sigma}/dQ^2$ with n partons in the final state with momenta k_i. The phase space for this process has the following delta function, which fixes the mass of the Drell-Yan pair,

$$\delta\left(Q^2 - \left(p_1 + p_2 - \sum_i k_i\right)^2\right). \tag{2.14}$$

In the threshold limit this becomes,

$$\delta\left(s(1-\hat{\tau}) + 2\sqrt{s}\left(\sum_{i=1}^{n} k_i^0\right) + \mathcal{O}\left((1-\hat{\tau})^2\right)\right). \tag{2.15}$$

Therefore the phase space is defined completely by the energy of the partons in the final states. The partonic cross section for this process is given by the following re-factorization, whose leading regions are shown in Figure 2.1,

$$\begin{aligned}\hat{\sigma}(w) &= H(p_1, p_2, \mu, \mu, \xi_i) \int \frac{dw_{J_1}}{w_{J_1}} \frac{dw_{J_2}}{w_{J_2}} \frac{dw_s}{w_s} \\ &\quad \times J_1(p_1 \cdot \xi_1/\mu, w_{J_1}(Q/\mu), \alpha_s(\mu))\ J_2(p_2 \cdot \xi_2/\mu, w_{J_2}(Q/\mu), \alpha_s(\mu)) \\ &\quad \times S(w_s Q/\mu, v_i, \xi_i, \alpha_s(\mu))\ \delta(w - w_{J_1} - w_{J_2} - w_s).\end{aligned} \tag{2.16}$$

Corrections to this expression vanish as powers of w. The arbitrary vectors ξ_i are used to define the matrix elements for jet functions and soft functions [20], analogous to the factorization scale in Eq. (1.17) for DIS. The convolution in Eq. (2.16) can be decomposed by taking its Laplace transform with respect to the weight w, analogously to the Mellin moment for DIS, Eq. (2.6),

$$\begin{aligned}\tilde{\sigma}_N = \int_0^\infty dw e^{-N w} &= H(p_1, p_2, \xi_i)\ \tilde{S}(Q/(\mu N), v_i, \xi_i, \alpha_s(\mu)) \\ &\quad \times \tilde{J}_1(p_1 \cdot \xi_1/\mu, Q/(\mu N), \alpha_s(\mu)) \\ &\quad \times \tilde{J}_2(p_2 \cdot \xi_2/\mu, Q/(\mu N), \alpha_s(\mu)),\end{aligned} \tag{2.17}$$

where N can be complex. The threshold behavior is now indicated by the limit of large N (large $(1-\hat{\tau})$ corrections are highly suppressed at large N).

Each of the functions in Eq. (2.17) needs to be renormalized and as in

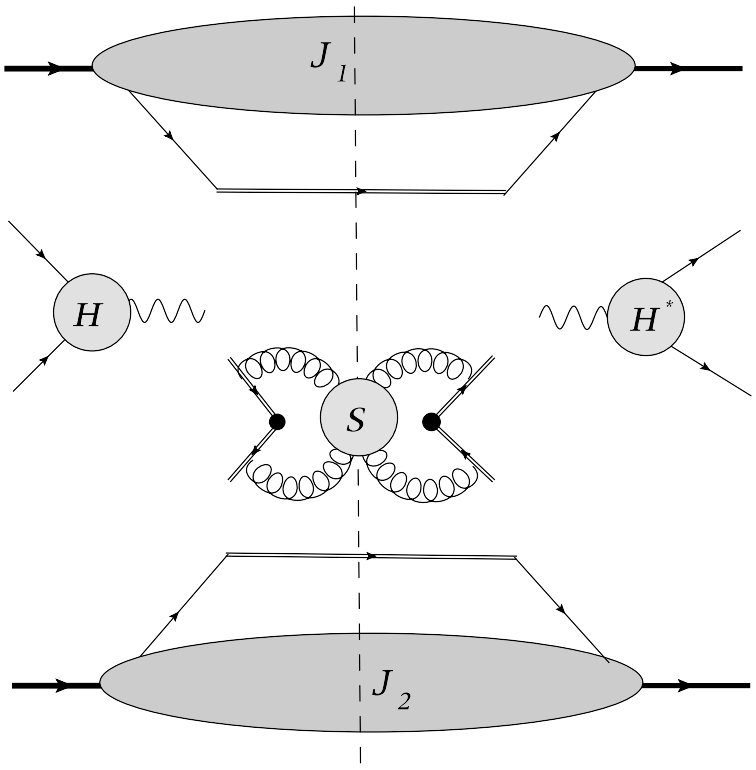

Figure 2.1: Factorization for Drell-Yan Scattering

Eq. (2.2), we have

$$\begin{aligned}\frac{d\ln H}{d\ln\mu} &= -\gamma_H(\alpha_s),\\ \frac{d\ln \tilde{J}_i}{d\ln\mu} &= -\gamma_{J_i}(\alpha_s),\\ \frac{d\ln \tilde{S}}{d\ln\mu} &= -\gamma_S(\alpha_s).\end{aligned} \tag{2.18}$$

Since the physical cross section is independent of the renormalization scale, these anomalous dimensions are related [17, 18, 20] by

$$\gamma_H + \gamma_S + \sum_{i=1}^{2}\gamma_{J_i} = 0. \tag{2.19}$$

The scheme we use to perform the factorization, and therefore the directions we pick for the vectors ξ_i, should not affect the physical cross section. We can then impose two extra constraints,

$$\begin{aligned}\left(p_1\cdot\xi_1\frac{\partial}{\partial p_1\cdot\xi_1}H\right)\tilde{J}_1\tilde{J}_2\tilde{S} \;+\; & H\left(p_1\cdot\xi_1\frac{\partial}{\partial p_1\cdot\xi_1}\tilde{J}_1\right)\tilde{J}_2\tilde{S}\\ & + H\tilde{J}_1\tilde{J}_2\left(p_1\cdot\xi_1\frac{\partial}{\partial p_1\cdot\xi_1}\tilde{S}\right) = 0,\end{aligned} \tag{2.20}$$

and similarly for ξ_2. Diving Eq. (2.20) by $H\tilde{J}_1\tilde{J}_2\tilde{S}$, we find

$$p_1\cdot\xi_1\frac{\partial}{\partial p_1\cdot\xi_1}\ln\tilde{J}_1 = \underbrace{-p_1\cdot\xi_1\frac{\partial}{\partial p_1\cdot\xi_1}\ln H}_{G}\underbrace{-p_1\cdot\xi_1\frac{\partial}{\partial p_1\cdot\xi_1}\ln\tilde{S}}_{K}, \tag{2.21}$$

and similarly for J_2. Since the anomalous dimensions of the J's depend only on α_s,

$$\frac{d}{d\ln\mu}\left(G\left(p_1\cdot\xi_1/\mu,\mu_F,\alpha_s(\mu^2)\right)+K\left(Q'_{a_1}/N,\mu,\alpha_s(\mu^2)\right)\right) = \frac{d}{d\ln p_1\cdot\xi_1}\gamma_{J_1}(\alpha_s) = 0 \tag{2.22}$$

Separation of variables in this equation then leads to

$$\begin{aligned} \frac{d}{d\ln\mu}\ln K &= -\gamma_K(\alpha_s), \\ \frac{d}{d\ln\mu}\ln G &= \gamma_K(\alpha_s). \end{aligned} \tag{2.23}$$

Solving these two equation leads to the following relation for $K+G$:

$$\begin{aligned} & G\left(p_1\cdot\xi_1,\mu,\mu,\alpha_s(\mu^2)\right) + K\left(Q'_{a_1}/N,\mu,\alpha_s(\mu^2)\right) \\ &= -\int_{Q_{a_1}/N}^{p_1\cdot\xi_1}\frac{d\mu'}{\mu'}\underbrace{\left(\gamma_K(\alpha_s(\mu')) + \beta(\alpha_s)\frac{\partial}{\partial\alpha_s}K(1,\alpha_s(\mu'))\right)}_{A(\alpha_s)} \\ &+ \underbrace{K(1,\alpha_s(p_1\cdot\xi_1)) + G(1,\alpha_s(p_1\cdot\xi_1))}_{A'(\alpha_s)} \\ = & -\int_{Q_{a_1}/N}^{p_1\cdot\xi_1}\frac{d\mu'}{\mu'}A(\alpha_s(\mu'^2)) + A'(\alpha_s((p_1\cdot\xi_1)^2)). \end{aligned} \tag{2.24}$$

Now using Eq. (2.24) to solve Eq. (2.21) together with (2.18) for the jet functions,

$$\begin{aligned} \tilde{J}(p_1\cdot\xi_1, Q/(\mu N),\alpha_s(\mu^2)) &= \tilde{J}(1,1,\alpha_s(Q^2/N^{2/a}))\exp\left[-\int_{Q/N}^{\mu}\frac{d\lambda}{\lambda}\gamma_{J_1}(\alpha_s(\lambda^2))\right]. \\ & \exp\left[-\int_{Q/N}^{p\cdot\xi}\frac{d\lambda}{\lambda}\left(\int_{Q/N}^{\lambda}\frac{d\xi}{\xi}A(\alpha_s(\xi^2)) - A'(\alpha_s(\lambda^2))\right)\right] \end{aligned} \tag{2.25}$$

Putting everything together, and setting $p\cdot\xi = Q$, gives the following resummed cross section for Drell-Yan in transform space.

$$\begin{aligned} \tilde{\sigma}_N &= \ln H(1,1,\alpha_s(Q)) + \ln S(1,1,\alpha_s(Q/N)) \\ &+ \sum_{i=1,2}\ln\tilde{J}_i(1,1,\alpha_s(Q/N)) - \int_Q^{Q/N}\frac{d\lambda}{\lambda}\gamma_S(\alpha_s(\lambda^2)) \\ &-2\int_{Q/N}^{Q}\frac{d\xi}{\xi}\left\{\ln\frac{Q}{\xi}A(\alpha_s(\xi^2)) - A'(\alpha_s(\xi^2)) + \sum_j\gamma_{J_j}(\alpha_s(\xi^2))\right\}. \end{aligned} \tag{2.26}$$

Expanding the above form to one loop in α_s, where $A(\alpha_s) = \alpha_s A^{(1)} + \ldots$, we

see that we have exponentiated the following logarithms,

$$\ln \tilde{\sigma}_N = \cdots + \alpha_s \left\{ 2B^{(1)} \ln N + A^{(1)} \ln^2 N + \dots \right\}. \tag{2.27}$$

These correspond precisely to the leading and next-to leading logarithms of threshold resummation in the Drell-Yan cross section. The inversion back to $\hat{\tau}$ space will be shown in subsequent chapters. Here we only note that the inverses of logarithms of N are "plus distributions" of Eq. (2.11).

2.4 Resummation of QCD Hard Scattering

For processes that involve color exchange, we use a more general factorization form for the cross section,

$$\tilde{\sigma} = \sum_{IJ} H_{IJ} \, \tilde{S}_{IJ} \, \prod_i \tilde{J}_i \tag{2.28}$$

where the indices I and J label the color structure in a manner described below. The J_i may correspond to initial and/or final collinear radiation. Thus for process involving heavy quarks, we will only need two initial-state jet factors, since final state heavy quark propagators do not involve collinear divergences. The functional dependence of the above functions on the kinematics and scales is the same as for Drell-Yan. As previously, the physical cross section is independent of the renormalization scale, and this leads to the corresponding renormalization group equations

$$\begin{aligned} \mu \frac{d}{d\mu} \ln H_{IJ} &= -(\Gamma_H(\alpha_s))_{IJ}, \\ \mu \frac{d}{d\mu} \ln S_{IJ} &= -(\Gamma_S(\alpha_s))_{IJ}, \\ \mu \frac{d}{d\mu} \ln J_i &= -\gamma_{J_i}(\alpha_s), \end{aligned} \tag{2.29}$$

where now the anomalous dimensions for the soft and hard functions are dependent on the color structure of the process. We can go through the same analysis as in the previous section, leading to similar exponentiation of the logarithms involved, with the additional constraint of keeping the color ordering intact. The details can be found in [20].

2.4.1 Outline for Thesis

We will now proceed to study the effects of threshold resummation and logarithmic corrections in different processes and observables. This is based in the following published work [22–25]. The rest of this thesis is organized as follows: In Chapter 3 we will discuss the resummation for the exclusive production of two final state light hadrons. We look at the effects of next-leading-logarithm (NLL) resummation in more exclusive observables. This will allow us to compare these results to specific experiments that have measured these correlations. In Chapter 4, we will proceed to the production of heavy quarks at $p\bar{p}$ collider. Specifically, we will look at the effects of threshold resummation at NLL on the Forward Backward asymmetry in $t\bar{t}$ production. We will then proceed to a systematic understanding of high invariant jet mass distributions at the LHC in Chapter 5, whose main contribution comes from logarithmic corrections. This study will allow us to develop jet observables to distinguish light quark jets from heavy parton jets, the subject of which is discussed in Chapter 6.

Chapter 3

Dihadron Production

3.1 Introduction

Cross sections for hadron production in hadronic collisions play an important role in QCD. They offer a variety of insights into strong interaction dynamics. At sufficiently large momentum transfer in the reaction, QCD perturbation theory can be used to derive predictions. The cross section may be factorized at leading power in the hard scale into convolutions of long-distance factors representing the structure of the initial hadrons and the fragmentation of the final-state partons into the observed hadrons, and parts that are short-distance and describe the hard interactions of the partons. If the parton distribution functions and fragmentation functions are known from other processes, especially deeply-inelastic scattering and e^+e^- annihilation, hadron production in hadronic collisions directly tests the factorized perturbative-QCD approach and the relevance of higher orders in the perturbative expansion.

Much emphasis in both theory and experiment has been on single-inclusive hadron production, $H_1H_2 \to hX$ [26–33]. Here the large momentum transfer is provided by the high transverse momentum of the observed hadron. Of equal importance, albeit explored to a somewhat lesser extent, is di-hadron production, $H_1H_2 \to h_1h_2X$, when the pair is produced with large invariant mass M. In many ways, one may think of this process as a generalization of the Drell-Yan process to a completely hadronic situation, with the Drell-Yan lepton pair replaced by the hadron pair. The process is therefore particularly interesting for studying QCD dynamics, as we shall also see throughout this paper. Experimental data for di-hadron production as a function of pair mass are available from various fixed-target experiments [34–36], as well as from the ISR [37]. On the theory side, next-to-leading order (NLO) calculations for this process are available [38–40]. They have been confronted with the available

data sets, and it was found that overall agreement could only be achieved when rather small renormalization and factorizations scales were chosen. The NLO calculations in fact show very large scale dependence. If more natural scales are chosen, NLO theory significantly underpredicts the cross section data, as we shall also confirm below.

In the present chapter, we investigate the all-order resummation of large logarithmic corrections to the partonic cross sections. This is of considerable interest for the comparison between data and the NLO calculation just described. A related resummation for the single-inclusive hadron cross section [30] was found to lead to significant enhancements of the predicted cross section over NLO, in much better overall agreement with the available data in that case.

At partonic threshold, when the initial partons have just enough energy to produce two partons with high invariant pair mass (which subsequently fragment into the observed hadron pair), the phase space available for gluon bremsstrahlung vanishes, resulting in large logarithmic corrections. To be more specific, if we consider the cross section as a function of the partonic pair mass $\hat{m}$, the partonic threshold is reached when $\hat{s} = \hat{m}^2$, that is, $\hat{\tau} \equiv \hat{m}^2/\hat{s} = 1$, where $\sqrt{\hat{s}}$ is the partonic center-of-mass system (c.m.s.) energy. The leading large contributions near threshold arise as $\alpha_s^k \left[\ln^{2k-1}(1-\hat{\tau})/(1-\hat{\tau})\right]_+$ at the kth order in perturbation theory, where α_s is the strong coupling and the "plus" distribution will be defined below. Sufficiently close to threshold, the perturbative series will be useful only if such terms are taken into account to all orders in α_s, which is what is achieved by threshold resummation [20, 41, 42, 80]. Here we extend threshold resummation further, to cross sections involving cuts on individual hadron p_T and the rapidity of the pair.

We note that this behavior near threshold is very familiar from that in the Drell-Yan process, if one thinks of $\hat{m}$ as the invariant mass of the lepton pair. Hadron pair production is more complex in that gluon emission will occur not only from initial-state partons, but also from those in the final state. Furthermore, interference between soft emissions from the various external legs is sensitive to the color exchange in the hard scattering, which gives rise to a special additional contribution to the resummation formula, derived in [20, 43, 44].

The larger $\hat{\tau}$, the more dominant the threshold logarithms will be. Because of this and the rapid fall-off of the parton distributions and fragmentation functions with momentum fraction, threshold effects tend to become more and more relevant as the *hadronic* scaling variable $\tau \equiv M^2/S$ goes to one. This means that the fixed-target regime is the place where threshold resummation is expected to be particularly relevant and useful. We will indeed confirm this in

our study. Nonetheless, because of the convolution form of the partonic cross sections and the parton distributions and fragmentation functions (see below), the threshold regime $\hat{\tau} \to 1$ plays an important role also at higher (collider) energies. Here one may, however, also have to incorporate higher-order terms that are subleading at partonic threshold.

In Sec. 3.2 we provide the basic formulas for the di-hadron cross section as a function of pair mass at fixed order in perturbation theory, and display the role of the threshold region. Section 3.3 presents details of the threshold resummation for the cross section. In Sec. 3.4 we give phenomenological results, comparing the threshold resummed calculation to the available experimental data. Finally, we summarize our results in Sec. 3.5. The Appendices provide details of the NLO corrections to the perturbative cross section near threshold.

3.2 Perturbative Cross Section and Partonic Threshold

We are interested in the hadronic cross section for the production of two hadrons $h_{1,2}$,

$$H_1(P_1) + H_2(P_2) \to h_1(K_1) + h_2(K_2) + X \ , \tag{3.1}$$

with pair invariant mass

$$M^2 \equiv (K_1 + K_2)^2 \ . \tag{3.2}$$

We will consider the cross section differential in the rapidities η_1, η_2 of the two produced hadrons, treated as massless, in the c.m.s. of the initial hadrons, or in their difference and average,

$$\Delta\eta = \frac{1}{2}(\eta_1 - \eta_2) \ , \tag{3.3}$$

$$\bar{\eta} = \frac{1}{2}(\eta_1 + \eta_2) \ . \tag{3.4}$$

We will later integrate over regions of rapidity corresponding to the relevant experimental coverage.

For sufficiently large M^2, the cross section for the process can be written

in the factorized form

$$M^4 \frac{d\sigma^{H_1H_2\to h_1h_2X}}{dM^2 d\Delta\eta d\bar{\eta}} = \sum_{abcd} \int_0^1 dx_a dx_b dz_c dz_d \, f_a^{H_1}(x_a,\mu_{Fi}) f_b^{H_2}(x_b,\mu_{Fi}) \times z_c D_c^{h_1}(z_c,\mu_{Ff}) z_d D_d^{h_2}(z_d,\mu_{Ff}) \times \frac{\hat{m}^4 d\hat{\sigma}^{ab\to cd}}{d\hat{m}^2 d\Delta\eta d\bar{\eta}} \left(\hat{\tau},\Delta\eta,\hat{\eta},\alpha_s(\mu_R),\frac{\mu_R}{\hat{m}},\frac{\mu_{Fi}}{\hat{m}},\frac{\mu_{Ff}}{\hat{m}}\right) , \quad (3.5)$$

where $\hat{\eta}$ is the average rapidity in the partonic c.m.s., which is related to $\bar{\eta}$ by

$$\hat{\eta} = \bar{\eta} - \frac{1}{2}\ln\left(\frac{x_a}{x_b}\right) . \quad (3.6)$$

The quantity $\Delta\eta$ is a difference of rapidities and hence boost invariant. It is important to note that the rapidities of the hadrons with light-like momenta K_1 and K_2 are the same as those of their light-like parent partons. The average and relative rapidities for the hadrons and their parent partons are also therefore the same, a feature that we will use below. Furthermore, in Eq. (3.5) the $f_{a,b}^{H_{1,2}}$ are the parton distribution functions for partons a,b in hadrons $H_{1,2}$ and $D_{c,d}^{h_{1,2}}$ the fragmentation functions for partons c,d fragmenting into the observed hadrons $h_{1,2}$. The distribution functions are evaluated at the initial-state and final-state factorization scales μ_{Fi} and μ_{Ff}, respectively. μ_R denotes the renormalization scale. The $d\hat{\sigma}^{ab\to cd}/d\hat{\tau}d\bar{\eta}d\Delta\eta$ are the partonic differential cross sections for the contributing partonic processes $ab\to cdX'$, where X' denotes some additional unobserved partonic final state. The partonic momenta are given in terms of the hadronic ones by $p_a = x_aP_1$, $p_b = x_bP_2$, $p_c = K_1/z_c$, $p_d = K_2/z_d$. We introduce a set of variables, some of which have been used in Eq. (3.5):

$$S = (P_1+P_2)^2 , \quad (3.7)$$

$$\tau \equiv \frac{M^2}{S} , \quad (3.8)$$

$$\hat{s} \equiv (x_aP_1+x_bP_2)^2 = x_ax_bS , \quad (3.9)$$

$$\hat{m}^2 \equiv \left(\frac{K_1}{z_c}+\frac{K_2}{z_d}\right)^2 = \frac{M^2}{z_cz_d} , \quad (3.10)$$

$$\hat{\tau} \equiv \frac{\hat{m}^2}{\hat{s}} = \frac{M^2}{x_ax_bz_cz_dS} = \frac{\tau}{x_ax_bz_cz_d} . \quad (3.11)$$

At the level of partonic scattering in the factorized cross section, Eq. (3.5), the

other relevant variables are the partonic c.m.s. energy $\sqrt{\hat{s}}$, and the invariant mass $\hat{m}$ of the pair of partons that fragment into the observed di-hadron pair. We have written Eq. (3.5) in such a way that the term in square brackets is a dimensionless function. Hence, it can be chosen to be a function of the dimensionless ratio $\hat{m}^2/\hat{s} = \hat{\tau}$ and the ratio of $\hat{m}$ to the factorization and renormalization scales, as well as the rapidities and the strong coupling. In the following, we will take all factorization scales to be equal to the renormalization scale for simplicity, that is, $\mu_R = \mu_{Fi} = \mu_{Ff} \equiv \mu$. We then write

$$\frac{\hat{m}^4 d\hat{\sigma}^{ab\to cd}}{d\hat{m}^2 d\Delta\eta d\bar{\eta}}\left(\hat{\tau}, \Delta\eta, \hat{\eta}, \alpha_s(\mu), \frac{\mu}{\hat{m}}\right) \equiv \omega_{ab\to cd}\left(\hat{\tau}, \Delta\eta, \hat{\eta}, \alpha_s(\mu), \frac{\mu}{\hat{m}}\right) . \quad (3.12)$$

The variable $\hat{\tau}$ is of special interest for threshold resummation, because it is a measure of the phase space available for radiation at short distances. The limit $\hat{\tau} \to 1$ corresponds to the partonic threshold, where the partonic hard scattering uses all available energy to produce the pair. This is kinematically similar to the Drell-Yan process, if one thinks of the hadron pair replaced by a lepton pair. The presence of fragmentation of course complicates the analysis somewhat, because only a fraction $z_c z_d$ of $\hat{m}^2$ is used for the invariant mass of the observed hadron pair. In the following it will in fact be convenient to also use the variable

$$\tau' \equiv \frac{\hat{m}^2}{S} = \frac{M^2}{z_c z_d S} , \quad (3.13)$$

which is the ratio of the partonic $\hat{m}^2$ to the overall c.m.s. invariant S and hence may be viewed as the "τ-variable" at the level of produced partons when fragmentation has not yet been taken into account. This variable is close in spirit to the variable $\tau = Q^2/S$ in Drell-Yan.

The partonic cross sections can be computed in QCD perturbation theory, where they are expanded as

$$\omega_{ab\to cd} = \left(\frac{\alpha_s}{\pi}\right)^2 \left[\omega^{\mathrm{LO}}_{ab\to cd} + \frac{\alpha_s}{\pi}\omega^{\mathrm{NLO}}_{ab\to cd} + \ldots\right] . \quad (3.14)$$

Here we have separated the overall power of $\mathcal{O}(\alpha_s^2)$, which arises because the leading order (LO) partonic hard-scattering processes are the ordinary $2 \to 2$ QCD scatterings. At LO, one has $\hat{\tau} = 1$, and also the two partons are produced back-to-back in the partonic c.m.s., so that $\hat{\eta} = 0$. One can therefore write the LO term as

$$\omega^{\mathrm{LO}}_{ab\to cd}\left(\hat{\tau}, \Delta\eta, \hat{\eta}\right) = \delta\left(1 - \hat{\tau}\right)\, \delta\left(\hat{\eta}\right)\, \omega^{(0)}_{ab\to cd}(\Delta\eta) , \quad (3.15)$$

where $\omega^{(0)}_{ab\to cd}$ is a function of $\Delta\eta$ only. The second delta-function implies that $\bar{\eta} = \frac{1}{2}\ln(x_a/x_b)$. At next-to-leading order (NLO), or overall $\mathcal{O}(\alpha_s^3)$, one can have $\hat{\tau} \neq 1$ and $\hat{\eta} \neq 0$. Near partonic threshold, $\hat{\tau} \to 1$, however, the kinematics becomes "LO like". The average rapidity of the final-state partons, c and d (and therefore of the observed di-hadrons) is determined by the ratio x_a/x_b, up to corrections that vanish when the energy available for soft radiation is squeezed to zero. As noted in Ref. [45], in this limit the delta function that fixes the partonic pair rapidity $\hat{\eta}$ becomes independent of soft radiation, and may be factored out of the phase space integral over the latter. This is true at all orders in perturbation theory. One has:

$$\begin{aligned}\omega_{ab\to cd}\left(\hat{\tau},\Delta\eta,\hat{\eta},\alpha_s(\mu),\mu/\hat{m}\right) &= \delta\left(\hat{\eta}\right)\,\omega^{\rm sing}_{ab\to cd}\left(\hat{\tau},\Delta\eta,\alpha_s(\mu),\mu/\hat{m}\right) \\ &\quad + \omega^{\rm reg}_{ab\to cd}\left(\hat{\tau},\Delta\eta,\hat{\eta},\alpha_s(\mu),\mu/\hat{m}\right)\ , \end{aligned} \tag{3.16}$$

where all singular behavior near threshold is contained in the functions $\omega^{\rm sing}_{ab\to cd}$. Threshold resummation addresses this singular part to all orders in the strong coupling. All remaining contributions, which are subleading near threshold, are collected in the "regular" functions $\omega^{\rm reg}_{ab\to cd}$. Specifically, for the NLO corrections, one finds the following structure:

$$\begin{aligned}\omega^{\rm NLO}_{ab\to cd}\left(\hat{\tau},\Delta\eta,\hat{\eta},\mu/\hat{m}\right) &= \delta\left(\hat{\eta}\right)\,\Big[\omega^{(1,0)}_{ab\to cd}(\Delta\eta,\mu/\hat{m})\,\delta(1-\hat{\tau}) \\ &\quad + \omega^{(1,1)}_{ab\to cd}(\Delta\eta,\mu/\hat{m})\,\left(\frac{1}{1-\hat{\tau}}\right)_+ + \omega^{(1,2)}_{ab\to cd}(\Delta\eta)\left(\frac{\log(1-\hat{\tau})}{1-\hat{\tau}}\right)_+\Big] \\ &\quad + \omega^{\rm reg,NLO}_{ab\to cd}(\hat{\tau},\Delta\eta,\hat{\eta},\mu/\hat{m})\ , \end{aligned} \tag{3.17}$$

where the singular part near threshold is represented by the functions $\omega^{(1,0)}_{ab\to cd}$, $\omega^{(1,1)}_{ab\to cd}$, $\omega^{(1,2)}_{ab\to cd}$, which are again functions of only $\Delta\eta$, up to scale dependence. The "plus"-distributions are defined by

$$\int_{x_0}^1 f(x)\left(g(x)\right)_+ dx \equiv \int_{x_0}^1 \left(f(x)-f(1)\right)\,g(x)dx - f(1)\int_0^{x_0} g(x)dx\ . \tag{3.18}$$

Appendix A describes the derivation of the coefficients $\omega^{(1,0)}_{ab\to cd}, \omega^{(1,1)}_{ab\to cd}, \omega^{(1,2)}_{ab\to cd}$ explicitly from a calculation of the NLO corrections near threshold. This will serve as a useful check on the correctness of the resummed formula, and also to determine certain matching coefficients.

As suggested above, the structure given in Eq. (3.17) is similar to that found for the Drell-Yan cross section at NLO. A difference is that in the inclusive Drell-Yan case one can integrate over all $\Delta\eta$ to obtain a total cross section.

This integration is finite because the LO process in Drell-Yan is the s-channel reaction $q\bar{q} \to \ell^+\ell^-$. In the case of di-hadrons, the LO QCD processes also have t as well as u-channel contributions, which cause the integral over $\Delta\eta$ to diverge when the two hadrons are produced back-to-back with large mass, but each parallel or anti-parallel to the initial beams. As a result, one will always need to consider only a finite range in $\Delta\eta$. This is, of course, not a problem as this is anyway also done in experiment. It does, however, require a slightly more elaborate analysis for threshold resummation, which we review below.

3.3 Threshold Resummation for Di-hadron Pairs

3.3.1 Hard Scales and Transforms

The resummation of the logarithmic corrections is organized in Mellin-N moment space [41]. In moment space, the partonic cross sections absorb logarithmic corrections associated with the emission of soft and collinear gluons to all orders. Employing appropriate moments, which we will identify shortly, we will see that the convolutions among the different nonperturbative and perturbative regions in the hadronic cross section decouple.

In terms of the dimensionless hard-scattering function introduced in Eq. (3.12) the hadronic cross section in Eq. (3.5) becomes

$$M^4 \frac{d\sigma^{H_1H_2\to h_1h_2X}}{dM^2 d\Delta\eta d\bar{\eta}} = \sum_{abcd} \int_0^1 dx_a dx_b\, dz_c\, dz_d\, f_a^{H_1}(x_a) f_b^{H_2}(x_b) \times z_c D_c^{h_1}(z_c) z_d D_d^{h_2}(z_d)\, \omega_{ab\to cd}\left(\hat{\tau}, \Delta\eta, \hat{\eta}, \alpha_s(\mu), \frac{\mu}{\hat{m}}\right) , \quad (3.19)$$

where for simplicity we have dropped the scale dependence of the parton distributions and fragmentation functions. At lowest order, when the hard-scattering function $\omega_{ab\to cd}$ is given by Eq. (3.15), the cross section is found to factorize under "double" moments [46, 47], a Mellin moment with respect to

$\tau = M^2/S$ and a Fourier moment in $\bar{\eta} = \hat{\eta} + \frac{1}{2}\ln(x_a/x_b)$:

$$\int_{-\infty}^{\infty} d\bar{\eta}\, \mathrm{e}^{i\nu\bar{\eta}} \int_0^1 d\tau\, \tau^{N-1} M^4 \frac{d\sigma^{H_1H_2\to h_1h_2X}}{dM^2 d\Delta\eta d\bar{\eta}}\bigg|_{\rm LO}$$

$$= \sum_{abcd} \tilde{f}_a^{H_1}(N+1+i\nu/2)\tilde{f}_b^{H_2}(N+1-i\nu/2)\tilde{D}_c^{h_1}(N+2)\tilde{D}_d^{h_2}(N+2)$$

$$\times \int_{-\infty}^{\infty} d\hat{\eta}\, \mathrm{e}^{i\nu\hat{\eta}} \int_0^1 d\hat{\tau}\, \hat{\tau}^{N-1}\, \delta\left(1-\hat{\tau}\right)\, \delta\left(\hat{\eta}\right)\, \left(\frac{\alpha_s(\mu)}{\pi}\right)^2 \omega^{(0)}_{ab\to cd}(\Delta\eta)\,, \quad (3.20)$$

where the Mellin moments of the parton distributions or fragmentation functions are defined in the usual way, for example

$$\tilde{f}_a^H(N) \equiv \int_0^1 x^{N-1} f_a^H(x) dx\,. \quad (3.21)$$

We note that instead of a combined Mellin and Fourier transform one may equivalently use a suitable double-Mellin transform [48]. The last two integrals in Eq. (3.20) give the combined Mellin and Fourier moment of the LO partonic cross section. Because of the two delta-functions, they are trivial and just yield the N and ν independent result $(\alpha_s/\pi)^2\omega^{(0)}_{ab\to cd}(\Delta\eta)$. One might expect that this generalizes to higher orders, so that the double moments

$$\int_{-\infty}^{\infty} d\hat{\eta}\, \mathrm{e}^{i\nu\hat{\eta}} \int_0^1 d\hat{\tau}\, \hat{\tau}^{N-1}\, \omega_{ab\to cd}\left(\hat{\tau}, \Delta\eta, \hat{\eta}, \alpha_s(\mu), \frac{\mu}{\hat{m}}\right) \quad (3.22)$$

would appear times moments of fragmentation functions. However, this is impeded by the presence of the renormalization/factorization scale μ which must necessarily enter in a ratio with $\hat{m} = M/\sqrt{z_c z_d}$. As a result of this dependence on z_c and z_d, the moments $\tilde{D}_c^{h_1}(N+2)$, $\tilde{D}_d^{h_2}(N+2)$ of the fragmentation functions will no longer be generated, and the factorized cross section does not separate into a product under moments. Physically, this is a reflection of the mismatch between the *observed* scale, the di-hadron mass M, and the *unobserved* threshold scale at the hard scattering, $\hat{m}$. Threshold logarithms appear when $\hat{s}$ approaches the latter scale, not the former. This implies that at fixed M there is actually a range of hard-scattering partonic thresholds, extending all the way from M at the lower end to $\sqrt{S}$ at the upper. This situation is to be contrasted to the Drell-Yan process or to di-jet production at fixed masses, where the underlying hard scale is defined directly by the observable.

We will deal with the presence of this range of hard scales $\hat{m}$ by car-

rying out threshold resummation at fixed $\hat{m}$ as well as at fixed factorization/renormalization scale. For this purpose, we rewrite the cross section (3.19) in a form that isolates the fragmentation functions:

$$M^4 \frac{d\sigma^{H_1H_2\to h_1h_2X}}{dM^2 d\Delta\eta d\bar{\eta}} = \sum_{cd} \int_0^1 dz_c\, dz_d\, z_c\, D_c^{h_1}(z_c,\mu)\, z_d\, D_d^{h_2}(z_d,\mu) \Omega_{H_1H_2\to cd}\left(\tau', \Delta\eta, \bar{\eta}, \alpha_s(\mu), \frac{\mu}{\hat{m}}\right) , \quad (3.23)$$

where again $\tau' = \hat{m}^2/S = \hat{\tau} x_a x_b$ and $\Omega_{H_1H_2\to cd}$ is given by the convolution of the parton distribution functions and $\omega_{ab\to cd}$:

$$\Omega_{H_1H_2\to cd}\left(\tau', \Delta\eta, \bar{\eta}, \alpha_s(\mu), \frac{\mu}{\hat{m}}\right) = \sum_{ab} \int_0^1 dx_a\, dx_b\, f_a^{H_1}(x_a,\mu)\, f_b^{H_2}(x_b,\mu) \omega_{ab\to cd}\left(\hat{\tau}, \Delta\eta, \hat{\eta}, \alpha_s(\mu), \frac{\mu}{\hat{m}}\right) , \quad (3.24)$$

with $\hat{\eta} = \bar{\eta} - \frac{1}{2}\ln(x_a/x_b)$ as before. At fixed final-state *partonic* mass $\hat{m}$, the function $\Omega_{H_1H_2\to cd}$ now has the desired factorization property under Fourier and Mellin transforms:

$$\int_{-\infty}^{\infty} d\bar{\eta}\, \mathrm{e}^{i\nu\bar{\eta}} \int_0^1 d\tau'\, (\tau')^{N-1}\, \Omega_{H_1H_2\to cd}\left(\tau', \Delta\eta, \bar{\eta}, \alpha_s(\mu), \frac{\mu}{\hat{m}}\right) = \sum_{ab} \tilde{f}_a^{H_1}(N+1+i\nu/2,\mu) \tilde{f}_b^{H_2}(N+1-i\nu/2,\mu) \times \tilde{\omega}_{ab\to cd}\left(N, \nu, \Delta\eta, \alpha_s(\mu), \frac{\mu}{\hat{m}}\right) , \quad (3.25)$$

where

$$\tilde{\omega}_{ab\to cd}\left(N, \nu, \Delta\eta, \alpha_s(\mu), \frac{\mu}{\hat{m}}\right) \equiv \int_{-\infty}^{\infty} d\hat{\eta}\, \mathrm{e}^{i\nu\hat{\eta}} \int_0^1 d\hat{\tau}\, \hat{\tau}^{N-1}\, \omega_{ab\to cd}\left(\hat{\tau}, \Delta\eta, \hat{\eta}, \alpha_s(\mu), \frac{\mu}{\hat{m}}\right) \quad (3.26)$$

Through Eqs. (3.23)–(3.26) we have formulated the hadronic cross section in a way that involves moment-space expressions for the partonic hard-scattering functions, which may be resummed. Because the final-state fractions z_i equal unity at partonic threshold, the scale $\hat{m}$ in the short-distance function may be identified here with the final-state partonic invariant mass, up to corrections that are suppressed by powers of N. For the singular, resummed short-distance function we therefore do not encounter the problem with the moments

discussed above in connection with Eq. (3.22).

3.3.2 Resummation at Next-to-Leading Logarithm

As we saw in Eq. (3.16), the singular parts of the partonic cross sections near threshold enter with $\delta(\hat{\eta})$. This gives for the corresponding moment-space expression

$$\tilde{\omega}^{\rm resum}_{ab\to cd}\left(N,\Delta\eta,\alpha_s(\mu),\frac{\mu}{\hat{m}}\right)=\int_0^1 d\hat{\tau}\,\hat{\tau}^{N-1}\,\omega^{\rm sing}_{ab\to cd}\left(\hat{\tau},\Delta\eta,\alpha_s(\mu),\frac{\mu}{\hat{m}}\right)\,. \quad (3.27)$$

which is a function of N only, but not of the Fourier variable ν. Dependence on the Fourier variable ν then resides entirely in the parton distributions. It is this function, $\tilde{\omega}^{\rm resum}_{ab\to cd}$, that threshold resummation addresses, which is the reason for the use of the label "resum" from now on.

The nature of singularities at partonic threshold is determined by the available phase space for radiation as $\hat{\tau}\to 1$. Denoting by k^μ the combined momentum of all radiation, whether from the incoming partons a and b or the outgoing partons c and d, one has

$$1-\hat{\tau}=1-\frac{(p_c+p_d)^2}{(p_a+p_b)^2}=1-\frac{(p_a+p_b-k)^2}{(p_a+p_b)^2}\approx\frac{2k_0^*}{\sqrt{s}}\,, \quad (3.28)$$

where k_0^* is the energy of the soft radiation in the c.m.s of the initial partons.

At partonic threshold, the cross section factorizes into "jet" functions associated with the two incoming and outgoing partons, in addition to an overall soft matrix, traced against the color matrix describing the hard scattering [20, 43]. Corrections to this factorized structure are suppressed by powers of $1-\hat{\tau}$. The total cross section is a convolution in energy between these functions, which is factorized into a product by moments in $\hat{\tau}^N\sim\exp[-N(1-\hat{\tau})]$, again with corrections suppressed by powers of $(1-\hat{\tau})$, or equivalently, powers of N. This result was demonstrated for jet cross sections in [43], and the extension to observed hadrons in the final state was discussed in [49, 50]. The resummed expression for the partonic hard-scattering function for the process $ab\to cd$ then reads [20, 43, 44, 80]:

$$\begin{aligned}\tilde{\omega}^{\rm resum}_{ab\to cd}\left(N,\Delta\eta,\alpha_s(\mu),\frac{\mu}{\hat{m}}\right) &= \Delta_a^{N+1}\left(\alpha_s(\mu),\frac{\mu}{\hat{m}}\right)\Delta_b^{N+1}\left(\alpha_s(\mu),\frac{\mu}{\hat{m}}\right)\\ &\times{\rm Tr}\left\{H\mathcal{S}_N^\dagger S\mathcal{S}_N\right\}_{ab\to cd}\left(\Delta\eta,\alpha_s(\mu),\frac{\mu}{\hat{m}}\right)\\ &\times\Delta_c^{N+2}\left(\alpha_s(\mu),\frac{\mu}{\hat{m}}\right)\Delta_d^{N+2}\left(\alpha_s(\mu),\frac{\mu}{\hat{m}}\right) \quad (3.29)\end{aligned}$$

Each of the functions $H_{ab\to cd}$, $\mathcal{S}_{N,ab\to cd}$, $S_{ab\to cd}$ in Eq. (3.29) is a matrix in a space of color exchange operators [20, 43], and the trace is taken in this space. Note that this part is the only one in the resummed expression Eq. (3.29) that carries dependence on $\Delta\eta$. The $H_{ab\to cd}$ are the hard-scattering functions. They are perturbative and have the expansion

$$H_{ab\to cd}\left(\Delta\eta, \alpha_s(\mu), \frac{\mu}{\hat{m}}\right) = H^{(0)}_{ab\to cd}\left(\Delta\eta\right) + \frac{\alpha_s(\mu)}{\pi} H^{(1)}_{ab\to cd}\left(\Delta\eta, \frac{\mu}{\hat{m}}\right) + \mathcal{O}(\alpha_s^2) \; . \tag{3.30}$$

The LO (*i.e.* $\mathcal{O}(\alpha_s^2)$) parts $H^{(0)}_{ab\to cd}$ are known [20, 43, 44], but the first-order corrections have not been derived yet. We shall return to this point shortly. The $S_{ab\to cd}$ are soft functions. They depend on N only through the argument of the running coupling, which is set to μ/N [20], and have the expansion

$$S_{ab\to cd}\left(\Delta\eta, \alpha_s, \frac{\mu}{\hat{m}}\right) = S^{(0)}_{ab\to cd} + \frac{\alpha_s}{\pi} S^{(1)}_{ab\to cd}\left(\Delta\eta, \frac{\mu}{N\hat{m}}\right) + \mathcal{O}(\alpha_s^2) \; . \tag{3.31}$$

The N-dependence of the soft function enters the resummed cross section at the level of next-to-next-to-leading logarithms. The LO terms $S^{(0)}_{ab\to cd}$ may also be found in [20, 43, 44]. They are independent of $\Delta\eta$.

The resummation of wide-angle soft gluons is contained in the $\mathcal{S}_{ab\to cd}$, which are exponentials and given in terms of soft anomalous dimensions, $\Gamma_{ab\to cd}$:

$$\mathcal{S}_{N,ab\to cd}\left(\Delta\eta, \alpha_s(\mu), \frac{\mu}{\hat{m}}\right) = \mathcal{P}\exp\left[\frac{1}{2}\int_{\hat{m}^2}^{\hat{m}^2/\bar{N}^2} \frac{dq^2}{q^2} \Gamma_{ab\to cd}\left(\Delta\eta, \alpha_s(q^2)\right)\right] \; , \tag{3.32}$$

where $\mathcal{P}$ denotes path ordering and where $\bar{N} \equiv N\mathrm{e}^{\gamma_E}$ with γ_E is the Euler constant. The soft anomalous dimension matrices start at $\mathcal{O}(\alpha_s)$,

$$\Gamma_{ab\to cd}\left(\Delta\eta, \alpha_s\right) = \frac{\alpha_s}{\pi}\, \Gamma^{(1)}_{ab\to cd}\left(\Delta\eta\right) + \mathcal{O}(\alpha_s^2) \; . \tag{3.33}$$

Their first-order terms are presented in [20, 43, 44, 51].

The Δ_i^N ($i = a, b, c, d$) represent the effects of soft-gluon radiation collinear to an initial or final parton. Working in the $\overline{\mathrm{MS}}$ scheme, one has [20, 41, 43, 44, 80]:

$$\begin{aligned} \ln \Delta_i^N\left(\alpha_s(\mu), \frac{\mu}{\hat{m}}\right) &= \int_0^1 \frac{z^{N-1}-1}{1-z} \int_{\hat{m}^2}^{(1-z)^2\hat{m}^2} \frac{dq^2}{q^2} A_i(\alpha_s(q^2)) \\ &+ \int_{\mu^2}^{\hat{m}^2} \frac{dq^2}{q^2}\left[-A_i(\alpha_s(q^2))\ln\bar{N} - \frac{1}{2}B_i(\alpha_s(q^2))\right] \end{aligned} \tag{3.34}$$

Here the functions A_i and B_i are perturbative series in α_s,

$$A_i(\alpha_s) = \frac{\alpha_s}{\pi} A_i^{(1)} + \left(\frac{\alpha_s}{\pi}\right)^2 A_i^{(2)} + \dots \,, \tag{3.35}$$

and likewise for B_i. To NLL, one needs the coefficients [84]:

$$\begin{aligned} A_i^{(1)} &= C_i \,, \quad A_a^{(2)} = \frac{1}{2}\, C_i \left[C_A \left(\frac{67}{18} - \frac{\pi^2}{6} \right) - \frac{5}{9} N_f \right] \,, \\ B_q^{(1)} &= -\frac{3}{2} C_F \,, \quad B_g^{(1)} = -2\pi\beta 0 \,, \end{aligned} \tag{3.36}$$

where N_f is the number of flavors, and

$$\begin{aligned} C_q = C_F &= \frac{N_c^2 - 1}{2N_c} = \frac{4}{3} \,, \quad C_g = C_A = N_c = 3 \,, \\ b_0 &= \frac{11 C_A - 2N_f}{12\pi} \,. \end{aligned} \tag{3.37}$$

The factors Δ_i^N generate leading threshold enhancements, due to soft-collinear radiation. We note that our expression for the Δ_i^N differs by the N-independent term proportional to $B_i^{(1)}$ from that often used in studies of threshold resummation (see, for example, Refs. [22, 80]). As was shown in [20, 43, 44], this term is part of the resummed expression and exponentiates. In fact, the second term on the right-hand-side of Eq. (3.34) contains the large-N part of the moments of the diagonal quark and gluon splitting functions, matching the full leading power μ_F-dependence of the parton distributions and fragmentation functions in Eqs. (3.23) and (3.25). We shall return to this point below. Here, we note that the Born cross sections are recovered by computing the following $\mathrm{Tr}\{H^{(0)} S^{(0)}\}_{ab\to cd}$, which is proportional to the function $\omega^{(0)}_{ab\to cd}(\Delta\eta)$ introduced in Eq. (3.15). It is instructive to consider the expansion of the trace part in Eq. (3.29) to first order in α_s. One finds [52]:

$$\begin{aligned} \mathrm{Tr}\left\{ H \mathcal{S}_N^\dagger S \mathcal{S}_N \right\}_{ab\to cd} \;=\; & \mathrm{Tr}\{H^{(0)} S^{(0)}\}_{ab\to cd} \\ & + \frac{\alpha_s}{\pi}\, \mathrm{Tr}\left\{ - \left[H^{(0)} (\Gamma^{(1)})^\dagger S^{(0)} + H^{(0)} S^{(0)} \Gamma^{(1)} \right] \ln \bar{N} \right. \\ & \left. + H^{(1)} S^{(0)} + H^{(0)} S^{(1)} \right\}_{ab\to cd} + \mathcal{O}(\alpha_s^2) \,. \end{aligned} \tag{3.38}$$

When combined with the first-order expansion of the factors Δ_i^N in Eq. (3.29),

one obtains

$$\begin{aligned}\tilde{\omega}^{\rm resum}_{ab\to cd}\left(N,\Delta\eta,\alpha_s(\mu),\frac{\mu}{\hat{m}}\right) &= {\rm Tr}\{H^{(0)}S^{(0)}\}_{ab\to cd} \\ &\times\left(1+\frac{\alpha_s}{\pi}\sum_{i=a,b,c,d}A_i^{(1)}\left[\ln^2\bar{N}+\ln\bar{N}\ln(\mu^2/\hat{m}^2)\right]\right) \\ &+\frac{\alpha_s}{\pi}\,{\rm Tr}\left\{-\left[H^{(0)}(\Gamma^{(1)})^\dagger S^{(0)}+H^{(0)}S^{(0)}\Gamma^{(1)}\right]\ln\bar{N}\right. \\ &\left.+H^{(1)}S^{(0)}+H^{(0)}S^{(1)}\right\}_{ab\to cd}+\mathcal{O}(\alpha_s^2)\,. \qquad (3.39)\end{aligned}$$

This expression can be compared to the results of the explicit NLO calculation near threshold given in Appendix A. This provides a cross-check on the terms that are logarithmic in N, that is, singular at threshold. From comparison to the part proportional to $\delta(1-\hat{\tau})$ in the NLO expression, one will be able to read off the combination $(H^{(1)}S^{(0)}+H^{(0)}S^{(1)})$ in Eq. (3.39). This is, of course, not sufficient to determine the full first-order matrices $H^{(1)}$ and $S^{(1)}$, which would be needed to fully evaluate the trace part in in Eq. (3.29) to NLL. To derive $H^{(1)}$ and $S^{(1)}$, one would need to perform the NLO calculation near threshold in terms of a color decomposition [53], which is beyond the scope of this work. Instead, we use here an approximation that has been made in previous studies (see, for example, Ref. [30]),

$$\begin{aligned}{\rm Tr}\left\{H\mathcal{S}_N^\dagger S\mathcal{S}_N\right\}_{ab\to cd} &\approx \left(1+\frac{\alpha_s}{\pi}C^{(1)}_{ab\to cd}\right){\rm Tr}\left\{H^{(0)}\mathcal{S}_N^\dagger S^{(0)}\mathcal{S}_N\right\}_{ab\to cd} \qquad (3.40)\end{aligned}$$

where

$$C^{(1)}_{ab\to cd}(\Delta\eta,\mu/\hat{m})\equiv\frac{{\rm Tr}\left\{H^{(1)}S^{(0)}+H^{(0)}S^{(1)}\right\}_{ab\to cd}}{{\rm Tr}\left\{H^{(0)}S^{(0)}\right\}_{ab\to cd}} \qquad (3.41)$$

are referred to as "C-coefficients". The coefficients we obtain for the various partonic channels are given in Appendix B. The approximation we have made becomes exact if only one color configuration contributes or if all eigenvalues of the soft anomalous dimension matrix are equal. By construction, it is also correct to first order in α_s.

We now turn to the explicit NLL expansions of the ingredients in the resummed partonic cross section. For the function Δ_i^N in Eq. (3.34) one finds:

$$\ln\Delta_i^N\left(\alpha_s(\mu),\frac{\mu}{\hat{m}}\right)=h_i^{(1)}(\lambda)\,\ln\bar{N}+h_i^{(2)}\left(\lambda,\alpha_s(\mu),\frac{\mu}{\hat{m}}\right)+\ln\mathcal{E}_i\left(\lambda,\alpha_s(\mu),\frac{\mu}{\hat{m}}\right)\,, \qquad (3.42)$$

where $\lambda = b_0 \alpha_s(\mu) \ln \bar{N}$ and the functions $h_i^{(1)}, h_i^{(2)}, \ln(\mathcal{E}_i)$ are given by

$$\begin{aligned}
h_i^{(1)}(\lambda) &= \frac{A_i^{(1)}}{2\pi\beta 0 \lambda} \left(2\lambda + \ln(1-2\lambda)\right) \ , \\
h_i^{(2)}\left(\lambda, \alpha_s(\mu), \frac{\mu}{\hat{m}}\right) &= \frac{2\lambda + \ln(1-2\lambda)}{2\pi b_0} \left(\frac{A_i^{(1)} b_1}{b_0^2} - \frac{A_i^{(2)}}{\pi\beta 0} - A_i^{(1)} \ln \frac{\mu^2}{\hat{m}^2} \right) \\
&\quad + \frac{A_i^{(1)} b_1}{4\pi\beta 0^3} \ln^2(1-2\lambda) + \frac{B_i^{(1)}}{2\pi\beta 0} \ln(1-2\lambda) \ , \\
\ln \mathcal{E}_i\left(\lambda, \alpha_s(\mu), \frac{\mu}{\hat{m}}\right) &= \frac{1}{\pi\beta 0} \left(-A_i^{(1)} \ln \bar{N} - \frac{1}{2} B_i^{(1)} \right) \\
&\quad \times \left[\ln(1-2\lambda) - \beta 0 \alpha_s(\mu) \ln \frac{\mu^2}{\hat{m}^2} \right] \ . \qquad (3.43)
\end{aligned}$$

We note that we have written Eq. (3.42) in a "non-standard" form that is actually somewhat more complex than necessary. For example, one can immediately see that the terms proportional to $B_i^{(1)} \ln(1-2\lambda)$ cancel between the functions $h_i^{(2)}$ and $\ln(\mathcal{E}_i)$, as they must because they were not present in the Δ_i^N in Eq. (3.34) in the first place. The term proportional to $\ln(\mu^2/\hat{m}^2)$ in $\ln(\mathcal{E}_i)$ is the expansion of the second term in Eq. (3.34). Its contribution involving $B_i^{(1)}$ does not carry logarithmic dependence on N and would normally be part of the "C-coefficients" discussed above. The term proportional to $\ln(1-2\lambda)$ in $\ln(\mathcal{E}_i)$ has been separated off the first term in Eq. (3.34). Our motivation to use this form of Eq. (3.42) is that the piece termed $\ln(\mathcal{E}_i)$ may be viewed as resulting from a large-N leading-order evolution of the corresponding parton distribution or fragmentation function between scales $\hat{m}/\bar{N}$ and the factorization scale μ_F (we remind the reader that we have set the factorization and renormalization scales equal and denoted them by μ). As mentioned earlier, the factors $(-2A_i^{(1)} \ln \bar{N} - B_i^{(1)})$ correspond to the moments of the flavor-diagonal splitting functions, P_{ii}^N, while the term in square brackets is a LO approximation to

$$\beta 0 \int_{\mu_F}^{\hat{m}^2/\bar{N}^2} \frac{dq^2}{q^2} \alpha_s(q^2) \ . \qquad (3.44)$$

Therefore, it is natural to identify [54]

$$\mathcal{E}_i\left(\lambda, \alpha_s(\mu), \frac{\mu}{\hat{m}}\right) \tilde{f}_i^H(N,\mu) \leftrightarrow \tilde{f}_i^H(N, \hat{m}/\bar{N}) \ , \qquad (3.45)$$

that is, the exponential related to $\mathcal{E}_i$ evolves the parton distributions from

the factorization scale to the scale $\hat{m}/\bar{N}$, and likewise for the fragmentation functions. At the level of diagonal evolution, it makes of course no difference if $\ln(\mathcal{E}_i)$ is used to evolve the parton distributions or if it is just added to the function $h_i^{(2)}$. However, as was discussed in [54, 55], one can actually promote the diagonal evolution expressed by $\mathcal{E}_i$ to the full singlet case by replacing the term $(-2A_i^{(1)} \ln \bar{N} - B_i^{(1)})$ by the full matrix of the moments of the LO singlet splitting functions, $P_{ij}^{(1),N}$, so that $\mathcal{E}$ itself becomes a matrix. Using this matrix in Eq. (3.42) instead of the diagonal $\mathcal{E}_i$, one takes into account terms that are suppressed as $1/N$ or higher. In particular, one resums terms of the form $\alpha_s^k \ln^{2k-1} \bar{N}/N$ to all orders in α_s [55]. We will mostly stick to the ordinary resummation based on a diagonal evolution operator $\mathcal{E}_i$ in this paper. However, as we shall show later in one example, the subleading terms taken into account by implementing the non-diagonal evolution in the parton distributions and fragmentation functions can actually be quite relevant in kinematic regimes where one is further away from threshold. Here we will only take the LO part of evolution into account, extension to NLO is possible and has been discussed in [54].

For a complete NLL resummation one also needs the expansion of the integral in Eq. (4.16), which leads to

$$\ln \mathcal{S}_{N,ab\to cd}\left(\Delta\eta, \alpha_s(\mu), \frac{\mu}{\hat{m}}\right) \;=\; \frac{\ln(1-2\lambda)}{2\pi b_0}\, \Gamma^{(1)}_{ab\to cd}\left(\Delta\eta\right) \;. \qquad (3.46)$$

As in [22], we perform the exponentiation of the matrix on the right-hand-side numerically, by iterating the exponential series to an adequately large order.

3.3.3 Inverse of the Mellin and Fourier Transform

As we have discussed in detail, the resummation is achieved in Mellin moment space. In order to obtain a resummed cross section in τ space, one needs an inverse Mellin transform, accompanied by an inverse Fourier transform that reconstructs the dependence on $\bar{\eta}$. The Mellin inverse requires a prescription for dealing with the singularity in the perturbative strong coupling constant in Eqs. (3.34),(4.16) or in the NLL expansions, Eqs. (3.42),(3.43). We will use the *Minimal Prescription* developed in Ref. [87], which relies on use of the NLL expanded forms Eqs. (3.42),(3.43), and on choosing a Mellin contour in complex-N space that lies to the *left* of the poles at $\lambda = 1/2$ and $\lambda = 1$ in the

Mellin integrand. From Eqs. (3.25) and (3.26), we find

$$\Omega^{\rm resum}_{H_1H_2\to cd}\left(\tau',\Delta\eta,\bar\eta,\alpha_s(\mu),\frac{\mu}{\hat m}\right)=\frac{1}{2\pi}\int_{-\infty}^{\infty}d\nu\,{\rm e}^{-i\nu\bar\eta}\int_{C_{MP}-i\infty}^{C_{MP}+i\infty}\frac{dN}{2\pi i}\,(\tau')^{-N}$$
$$\times\sum_{ab}\tilde f_a^{H_1}(N+1+i\nu/2,\mu)\tilde f_b^{H_2}(N+1-i\nu/2,\mu)$$
$$\times\tilde\omega^{\rm resum}_{ab\to cd}\left(N,\nu,\Delta\eta,\alpha_s(\mu),\frac{\mu}{\hat m}\right)\,, \tag{3.47}$$

where the Mellin contour is chosen so that $b_0\alpha_s(\mu_R^2)\ln C_{MP}<1/2$, but all other poles in the integrand are as usual to the left of the contour. The result defined by the minimal prescription has the property that its perturbative expansion is an asymptotic series that has no factorial divergence and therefore no "built-in" power-like ambiguities [87]. Power corrections may then be added as phenomenologically required. For most of our discussion below, the resummed short-distance function $\tilde\omega^{\rm resum}_{ab\to cd}$ is specified directly by Eqs. (3.42) and (3.43). When we refer to "full singlet evolution", however, we make the identification in Eq. (3.45), and evolve the parton distributions and fragmentation functions to scale $\hat m/\bar N$. In this case the exponential in $\tilde\omega^{\rm resum}_{ab\to cd}$ is found from the $h_i^{(1)}$ and $h_i^{(2)}$ terms only in Eq. (3.42).

We note that the parton distribution functions in moment space fall off with an inverse power of the Mellin moment, typically as $1/N^4$ or faster. This helps very significantly to make the inverse Mellin integral in Eq. (3.47) numerically stable. In particular, the resulting functions $\Omega^{\rm resum}_{H_1H_2\to cd}$ are very well-behaved at high τ'. This would be very different if one were to invert just the resummed partonic cross sections $\tilde\omega^{\rm resum}_{ab\to cd}$ and attempt to convolute the result with the parton distributions. The good behavior of the $\Omega^{\rm resum}_{H_1H_2\to cd}$ makes it straightforward numerically to insert them into Eq. (3.23), where they are convoluted with the fragmentation functions in terms of momentum fractions z at fixed rapidities. At this stage, it is straightforward to impose cuts in the transverse momenta and rapidities of the observed particles. This gives the final hadronic cross section $M^4d\sigma^{H_1H_2\to h_1h_2X}/dM^2d\Delta\eta d\bar\eta$. We note that because of the presence of the Landau pole and the definition of the Mellin contour in the minimal prescription, the inverted $\Omega^{\rm resum}_{H_1H_2\to cd}$ has support at $\tau'>1$, where it is however decreasing exponentially with τ'. The numerical contribution from this region is very small (less than 1%) for all of the kinematics relevant for phenomenology.

When performing the resummation, one of course wants to make full use of the available fixed-order cross section, which in our case is NLO ($\mathcal{O}(\alpha_s^3)$). Therefore, a matching to this cross section is appropriate, which may be

achieved by expanding the resummed cross section to $\mathcal{O}(\alpha_s^3)$, subtracting the expanded result from the resummed one, and adding the full NLO cross section. Schematically:

$$d\sigma^{\rm match} = \left(d\sigma^{\rm resum} - d\sigma^{\rm resum}\Big|_{\mathcal{O}(\alpha_s^3)} \right) + d\sigma^{\rm NLO} \,. \tag{3.48}$$

In this way, NLO is taken into account in full, and the soft-gluon contributions beyond NLO are resummed to NLL. Any double-counting of perturbative orders is avoided.

3.4 Phenomenological Results

We now compare our resummed calculations to experimental di-hadron production data given as functions of the pair mass, M. These are available from the fixed-target experiments NA24 [34] (pp scattering at beam energy $E_p = 300$ GeV), E711 [35] (protons with $E_p = 800$ GeV on Beryllium), and E706 [36] (pp and pBe with $E_p = 500$ and 800 GeV), as well as from the ISR pp collider experiment CCOR [37] which produced data at $\sqrt{S} = 44.8$ and 62.4 GeV. The data sets refer to a $\pi^0\pi^0 X$ final state, with the exception of E711, which measured the final states h^+h^+X, h^-h^-X, h^+h^-X with h summed over all possible hadron species. When presenting our results for this data set, we will follow [39] to consider for simplicity only the *summed* charged-hadron combination $(h^+ + h^-)(h^+ + h^-)X$. For this combination also the information on the fragmentation functions is more reliable than for individual charge states.

In each of the experimental data sets, kinematic cuts have been applied. These are variously on the individual hadron transverse momenta $p_{T,i}$ or rapidities η_i, or on variables that are defined from both hadrons, $\cos\theta^*$, Y, $p_T^{\rm pair}$. Here $\cos\theta^*$ is the mean of the cosines of the angles between the observed hadron directions and the closest beam directions, in a frame where the produced hadrons have equal and opposite longitudinal momenta, $p_{T,1}\sinh\eta_1 = -p_{T,2}\sinh\eta_2$ [34–37, 39]. This system approximately coincides with the partonic c.m.s. In terms of the observed transverse momenta and rapidity difference one has:

$$\cos\theta^* = \frac{1}{2}\left(\frac{p_{T,1}}{p_{T,2} + p_{T,1}\cosh(2\Delta\eta)} + \frac{p_{T,2}}{p_{T,1} + p_{T,2}\cosh(2\Delta\eta)} \right) \sinh(2\Delta\eta) \,. \tag{3.49}$$

Furthermore, Y is the rapidity of the pion pair,

$$Y = \frac{1}{2}\ln\left(\frac{\kappa^0+\kappa^3}{\kappa^0-\kappa^3}\right) = \bar{\eta} - \frac{1}{2}\ln\left(\frac{p_{T,1}\,\mathrm{e}^{-\Delta\eta}+p_{T,2}\,\mathrm{e}^{\Delta\eta}}{p_{T,1}\,\mathrm{e}^{\Delta\eta}+p_{T,2}\,\mathrm{e}^{-\Delta\eta}}\right)\,, \tag{3.50}$$

where $\kappa = K_1+K_2$ is the pair's four-momentum and where the second equality in terms of $\Delta\eta$, $\bar{\eta}$ and the hadron transverse momenta $p_{T,i}$ holds for LO kinematics as appropriate in the threshold regime. Finally, p_T^{pair} is the transverse momentum of the pion pair,

$$p_T^{\mathrm{pair}} = |\mathbf{p}_{T,1}+\mathbf{p}_{T,2}| = |p_{T,1}-p_{T,2}|\,, \tag{3.51}$$

where again the second equality holds to LO. Thanks to our way of organizing the threshold resummed cross section, inclusion of cuts on any of these variables is straightforward.

In all our calculations, we use the CTEQ6M5 set of parton distribution functions [56], along with its associated value of the strong coupling constant. We also use the "de Florian-Sassot-Stratmann" (DSS) fragmentation functions [57]. We choose for our calculations the renormalization and factorization scales to be equal, and we give them the values M and $2M$, in order to investigate the scale dependence of the results. One expects that a natural scale choice would be offered by the hard scale in the partonic scattering, which is $\mathcal{O}(\hat{m})$. Because of the relation $M = \hat{m}\sqrt{z_c z_d}$, the scale M is actually significantly lower than $\hat{m}$, typically by a factor 2. Our scale choices of M and $2M$ therefore roughly correspond to scales $\hat{m}/2$ and $\hat{m}$, and we refrain from using a scale lower than $\mu = M$ since this would correspond to a rather low scale at the partonic hard scattering.

Figure 3.1 shows the comparison to the NA24 [34] data for $pp \to \pi^0\pi^0 X$ at $\sqrt{S} = 23.7$ GeV. The cuts employed by NA24 are $|\cos\theta^*| < 0.4$, average over $|Y| < 0.35$, and $p_T^{\mathrm{pair}} < 1$ GeV. We start by comparing the full NLO cross section to the first-order expansion of the resummed expression, that is, the last two terms in Eq. (3.48). This will help to gauge to what extent the soft-gluon terms constitute the dominant part of the cross section, so that their resummation is reliable. It turns out that the two terms agree to a remarkable degree. The dashed lines in Fig. 3.1 show the NLO cross section for scales $2M$ (lower) and M (upper), while the crosses give the NLO expansion of the resummed cross section. Their difference actually never exceeds 1% for the kinematics relevant for NA24. The solid lines in the figure present the full, and matched, resummed results, including "C-coefficients" implemented as described in Sec. 3.3.2 (see Eq. (3.41)). One can see that resummation leads to a very significant enhancement of the theoretical prediction. A very good

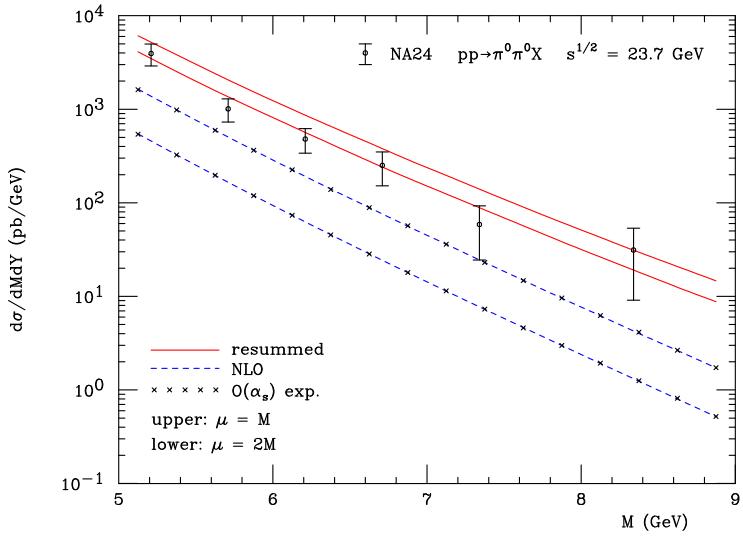

Figure 3.1: *Comparison of the NLO (dashed) and resummed (solid) calculations to the NA24 data [34], for two different choices of the renormalization and factorization scales, $\mu = M$ (upper lines) and $\mu = 2M$ (lower lines). The crosses display the NLO $\mathcal{O}(\alpha_s)$ expansion of the resummed cross section.*

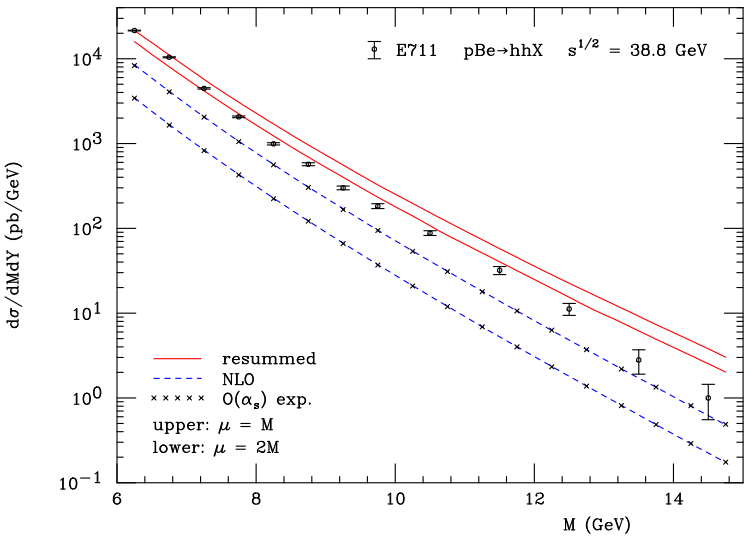

Figure 3.2: *Same as Fig. 3.1, but for charged-hadron production for pp scattering at $\sqrt{S} = 38.8$ GeV and with cuts appropriate for comparison to E711. The data are from [35].*

description of the NA24 data [34] is obtained, much better than for the NLO calculation which falls short of the data unless rather low renormalization and factorization scales are used. Also the scale dependence of the calculated cross section is much reduced by resummation.

We next turn to the cross section for charged-hadron production, $pBe \to h^{\pm}h^{\pm}X$, measured by E711 [35] at $\sqrt{S} = 38.8$ GeV. We recall that we sum over the charges of the produced hadrons. The cuts applied by E711 were $p_{T,i} > 2$ GeV, and average over $-0.4 < |Y| < 0.2$. The cut on the individual hadron transverse momenta is, in fact, irrelevant for the values of M considered here. Furthermore, as stated in their Fig. 6 [35] for the pair mass distribution we apply $p_T^{\rm pair} < 2$ GeV, and $0.1 < |\cos\theta^*| < 0.25$. Figure 3.2 shows the data and our results. As before, the agreement between NLO and the NLO expansion of the resummed calculation is excellent. Again, resummation leads to an increase of the predicted cross section and a reduction of scale dependence. Even though the resummed result agrees with the data much better than the NLO one for the scale we have chosen, it tends to lie somewhat above the data, in particular at the highest values of M. Keeping in mind the results for NA24, one may wonder if this might be in part related to the fragmentation functions for summed charged hadrons, which are probably slightly less well understood than those for pions, due to the contributions from the heavier kaons and, in particular, baryons.

Figures 3.3 and 3.4 show the comparison of our results to the E706 data sets for neutral pion pair production in pp and pBe scattering at $\sqrt{S} = 38.8$ GeV (800 GeV beam energy), respectively. We do not take into account any nuclear effects for the Beryllium nucleus, except for the trivial isospin one. This has a very minor effect on the cross section, compared to pp. E706 used cuts fairly different from those applied in the data we have discussed so far. There were no explicit cuts on $\cos\theta^*$, $p_T^{\rm pair}$ or Y, but instead cuts $p_{T,i} > p_T^{\rm cut} = 2.5$ GeV and either $-1.05 < \eta_i < 0.55$ (for the $\sqrt{S} = 38.8$ GeV data) or $-0.8 < \eta_i < 0.8$ (for the $\sqrt{S} = 31.6$ GeV data) on the transverse momenta and rapidities of the individual pions. The cut on transverse momentum, in particular, has a strong influence at the lower M: in a rough approximation, it leads to a kinematic limit $M \sim 2p_{T,i} > 5$ GeV, so that the cross section has to decrease very rapidly once one decreases M toward 5 GeV. This behavior is indeed seen in the figures.

As in the previous cases, the NLO expansion of the resummed and the full NLO cross section agree extremely well, typically to better than 2%. For the two scales we have chosen, the NLO cross sections fall well short of the data. It was noted in [39, 40] that in order for NLO to match the data, very low scales of $\mu = 0.35M$ have to be chosen. The resummed cross section, on the other

hand, has much reduced scale dependence and describes the data very well for the more natural scales M and $2M$, except at the lower M where the cut $p_T^{\rm cut}$ on the $p_{T,i}$ becomes relevant. One observes that the data extend to lower M than the theoretical cross section, which basically cuts off at $M = 5$ GeV as discussed above. A new scale becomes relevant here, the difference $|M-2p_T^{\rm cut}|$. Higher order effects associated with this scale (which are different from the ones addressed by threshold resummation) and/or non-perturbative effects such as intrinsic transverse momenta [36] probably control the cross section here. It is also instructive to see that the cross section is very sensitive to the actual value of the cut on the $p_{T,i}$. In Fig. 3.5 we show the resummed results for scale $\mu = 2M$ for $p_{T,i} > 2.5$ GeV (as before) and $p_{T,i} > 2.2$ GeV. One can see that with the lower cut the data are much better described. Experimental resolution effects might therefore have a significant influence on the comparison between data and theory here.

In order to check consistency, E706 also presented their pBe data set at $\sqrt{S} = 38.8$ GeV when the E711 cuts were applied instead of the E706 default ones. These data are found in [36]. Figure 3.6 shows the comparison for this case. One can see the same trends as before. Clearly, the description of the data by the resummed calculation is excellent. For this set of cuts, the cross section is not forced to turn down by kinematics at the lower M, and theory and data agree well everywhere. Figures 3.7 and 3.8 show results corresponding to Figs. 3.3, 3.4, but for the lower beam energy, 530 GeV, employed by E706 ($\sqrt{S} = 31.6$ GeV).

We finally turn to the data sets available at the highest energy, which are from the CCOR experiment at the ISR [37]. Two data set are available, at $\sqrt{S} = 44.8$ GeV and 62.4 GeV. The cuts employed by CCOR were identical to those of NA24, $|\cos\theta^*| < 0.4$, average over $|Y| < 0.35$, and $p_T^{\rm pair} < 1$ GeV. Figure 3.9 shows our results at $\sqrt{S} = 44.8$ GeV. The resummed calculation again shows decreased scale dependence and describes the data much better than the NLO one. At the lower values of M, it does show a tendency to lie above the data. Barring any issue with the data (which appear to have a certain unexpected "shoulder" around $M = 10$ GeV or so), this might indicate that one gets too far from threshold for resummation to be very precise. On the other hand, the agreement between full NLO and the NLO expansion of the resummed cross section still remains very good, as can be seen from the figure. The trend for resummation to give results higher than the data becomes more pronounced at the higher energy, $\sqrt{S} = 62.4$ GeV, as Fig. 3.10 shows. Although not easily seen from the figure, the NLO expansion of the resummed cross section starts to deviate more from the full NLO cross section than at the lower energies. At the lower M shown, it can be higher by up to 7%, which

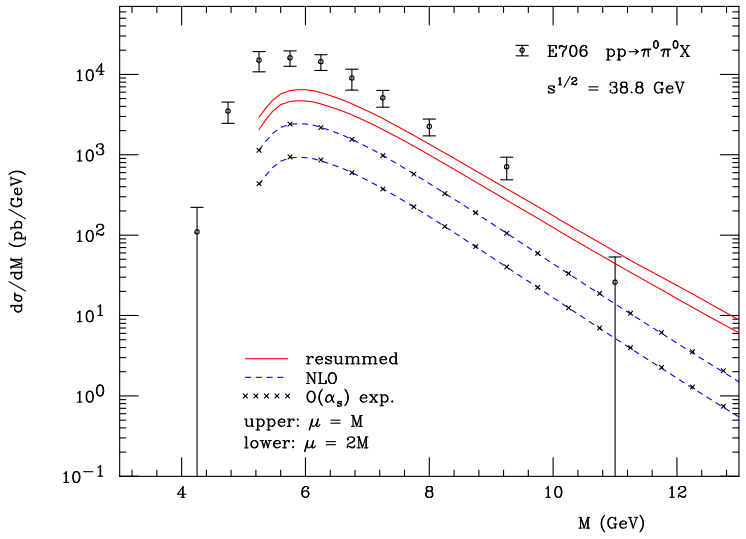

Figure 3.3: *Same as Fig. 3.1, but with cuts appropriate for comparison to E706 at* $\sqrt{S} = 38.8$ *GeV. The data are from [36].*

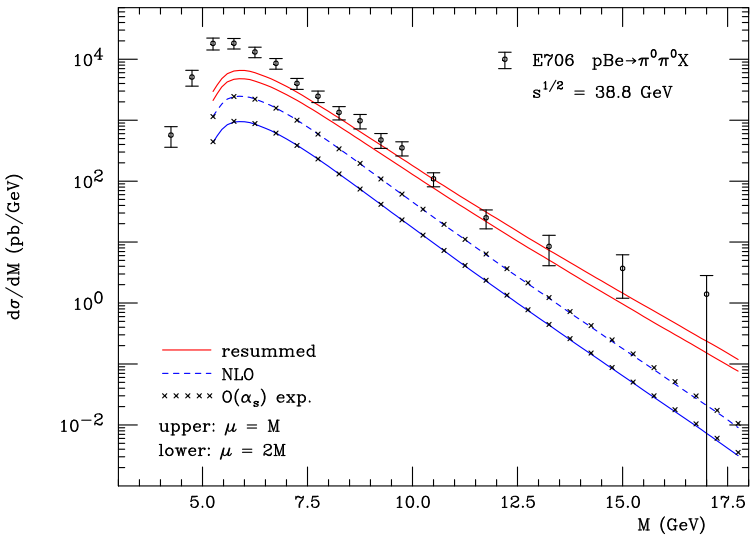

Figure 3.4: *Same as Fig. 3.3, but for proton-Beryllium scattering.*

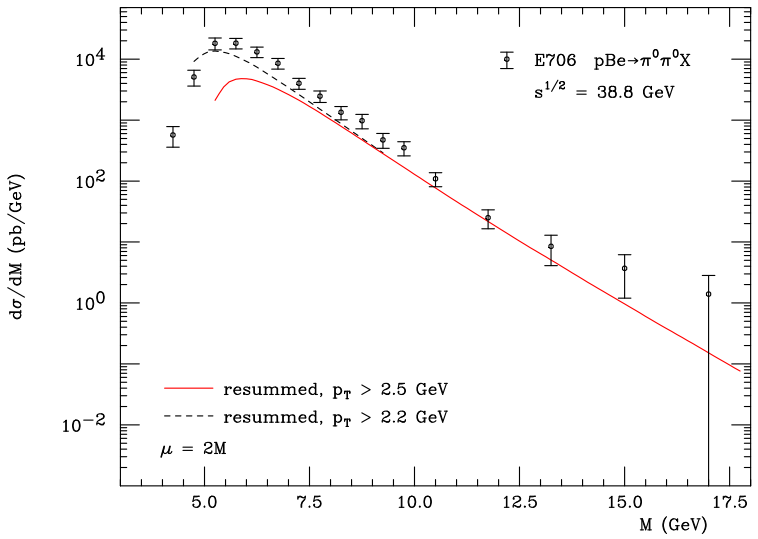

Figure 3.5: *Resummed cross section for scale $\mu = 2M$ and $p_{T,i} > 2.2$ GeV (dashed), compared to the one with $p_{T,i} > 2.5$ GeV shown previously in Fig. 3.4 (solid).*

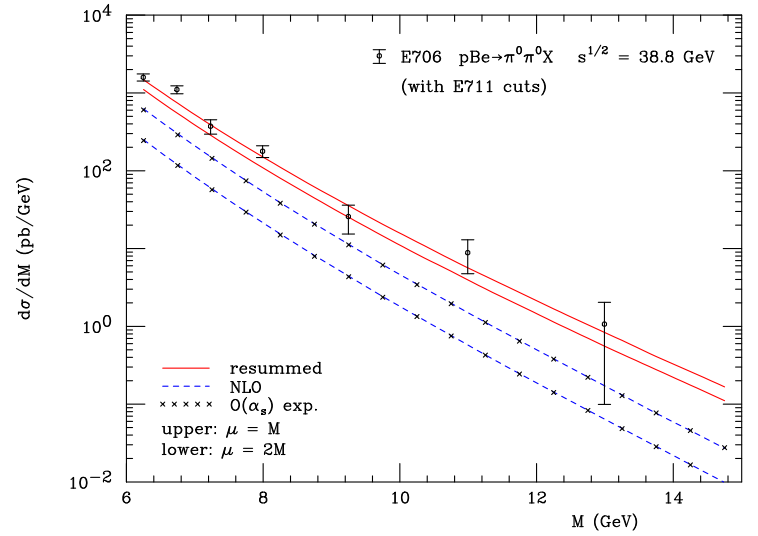

Figure 3.6: *Comparison to E706 data with a different set of cuts, corresponding to the ones applied by E711. The data with these cuts are from [36].*

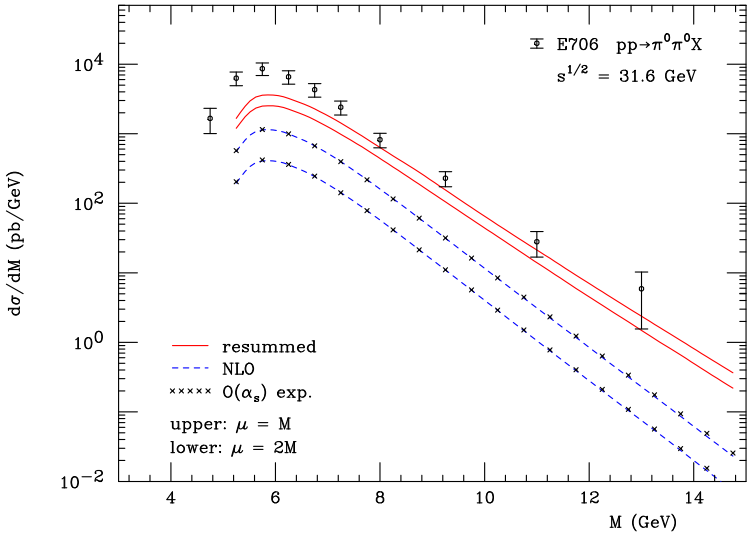

Figure 3.7: *Same as Fig. 3.3, but at* $\sqrt{S} = 31.6$ *GeV.*

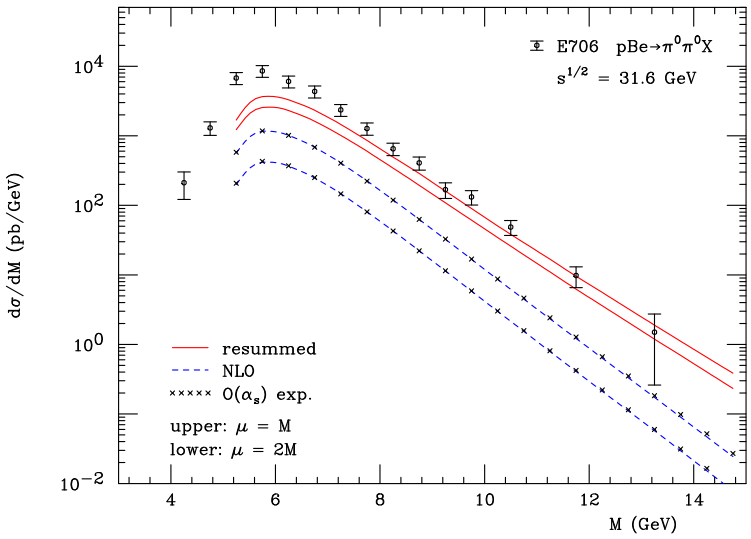

Figure 3.8: *Same as Fig. 3.4, but at* $\sqrt{S} = 31.6$ *GeV.*

is still a relatively minor deviation, but could be indicative of the reason why the resummed result is high as well.

Clearly, any deviation between the full NLO cross section and the NLO expansion of the resummed one is due to terms that are formally suppressed by an inverse power of the Mellin moment N near threshold. It is therefore interesting to explore the likely effects of such terms. This can be done by promoting the LO anomalous dimension in the evolution part in Eq. (3.42) from its diagonal form to the full one, as described in Sec. 3.3.2:

$$-2A_i^{(1)} \ln \bar{N} - B_i^{(1)} \to P_{ij}^{(1),N} \,, \tag{3.52}$$

which includes the subleading terms in $1/N$ and full singlet mixing. For simplicity, we perform this modification only for the lowest order part of evolution, as indicated in Eqs. (3.43) and (3.52). The results obtained in this way are shown in Fig. 3.11. One can see that the resummed result obtained in this way indeed decreases significantly with respect to the one in Fig. 3.10 which was based on the diagonal evolution only, and is much closer to the data. At the same time, the agreement between the NLO cross section and the $\mathcal{O}(\alpha_s)$ expanded resummed result becomes as good as what we encountered in the fixed-target case. Figure 3.12 presents the corresponding result for the case of NA24. Comparison with Fig. 3.1 shows that the effect of the subleading terms is much smaller here, as expected from the fact that one is closer to threshold in the case of NA24. Nonetheless, the effects lead to a slight further improvement between the resummed calculation and the data. In particular, they give the theoretical result a somewhat flatter behavior, which follows the trend of the data more closely overall. While the implementation of subleading terms in this way will require further study, this appears to be a promising approach for extending the applicability of threshold resummation into regimes where one is relatively far away from threshold.

That said, we remind the reader that already in the part that is leading near threshold we have made the approximation in Eq. (3.41) for our "C-coefficients". This, too, will need to be improved in the future, by taking into account the full color structure of the hard scattering function beyond LO, as we discussed in Sec. 3.3.2. To give a somewhat extreme example of the effects generated by the C-coefficients, we have re-computed the resummed cross section for the case of CCOR at $\sqrt{S} = 62.4$ GeV, but leaving out all effects of the the coefficients *beyond NLO*. In other words, we leave out the C-coefficients in the first two terms on the right-hand-side of Eq. (3.48), keeping them of course in $d\sigma^{\rm NLO}$. This is likely not a good approximation of the beyond-NLO hard coefficients, because the $C^{(1)}_{ab\to cd}$ have π^2 terms and logarithms in the renormalization scale μ that are independent of the color channel and truly

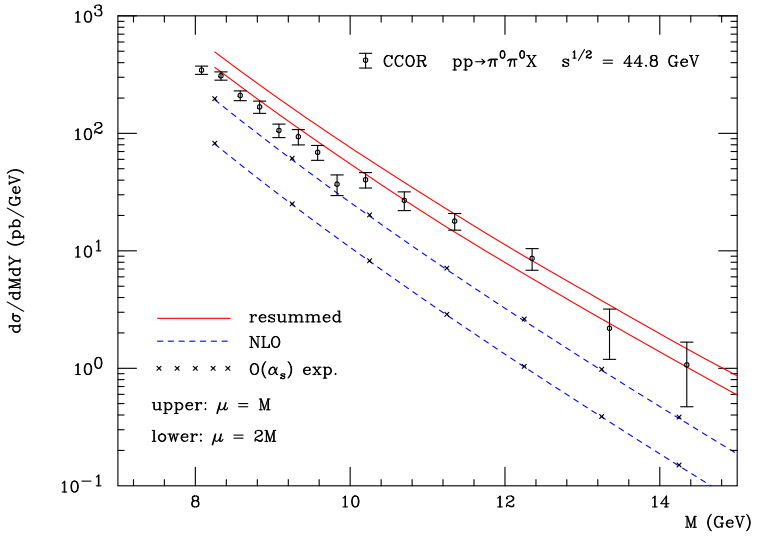

Figure 3.9: *Comparison of the NLO (dashed) and resummed (solid) calculations to the CCOR data [34] at* $\sqrt{S} = 44.8$ *GeV, for two different choices of the renormalization and factorization scales,* $\mu = M$ *(upper lines) and* $\mu = 2M$ *(lower lines). The crosses display the NLO* $\mathcal{O}(\alpha_s)$ *expansion of the resummed cross section.*

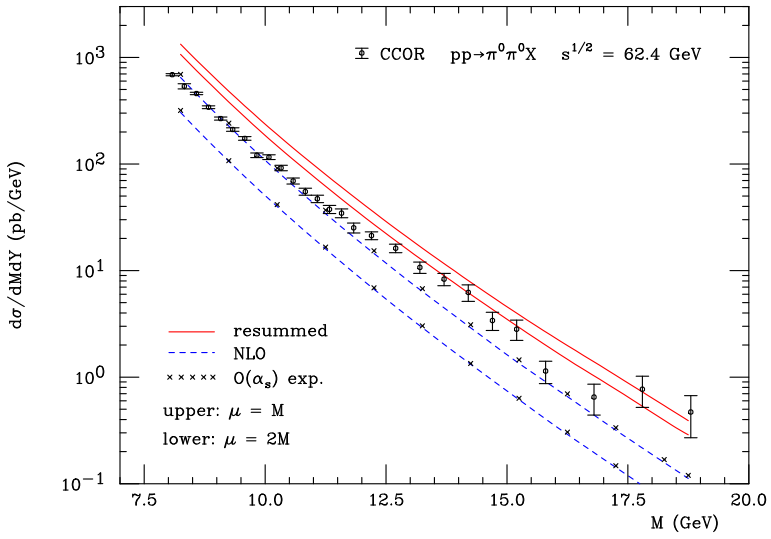

Figure 3.10: *Same as Fig. 3.9, but for* $\sqrt{S} = 62.4$ *GeV.*

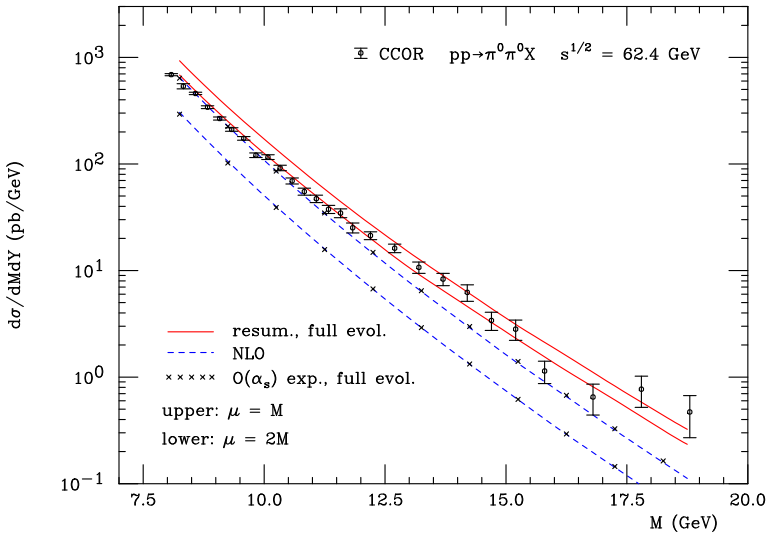

Figure 3.11: *Same as Fig. 3.10, but extending the diagonal evolution in the resummed formula to included subleading terms and singlet mixing, as shown in Eq. (3.52).*

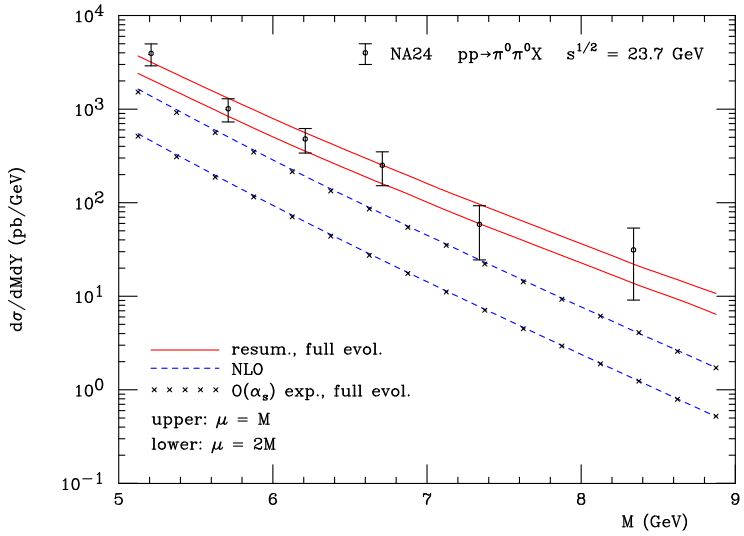

Figure 3.12: *Same as Fig. 3.11, but for the case of NA24.*

enter in the form given in Eq. (3.41). Some of these are in fact even known to exponentiate [20, 43, 44, 52, 58]. In any case, the result of this exercise is shown in Fig. 3.13, where it is also compared to our earlier calculation that included the C-coefficients in the way discussed in Sec. 3.3.2. One can see that there is a sizable numerical difference, and that the scale dependence of the resummed result without the beyond-NLO C-coefficients becomes significantly worse.

We finally turn to the distribution in $\cos\theta^*$, defined in Eq. (3.49), for which most of the experiments mentioned above have presented data as well. In fact, the CCOR data [37] for this observable were instrumental in establishing the QCD hard-scattering nature of pp interactions [59]. From the point of view of threshold resummation, the distribution in $\cos\theta^*$ may appear somewhat less interesting than the pair mass one, since the threshold logarithms arise in $1-\hat{\tau} = 1-\hat{m}^2/\hat{s}$, regardless of $\cos\theta^*$. In addition, the $\cos\theta^*$ distributions are presented as normalized distributions of the form

$$\frac{d\sigma/d\cos\theta^*}{d\sigma/d\cos\theta^*|_{\cos\theta^*=0}} \,, \tag{3.53}$$

so that the main enhancement generated by threshold resummation is expected to cancel. Nonetheless, as we have seen in Sec. 3.3.2, the resummed expressions do contain additional dependence on $\Delta\eta$ beyond that present in the Born cross sections, which will affect the $\cos\theta^*$ distribution at higher orders. This is visible from the soft part in Eq. (3.46) and also from the "C-coefficients" in Eq. (3.41). Rather than going through an exhaustive comparison to all the available data, we just consider one example that is representative of the effects of threshold resummation on the $\cos\theta^*$ distribution. Figure 3.14 shows the normalized distribution for the E711 case, where we have again summed over all charge states of the produced hadrons. The dashed lines show the NLO result calculated again with the code of [39], for scales $\mu = 2M$ and $\mu = M$. One can see that for these scales the NLO calculation is lower than the data for higher values of $\cos\theta^*$. The dot-dashed lines in Fig. 3.14 show the resummed results for scales $\mu = 2M$ and $\mu = M$. These show a steeper rise with $\cos\theta^*$ and describe the data better than NLO for the scales shown. However, they still tend to lie below the data at higher values of $\cos\theta^*$. As was suggested in [37, 39, 40], for the $\cos\theta^*$ distribution the hard scale in the partonic process will itself be a function of $\cos\theta^*$, so that it is more natural to choose a factorization/renormalization scale that reflects this feature. We therefore present our resummed results also for scales $\mu = 2M^*$ and $\mu = M^*$, where $M^{*2} = M^2(1-\cos\theta^*)$ which is proportional to the Mandelstam variable $\hat{t}$ in the partonic process. One observes that with these scale choices a very

good description of the data is achieved. We note that in the NLO calculations presented in Refs. [39, 40] the scale was chosen proportional to the (average) transverse momenta of the produced hadrons, which for given M also depend on $\cos\theta^*$. This resulted in a satisfactory description of the data, when scales effectively a factor two smaller than our M^* were used. Overall, the trend for the resummed $\cos\theta^*$ distribution to lie higher than NLO and be in better agreement with the data is found to be a generic feature that occurs as well for the cases of the other experiments.

3.5 Conclusions

We have investigated the effects of next-to-leading logarithmic threshold resummation on the cross section for di-hadron production in hadronic collisions, $H_1H_2 \to h_1h_2X$, for a range of invariant masses of the produced hadron pair. We have developed techniques to implement the resummation formalism at fixed rapidities for the produced hadrons and for all relevant experimental cuts. Extensions of these techniques to the level of next-to-next-lo-leading logarithms should be relatively straightforward in light of the close relation between the one- and two-loop soft anomalous dimension matrices [60].

For the fixed target and collider data studied here, the one-loop expansions of our resummed expressions approximate the corresponding exact one-loop cross sections excellently, to the level of a few percent and often less. In addition, with scales chosen to match the underlying hard scattering, the matched resummed cross sections typically explain the available data better than do NLO expressions at similar scales, with significantly reduced scale dependence.

An important extension of these methods will be in the production and fragmentation of heavy quarks and in jet cross sections, where similar resummation methods are applicable. Given the reduction in scale dependence, this could provide an improved control over Standard Model tests and backgrounds in new physics searches.

In the next chapter we study the effects of resummation in top anti-top production. We take a special look at a particular observable, the charge asymmetry in top anti-top production.

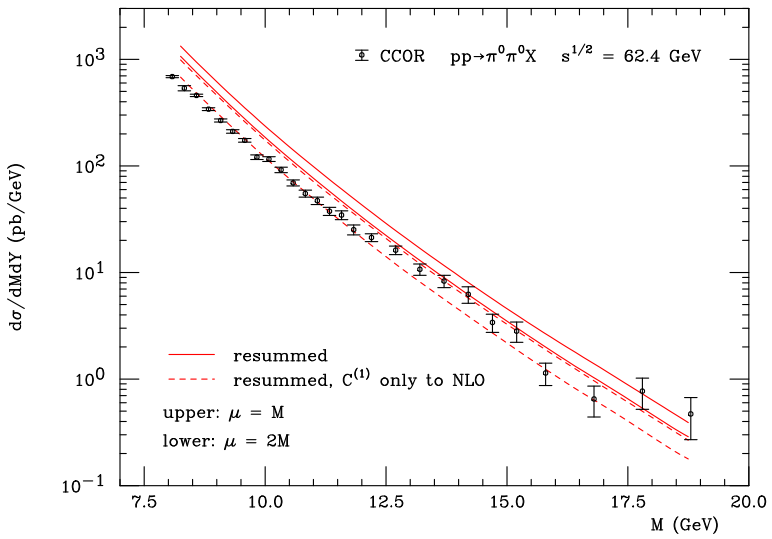

Figure 3.13: *Resummed results for the case of CCOR at* $\sqrt{S} = 62.4$ *GeV. The solid lines show the results for scales* M *and* $2M$ *shown previously in Fig. 3.10, while the dashed ones were obtained by neglecting the contributions by the* $C^{(1)}_{ab\to cd}$ *coefficients beyond NLO.*

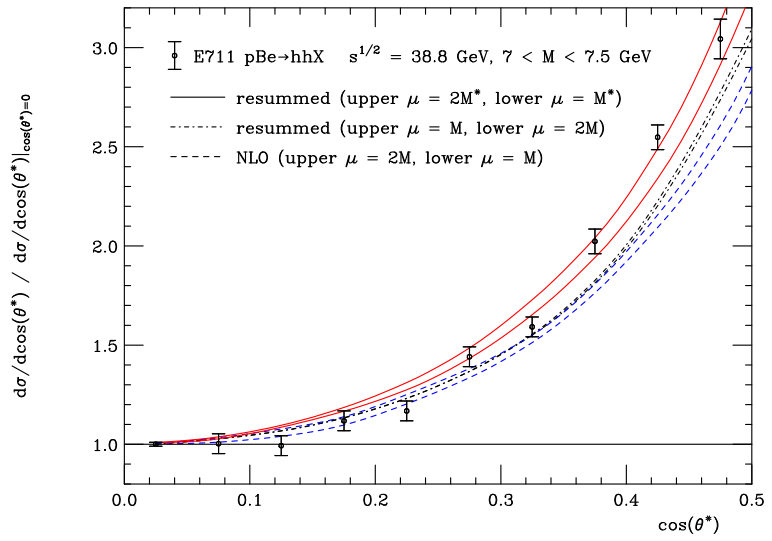

Figure 3.14: *Normalized distribution in* $\cos\theta^*$ *(see (3.53)) for the case of charged-hadron production at E711. Dashed is NLO, while the dot-dashed and solid lines show resummed results. For the latter we have also used the scales* $\mu = M^*$ *and* $\mu = 2M^*$*, where* $M^{*2} = M^2(1 - \cos\theta^*)$.

Chapter 4

Charge Asymmetry in Top Production

4.1 Introduction

Heavy quark pair production in hadronic collisions is important both for accurate tests of the Standard Model and in searches for New Physics. Thanks to the large scale set by the mass of the heavy quark, one can often use QCD perturbation theory in obtaining predictions for heavy-flavor production, employing the factorization of the hadronic cross section into parton distribution functions and perturbative short-distance cross sections.

Top quark production may provide an arena for testing possible extensions of the Standard Model [62–65]. One particularly interesting observable in $t\bar{t}$ production that has been considered in this context [66, 67] is the *charge asymmetry* (or, forward-backward asymmetry), which is obtained by comparing the rate for producing a top quark at a given angle to that for producing an anti-top at the same angle. Electro-weak processes, as well as processes in many extensions of the Standard Model, may produce a charge asymmetry at Born level. QCD, on the other hand, being a purely vector theory, does not produce a charge asymmetry in the lowest-order (LO) processes $q\bar{q} \to t\bar{t}$ and $gg \to t\bar{t}$. The charge asymmetry thus has the potential of probing or constraining possible tree-level axial couplings of the gluon [66, 67] at the Tevatron or the LHC.

Starting at order α_s^3, however, QCD itself contributes to the charge asymmetry, through $q\bar{q}$ annihilation $q\bar{q} \to t\bar{t}(g)$ and flavor excitation, $qg \to q\,t\bar{t}$ [68]. This happens through diagrams in which two separate fermion lines (one of them the top quark line) are connected by three gluons. This phenomenon, which is also well-known in QED [69], enters with the combination $d_{abc}d^{abc}$ of

the symmetric QCD structure constants. The same mechanism for light flavors has been found to generate a strange quark $s - \bar{s}$ asymmetry in the nucleon sea [70]. The charge asymmetric part is contained in the full next-to-leading order (NLO, $\mathcal{O}(\alpha_s^3)$) calculations of the differential heavy-flavor production cross section [71–73]. Since this is the order at which the effect arises for the first time, we will usually refer to the charge asymmetric part arising at $\mathcal{O}(\alpha_s^3)$ as LO. There have been detailed calculations and phenomenological studies of the QCD top quark charge asymmetry at the Tevatron (or the LHC), both for the inclusive case, $p\bar{p} \to t\bar{t}X$ [67, 74], and for associated-jet final states, $p\bar{p} \to t\bar{t}\,\mathrm{jet}X$ [75, 76]. In particular, Ref. [76] provides the full NLO ($\mathcal{O}(\alpha_s^4)$) corrections to $p\bar{p} \to t\bar{t}\,\mathrm{jet}X$.

Very recently, first measurements of top quark charge asymmetries have been reported by the Tevatron collaborations [77, 78]. In the inclusive case, asymmetries of $12 \pm 8\,(\mathrm{stat.}) \pm 1(\mathrm{syst.})\%$ and $23 \pm 12\,(\mathrm{stat.}) \pm 6(\mathrm{syst.})\%$ were found by D0 [77] and CDF [78], respectively. Even though experimental uncertainties are evidently still large, this is a very encouraging first step that motivates further theoretical investigations. In the present paper we improve the theoretical framework for the case of the inclusive charge asymmetry by examining the effects of QCD threshold resummation. This will provide insight into the important question of how robust the asymmetry is with respect to higher order QCD corrections. Our study requires us to implement NLL resummation in heavy quark production at fixed angle and rapidity [20, 21]. Earlier phenomenological studies of the threshold-resummed $t\bar{t}$ cross section, which however did not focus on the charge asymmetry, may be found in [79–82].

As is well-known, when the initial partons have just enough energy to produce a $t\bar{t}$ pair, the phase space available for gluon bremsstrahlung nearly vanishes, giving rise to large logarithmic corrections to the partonic cross section. For example, if we consider the cross section for $t\bar{t}$ production at fixed pair invariant mass, this partonic threshold is reached when the pair invariant mass equals the partonic center of mass (c.m.) energy, $M_{t\bar{t}}^2 = s$. At the nth order of perturbation theory, the large threshold corrections arise as $\alpha_s^{2+n} \left[\log^m(1-\hat{\tau})/(1-\hat{\tau})\right]_+$ with $m \leq 2n-1$, where $\hat{\tau} = M_{t\bar{t}}^2/s$ and the "+"-distribution will be reviewed below. The maximum value, $m = 2n-1$ corresponds to the leading logarithms (LL), $m = 2n-2$ to next-to-leading logarithms (NLL), and so forth. Near threshold, the perturbative calculation produces potentially large corrections at all orders in the strong coupling, α_s. These corrections are addressed by threshold resummation. This is particularly relevant for the Tevatron case, where the hadronic c.m. energy is not too much larger than twice the top mass, $2m_t$, so that $\hat{\tau}$ is on average rather

close to unity. Related considerations also apply at the LHC when the pair is produced with $M_{t\bar{t}}^2 \gg 4m_t^2$.

For heavy quark production, threshold resummation has been derived to NLL accuracy [20, 80]. The results of [20] have been presented for arbitrary c.m. scattering angle of the produced top quark, which makes it possible to obtain a resummed charge asymmetry from them. Among the processes that contribute to the charge asymmetry, only $q\bar{q}$ annihilation contains threshold logarithms, while the flavor excitation qg process is suppressed near threshold. As we shall discuss in some detail, it turns out that the leading logarithms in the charge asymmetric part of $q\bar{q}$ annihilation cancel at $\mathcal{O}(\alpha_s^3)$. This is because the charge asymmetric part is a difference of cross sections with the top or the anti-top produced at a certain angle, and the leading logarithms enter in association with the $\mathcal{O}(\alpha_s^2)$ $q\bar{q} \to t\bar{t}$ Born process, which is charge symmetric. We shall return to this point below, and will find that beyond $\mathcal{O}(\alpha_s^2)$ the charge asymmetric cross section is enhanced by the same threshold logarithms as the symmetric one. We also note that the gg fusion process is charge symmetric to all orders; nonetheless its resummation can be relevant also for the charge asymmetry as it contributes to the denominator of the asymmetry and may thus dilute it somewhat. This effect does not lead to significant suppression, however, because of the higher-order threshold enhancements to the asymmetric cross section, which we will exhibit below.

The remainder of this chapter is organized as follows. In Sec. 4.2 we give the basic formulas associated with the charge asymmetry and discuss the near-threshold behavior at $\mathcal{O}(\alpha_s^2)$. In Sec. 3 we present the relevant expressions for the NLL resummed $t\bar{t}$ cross section as a function of the $t\bar{t}$ pair invariant mass and the top c.m. scattering angle. Section 4 presents our phenomenological results for Tevatron kinematics, and we summarize our findings in Sec. 5.

4.2 Perturbative Cross section, and Charge Asymmetry

We consider inclusive $t\bar{t}$ production in hadronic collisions,

$$H_A(P_A) + H_B(P_B) \to t(p_t)\bar{t}(p_{\bar{t}}) + X(p_X), \tag{4.1}$$

where we have indicated the momenta. We introduce the invariant mass squared of the $t\bar{t}$ pair: $M_{t\bar{t}}^2 = (p_t + p_{\bar{t}})^2$, and the variable $\tau \equiv M_{t\bar{t}}^2/S$ with $S = (P_A + P_B)^2$. The factorized cross-section for the process is written in terms of convolutions of parton distributions $f_a^{H_A}$ and $f_b^{H_B}$ for partons a,b in hadrons H_A, H_B, respectively, with perturbative partonic hard-scattering

cross-sections $\hat{\sigma}_{ab}$:

$$\frac{d^2\sigma^{H_A H_B \to t\bar{t}X}}{dM_{t\bar{t}}^2\, d\cos\theta} = \sum_{ab} \int_0^1 dx_a \int_0^1 dx_b\, f_a^{H_A}(x_a,\mu^2) f_b^{H_B}(x_b,\mu^2) \times \frac{1}{s} \frac{d^2\hat{\sigma}_{ab}(\hat{\tau},\cos\theta,\mu^2/s)}{d\hat{\tau}\, d\cos\theta}, \tag{4.2}$$

where the sum runs over all partonic subprocesses that produce top quark pairs. We have introduced the partonic variable $\hat{\tau} = M_{t\bar{t}}^2/s = \tau/x_a x_b$. We define θ as the production angle of the top quark in the partonic center-of-mass frame. We note from the outset that this is not the definition adopted in the Tevatron experiments, where the asymmetry is considered as a function of the rapidity difference Δy_t of the t and $\bar{t}$. However, for LO kinematics, the two definitions are directly related through [78] $\tanh(\Delta y/2) = \beta\cos\theta$, with $\beta = \sqrt{1-4m_t^2/s}$ the top quark velocity. As the partonic threshold regime is characterized by LO kinematics, we expect our resummed results below to be very faithful representations also of the effects expected for the Tevatron definition (see also [67]). In fact, we have found that for quantities integrated over angle the charge asymmetries for the two definitions agree at the level of about 2% or better. The integration limits in Eq. (4.2) are determined by the conditions [81] $s \geq M_{t\bar{t}}^2 \geq 4m_t^2/(1-\beta^2\cos^2\theta)$. Finally, the scale μ denotes the factorization and renormalization scales, which we take to be equal throughout this study.

We next define the charge-asymmetric and charge-averaged cross sections:

$$\frac{d\Delta\sigma}{dM_{t\bar{t}}^2 d\cos\theta} \equiv \frac{1}{2}\left\{\frac{d^2\sigma^{H_A H_B \to t\bar{t}X}}{dM_{t\bar{t}}^2 d\cos\theta} - \frac{d^2\sigma^{H_A H_B \to \bar{t}tX}}{dM_{t\bar{t}}^2 d\cos\theta}\right\},$$
$$\frac{d\bar{\sigma}}{dM_{t\bar{t}}^2 d\cos\theta} \equiv \frac{1}{2}\left\{\frac{d^2\sigma^{H_A H_B \to t\bar{t}X}}{dM_{t\bar{t}}^2 d\cos\theta} + \frac{d^2\sigma^{H_A H_B \to \bar{t}tX}}{dM_{t\bar{t}}^2 d\cos\theta}\right\},$$

and the corresponding charge asymmetry

$$A_c(M_{t\bar{t}}^2,\cos\theta) \equiv \frac{d\Delta\sigma}{d\sigma}\,. \tag{4.3}$$

To lowest order (LO), $t\bar{t}$ pairs are produced by the processes $q\bar{q} \to t\bar{t}$ and $gg \to t\bar{t}$. These produce the top and the anti-top evenly at a given production angle θ, so that the charge asymmetry vanishes. Beyond LO, however, $q\bar{q}$ annihilation as well as the flavor excitation process $qg \to t\bar{t}q$ have charge asymmetric contributions [74], while gg scattering remains symmetric. For the $q\bar{q}$ annihilation process, the asymmetry arises from three gluons connecting the

light-quark and the top-quark lines. In the case of inclusive $t\bar{t}$ production, the asymmetry receives contributions from real diagrams for $q\bar{q} \to t\bar{t}g$ and from virtual corrections in $q\bar{q} \to t\bar{t}$. The charge asymmetric pieces for the $\mathcal{O}(\alpha_s^3)$ subprocesses have been computed in detail in [74]; they are also included of course in the full next-to-leading order (NLO) calculations of the top quark cross section [71–73].

As we discussed in the Introduction, large double- and single-logarithmic corrections arise at higher orders in the partonic cross sections for $q\bar{q}$ annihilation and gg fusion when $\hat{\tau}$ becomes large, that is, when $M_{t\bar{t}}^2 \sim s$. The structure of the NLO terms in the $q\bar{q}$ annihilation cross section becomes, for example,

$$\begin{aligned} \frac{d^2\hat{\sigma}_{q\bar{q}}^{\rm NLO}(\hat{\tau},\cos\theta)}{d\hat{\tau}\,d\cos\theta} &= C_1(\theta)\delta(1-\hat{\tau}) + C_2(\theta)\left(\frac{1}{1-\hat{\tau}}\right)_+ \\ &\quad + C_3(\theta)\left(\frac{\log(1-\hat{\tau})}{1-\hat{\tau}}\right)_+ + \dots\,, \end{aligned} \tag{4.4}$$

where the ellipses denote terms that are suppressed near threshold. We have suppressed the dependence on the factorization/renormalization scale, as we will often do in the following. The "+"-distribution is defined as usual by

$$\int_x^1 dz\,[g(z)]_+\,f(z) = \int_x^1 dz\,g(z)\,(f(z)-f(1)) - f(1)\int_0^x dz\,g(z)\,. \tag{4.5}$$

The coefficients C_i may be found in Ref. [81]. It turns out that only C_1 and C_2 possess charge-asymmetric pieces, while the double-logarithmic part associated with C_3 is symmetric and thus cancels in the asymmetry at lowest order. This is a result of the factorization of collinear logarithms, which do not interfere with color flow in the hard scattering [20]. As a result, the charge asymmetric contributions in $q\bar{q} \to t\bar{t}g$ and $q\bar{q} \to t\bar{t}$ each have an infrared (but no collinear) singularity at $\mathcal{O}(\alpha_s^3)$ [74], which cancels in their sum and leaves behind a single logarithm, represented by the term proportional to $1/(1-\hat{\tau})_+$ in Eq. (4.4). We will see in the next section, however, that, starting with the next order, leading logarithms contribute to the asymmetric cross section as an overall factor.

4.3 NLL resummation

The resummation of the soft-gluon contributions is organized in Mellin-N moment space. We take a moment of the hadronic cross section with respect to

the variable τ:

$$\frac{d\sigma^N}{d\cos\theta} \equiv \int_0^1 d\tau \tau^{N-1} \frac{d^2\sigma}{d\tau d\cos\theta} \ . \tag{4.6}$$

Under Mellin moments, the convolutions in the factorized cross section near threshold become products:

$$\frac{d\sigma^N}{d\cos\theta} = \sum_{ab} f_a^{H_A,N}(\mu^2) f_b^{H_B,N}(\mu^2) \hat{\sigma}_{ab}(N,\theta) \ , \tag{4.7}$$

where the $f_a^{H_A,N}, f_b^{H_B,N}$ are the Mellin moments of the parton distributions, defined by analogy to Eq. (4.6), and where

$$\hat{\sigma}_{ab}(N,\theta) \ = \ \int_0^1 d\hat{\tau} \hat{\tau}^{N-1} \frac{d^2\hat{\sigma}_{ab}(\hat{\tau},\cos\theta)}{d\hat{\tau}\, d\cos\theta} \ . \tag{4.8}$$

The threshold limit ($\hat{\tau} \to 1$) now corresponds to $N \to \infty$ in moment space.

Threshold resummation results in exponentiation of the soft gluon corrections in moment space. Unlike color singlet cases like the Drell-Yan process, in heavy-flavor production soft gluons emitted at large angles interfere with the color structure of the underlying Born process. One must then take into account all color structures and sum over them. The details of this procedure were worked out for scattering at fixed angles in [20, 21, 83]. For a given partonic channel ($ab = q\bar{q},\ gg$), the resumed perturbative cross section is given by [1]

$$\begin{aligned} \hat{\sigma}_{ab}^{(\mathrm{res})}(N,\theta) \ &= \ C_{ab}(\theta)\, \Delta_a(N) \Delta_b(N) \\ &\quad \times \mathrm{Tr}\left\{ H_{ab}^{(0)}(\theta)\ [\mathcal{S}_{ab}(N,\theta)]^\dagger\ S_{ab}^{(0)}\, \mathcal{S}_{ab}(N,\theta) \right\} \ , \end{aligned} \tag{4.9}$$

where we have suppressed for simplicity the dependence of the various functions on the pair mass $M_{t\bar{t}}$, but have kept dependence on the scattering angle θ wherever it occurs. Even before defining the various factors in the resummed cross section, we may note that it naturally gives rise to a charge asymmetry. In Eq. (4.9), all dependence on the c.m. scattering angle θ resides in the color trace part and in the coefficients C_{ab}. Therefore, these generate the charge-asymmetric part of the cross section near threshold:

$$\begin{aligned} \Delta\hat{\sigma}_{q\bar{q}}^{(\mathrm{res})}(N,\theta) \ &= \ (\Delta_q(N))^2 \Big[C_{q\bar{q}}(\theta)\, \mathrm{Tr}\left\{ H_{ab}^{(0)}(\theta)\ [\mathcal{S}_{ab}(N,\theta)]^\dagger\ S_{ab}^{(0)}\, \mathcal{S}_{ab}(N,\theta) \right\} \\ &\quad - C_{q\bar{q}}(-\theta)\, \mathrm{Tr}\left\{ H_{ab}^{(0)}(\theta)\ [\mathcal{S}_{ab}(N,-\theta)]^\dagger\ S_{ab}^{(0)}\, \mathcal{S}_{ab}(N,-\theta) \right\} \Big] \ . \end{aligned} \tag{4.10}$$

[1] See, in particular, Eq. (50) of Ref. [21].

It is the ratio of Eq. (4.10) and its charge-averaged counterpart that defines the asymmetry. We anticipate that, when expanding the resummed expression to next-to-leading order, leading logarithms cancel and the C_2 term in Eq. (4.4) is reproduced.

Now let us review the elements of the resummed cross sections. The trace in Eq. (4.9) is taken in a space of color exchange operators [20, 21]. At lowest order, $H_{ab}^{(0)}$ and $S_{ab}^{(0)}$ are the hard-scattering and the zeroth-order soft functions, respectively. The factors $\mathcal{S}_{ab}$ are also matrices in color space and depend on the basis of color tensors used to describe color exchange. Employing the s-channel singlet-octet basis of [20], one has for the $q\bar{q}$ subprocess, which we are mostly interested in here,

$$\begin{aligned} H_{q\bar{q}}^{(0)} &= \alpha_s^2 \begin{pmatrix} 0 & 0 \\ 0 & 2\left(\frac{t^2+u^2}{s^2}+2\frac{m_t^2}{s}\right)/C_A^2 \end{pmatrix} , \\ S_{q\bar{q}}^{(0)} &= \begin{pmatrix} C_A^2 & 0 \\ 0 & (C_A^2-1)/4 \end{pmatrix} , \end{aligned} \tag{4.11}$$

where $t \equiv (p_t - p_a)^2 - m_t^2 = -s(1-\beta\cos\theta)/2$, $u \equiv (p_{\bar{t}} - p_a)^2 - m_t^2 = -s(1+\beta\cos\theta)/2$, with p_a the momentum of initial parton a, $\beta = \sqrt{1-4m_t^2/s}$, and $C_A = 3$. The corresponding expressions for the soft anomalous dimension matrices of the gg-initiated subprocess may be found in [20]. Note that the Born cross sections are recovered by computing $\mathrm{Tr}\{H_{ab}^{(0)} S_{ab}^{(0)}\}$ and that $H_{ab}^{(0)}$ is symmetric under interchange of t and u and hence charge symmetric.

Each of the functions $\Delta_{a,b}(N)$ and $\mathcal{S}_{ab}(N,\theta)$ is an exponential. $\Delta_a(N)$ represents the effects of soft-gluon radiation collinear to initial parton a and in the $\overline{\mathrm{MS}}$ scheme is given by

$$\ln \Delta_a(N) = \int_0^1 \frac{z^{N-1}-1}{1-z} \int_{\mu^2}^{(1-z)^2 M_{t\bar{t}}^2} \frac{dq^2}{q^2} A_a(\alpha_s(q^2)) , \tag{4.12}$$

and similarly for $\Delta_b(N)$. The function A_a is a perturbative series in α_s,

$$A_a(\alpha_s) = \frac{\alpha_s}{\pi} A_a^{(1)} + \left(\frac{\alpha_s}{\pi}\right)^2 A_a^{(2)} + \dots , \tag{4.13}$$

with [84]:

$$A_a^{(1)} = C_a , \quad A_a^{(2)} = \frac{1}{2} C_a \left[C_A \left(\frac{67}{18} - \frac{\pi^2}{6} \right) - \frac{5}{9} N_f \right] , \tag{4.14}$$

where N_f is the number of flavors, and

$$C_q = C_F = (N_c^2 - 1)/2N_c = 4/3\,, \quad C_g = C_A = N_c = 3\,. \tag{4.15}$$

The factors $\Delta_{a,b}(N)$ generate leading threshold enhancements, due to soft-collinear radiation, as the same overall factors in both the charge symmetric and antisymmetric cross sections.

The large-angle soft gluon exponentials $\mathcal{S}_{ab}(N,\theta)$ are dependent on the process and mix the color structure. One has

$$\mathcal{S}_{ab}\left(N,\theta\right) \;=\; \mathcal{P}\exp\left[\frac{1}{2}\int_{M_{t\bar{t}}^2}^{M_{t\bar{t}}^2/N^2}\frac{dq^2}{q^2}\Gamma_{ab}^{S}\left(\alpha_s(q^2),\theta\right)\right]\,, \tag{4.16}$$

where $\mathcal{P}$ denotes path ordering and where Γ_{ab}^{S} are soft anomalous dimensions, which are also matrices in a given color basis. They are perturbative; for the resummation at NLL one only needs the first-order term and path ordering becomes irrelevant. For the $q\bar{q}$ subprocess, the first-order anomalous dimension matrix can be represented as

$$\Gamma_{q\bar{q}}^{S,(1)} = \frac{\alpha_s}{\pi}\begin{pmatrix}\Gamma_{11}^{q\bar{q}} & \Gamma_{12}^{q\bar{q}}\\ \Gamma_{21}^{q\bar{q}} & \Gamma_{22}^{q\bar{q}}\end{pmatrix}\,, \tag{4.17}$$

with matrix elements [20][2]

$$\begin{aligned}
\Gamma_{11}^{q\bar{q}} &= -C_F\left[L_\beta + 1 + i\pi\right],\\
\Gamma_{21}^{q\bar{q}} &= 2\ln\left(\frac{t}{u}\right)\,,\\
\Gamma_{12}^{q\bar{q}} &= \frac{C_F}{C_A}\ln\left(\frac{t}{u}\right)\,,\\
\Gamma_{22}^{q\bar{q}} &= C_F\left[4\ln\left(\frac{t}{u}\right) - L_\beta - 1 - i\pi\right]\\
&\quad + \frac{C_A}{2}\left[-3\ln\left(\frac{t}{u}\right) - \ln\left(\frac{m_t^2 s}{tu}\right) + L_\beta + 1 + i\pi\right]\,,
\end{aligned} \tag{4.18}$$

where

$$L_\beta = \frac{1-2m_t^2/s}{\beta}\left(\ln\frac{1-\beta}{1+\beta} + i\pi\right)\,. \tag{4.19}$$

Finally, the coefficients $C_{ab}(\theta)$ contain N-independent hard contributions aris-

[2]Note that for our definition of the charge asymmetry we need to interchange t and u in the results of [20].

ing from one-loop virtual corrections. They are perturbative as well, and have the expansion

$$C_{ab}(\theta) = 1 + \frac{\alpha_s}{\pi} C_{ab}^{(1)}(\theta) + \mathcal{O}(\alpha_s^2) \; . \tag{4.20}$$

The coefficients $C_{ab}^{(1)}$ may be obtained by comparison of the resummed formula to the full NLO calculation. We note that they contain the Coulomb corrections which diverge as $1/\beta$ at $s \sim 4m_t^2$. As indicated, the $C_{ab}^{(1)}$ depend on the scattering angle θ, and in fact for the $q\bar{q}$ subprocess they also contain a charge-asymmetric part. The full coefficients have been derived in Ref. [81] and are given by very lengthy expressions. Starting from slightly corrected versions [3] of the expressions given in [81], we have been able to verify that the charge-asymmetric part of the resulting coefficient for the $q\bar{q}$ process reproduces the corresponding result given in [74].

We now give explicit formulas for the expansions of the resummed exponents to NLL accuracy following the general approach of [87]. The functions $\Delta_{a,b}(N)$ become

$$\begin{aligned} \ln \Delta_N^a(\alpha_s(\mu^2), M_{t\bar{t}}^2/\mu^2) \; &= \; \ln \bar{N} \; h_a^{(1)}(\lambda) + h_a^{(2)}(\lambda, M_{t\bar{t}}^2/\mu^2) \\ &\quad + \mathcal{O}\left(\alpha_s(\alpha_s \ln N)^k\right) \; . \end{aligned} \tag{4.21}$$

Here $\lambda = \beta_0 \alpha_s(\mu^2) \ln \bar{N}$ with $\bar{N} = N e^{\gamma_E}$, where γ_E is the Euler constant. The functions $h^{(1,2)}$ are given by

$$h_a^{(1)}(\lambda) = \frac{A_a^{(1)}}{2\pi\beta_0\lambda} \left[2\lambda + (1-2\lambda)\ln(1-2\lambda)\right] \; , \tag{4.22}$$

$$\begin{aligned} h_a^{(2)}(\lambda, M_{t\bar{t}}^2/\mu^2) = &- \frac{A_a^{(2)}}{2\pi^2\beta_0^2} \left[2\lambda + \ln(1-2\lambda)\right] + \frac{A_a^{(1)}}{2\pi\beta_0} \ln(1-2\lambda) \ln \frac{M_{t\bar{t}}^2}{\mu^2} \\ &+ \frac{A_a^{(1)}\beta_1}{2\pi\beta_0^3} \left[2\lambda + \ln(1-2\lambda) + \frac{1}{2}\ln^2(1-2\lambda)\right] \; , \end{aligned} \tag{4.23}$$

where $\beta_0 = \left(11C_A - 2N_f\right)/12\pi$, and

$$\beta_1 = \frac{1}{24\pi^2}\left(17C_A^2 - 5C_A N_f - 3C_F N_f\right) \quad . \tag{4.24}$$

The function $h_a^{(1)}$ above contains all LL terms in the perturbative series, while $h_a^{(2)}$ is of NLL only. For a complete NLL resummation one also needs the

[3] Specifically, we use Eq. (A.19) of Ref. [85] in the second and third integral in (A.20) of Ref. [86] and in Eqs. (A.9) and (A.11) of the first paper of Ref. [81].

expansion of the integral in Eq. (4.16), given by,

$$\ln \mathcal{S}_{ab}\left(N,\theta\right) \;=\; \frac{\ln(1-2\lambda)}{2\pi b_0}\,\Gamma^{S,(1)}_{q\bar{q}}(\theta)\,. \tag{4.25}$$

While the full structure of the resummed expressions is rather long and complicated, a major simplification occurs when one expands it for small β and ignores the coefficient C_{ab}. One finds in this case

$$\begin{aligned}\hat{\sigma}^{(\mathrm{res})}_{q\bar{q}}(N,\theta) \;&=\; \hat{\sigma}^{(\mathrm{Born})}_{q\bar{q}}(\theta)\;\left(\Delta_q(N)\right)^2\left\{1+\frac{\beta\cos\theta(8C_F-3C_A)\ln(1-2\lambda)}{\pi b_0}\right\}\\ &\quad\times \mathrm{e}^{-\frac{C_A}{2\pi b_0}\ln(1-2\lambda)}\,.\end{aligned} \tag{4.26}$$

Here, the factor $8C_F-3C_A$ is the typical color factor associated with the QCD charge asymmetry [74]. One can see how the single threshold logarithm arises at the first order in α_s in the charge-asymmetric part. The charge-asymmetric piece is suppressed by the factor β, but enhanced by the term $\ln(1-2\lambda)$. All factors outside the curly brackets are common to the charge-asymmetric and the charge-summed parts and are expected to largely cancel in the charge asymmetry at hadron level. We note that in the limit $\beta \to 0$ our formulas above reproduce the moment-space expressions for the resummed total heavy-flavor cross section derived in [80].

In our discussion below, we use the full formula (4.10) when calculating the charge asymmetry. Since the matrices involved for the $q\bar{q}$ subprocess are two-dimensional, it is straightforward to perform the required exponentiations and other manipulations, explicitly employing a diagonal color basis for these 2×2 matrices [20]. For the (charge-symmetric) gg subprocess, the matrices are three-dimensional, and this procedure becomes more complicated. We found it simpler here to do the matrix manipulations numerically, calculating in particular the matrix exponentials by iterating the exponential series to the tenth order. We emphasize again that the gg process is charge-symmetric. Thus, it only contributes to the denominator of the charge asymmetry, diluting the asymmetry somewhat, because the effects of threshold resummation can be larger for gluons than for quarks.

4.4 Phenomenological results

We will now investigate the numerical size of the QCD charge asymmetry for top quark production at the Tevatron, making use of the resummation formulas presented above. In order to do this, we first need to specify the inverse Mellin

transform. This requires a prescription for dealing with the singularity in the perturbative strong coupling constant in the resummed exponent. We will use the *Minimal Prescription* developed in Ref. [87], which relies on use of the NLL expanded forms Eqs. (4.21)-(4.23), and on choosing a Mellin contour in complex-N space that lies to the *left* of the poles at $\lambda = 1/2$ in the Mellin integrand:

$$\frac{d^2\sigma}{dM_{t\bar{t}}^2\, d\cos\theta} = \int_{C_{MP}-i\infty}^{C_{MP}+i\infty} \frac{dN}{2\pi i}\, \tau^{-N} \sigma^{(\mathrm{res})}(N)\ , \tag{4.27}$$

where $b_0\alpha_s(\mu^2)\ln C_{MP} < 1/2$, but all other poles in the integrand are as usual to the left of the contour. The result defined by the minimal prescription has the property that its perturbative expansion is an asymptotic series that has no factorial divergence and therefore no "built-in" power-like ambiguities. Power corrections may then be added, as phenomenologically required.

For our calculations we use the CTEQ6M parton distributions [88]. To obtain these in Mellin-moment space, we follow [89] and perform a simple fit to each parton distribution at each scale needed, using a functional form that allows Mellin moments to be taken analytically. We note that for the Tevatron case considered here, $t\bar{t}$ pairs are largely produced in valence-valence scattering, for which the parton distributions are rather well known. The higher-order and resummation effects will be very similar for other sets of parton distributions. We use $m_t = 170.9$ GeV [90], $\sqrt{S} = 1.96$ TeV, and our default choice for the factorization/renormalization scale is $\mu = M_{t\bar{t}}$.

The lower set of lines in Fig. 4.1 shows our results for the charge asymmetric cross section $d\Delta\sigma/dM_{t\bar{t}}$ as a function of the $t\bar{t}$ pair mass, while the upper set presents the charge-averaged one, $d\bar{\sigma}/dM_{t\bar{t}}$. We consider here the cross sections integrated over $0 \le \cos\theta \le 1$. In both cases, we show by the *dotted lines* the lowest-order result, which is $\mathcal{O}(\alpha_s^2)$ in the charge-averaged case, and $\mathcal{O}(\alpha_s^3)$ in the asymmetric part. In the former case, this result is just based on the usual Born cross processes, $q\bar{q} \to t\bar{t}$ and $gg \to t\bar{t}$. For the charge asymmetric part, we make use of the expressions given in the Appendix of [74]. This includes the small contribution by the quark-gluon flavor excitation process $qg \to t\bar{t}q$. Next in Fig. 4.1 we show the first-order expansion of the resummed cross sections (*dashed lines*), which are approximations to the full NLO result. In case of the charge-asymmetric piece, which only starts at NLO, we can check the quality of this approximation by comparing the dotted and dashed lines. One can see that the two results agree very well in this case, implying that the threshold corrections addressed by resummation dominate. [4]

[4] In principle, one may carry out the same check for the charge-symmetric cross section

For the charge-asymmetric part, we also show (*dashed-dotted lines*) the second-order expansion of the resummed cross section, which is of $\mathcal{O}(\alpha_s^4)$, because this contains the first non-trivial QCD correction in this case. The solid lines finally show the full NLL-resummed result. One can see that resummation has a very significant impact on the predicted cross sections, in particular for the charge-asymmetric part at high $M_{t\bar{t}}$. Note that for the resummed curve for this part we have performed a matching to the full $\mathcal{O}(\alpha_s^3)$ result of [74] by correcting it by the difference between the dotted and dashed lines. In this way, the $\mathcal{O}(\alpha_s^3)$ is taken into account in full, and the soft-gluon contributions beyond NLO are resummed to NLL.

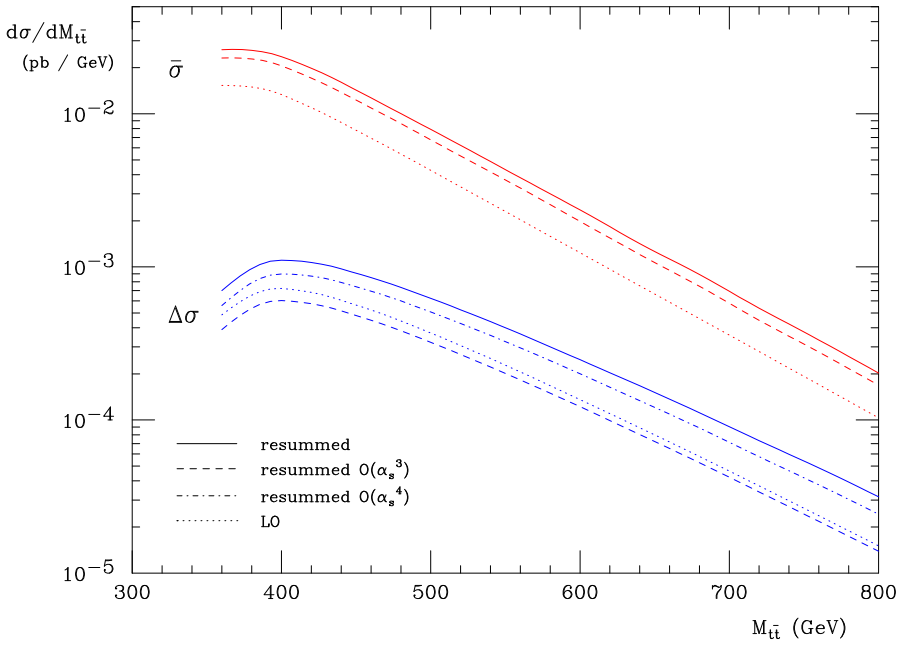

Figure 4.1: Charge asymmetric and charge averaged cross sections $d\Delta\sigma/dM_{t\bar{t}}$ and $d\bar{\sigma}/dM_{t\bar{t}}$ as functions of the $t\bar{t}$ pair mass, integrated over $0 \leq \cos\theta \leq 1$. Dotted lines are LO, dashed lines include the first-order corrections generated by resummation, and solid lines show the full resummmed result. For the charge-asymmetric part, we also show the second-order expansion of the resummed cross section, which is of $\mathcal{O}(\alpha_s^4)$, because this contains the first non-trivial QCD correction in this case.

In Fig. 4.2 we analyze the scale dependence of the results, for both the

at fixed $M_{t\bar{t}}$ and θ by comparing to the full NLO calculations of [71, 72]. Such a study is unlikely to change our results here qualitatively, and would go beyond the scope of this work.

charge asymmetric and averaged parts. The dash-dotted lines correspond to a variation of $M_{t\bar{t}}/2 \leq \mu \leq 2M_{t\bar{t}}$, with the central lines (dotted) the ones for $\mu = M_{t\bar{t}}$ already shown in Fig. 4.1. The higher results are obtained for the lower choice of scale. The dashed and solid lines display the same for the resummed cross sections. One can see a very significant reduction of scale dependence, in particular for the charge averaged cross section. This improvement in scale dependence due to threshold resummation is in line with similar findings in the literature for other cross sections [80–82, 91, 92]. We note that the fact that $t\bar{t}$ production at the Tevatron proceeds primarily through $q\bar{q}$ valence-valence annihilation helps here, since only the flavor-diagonal non-singlet evolution matters, which is part of the resummation formula [80, 91].

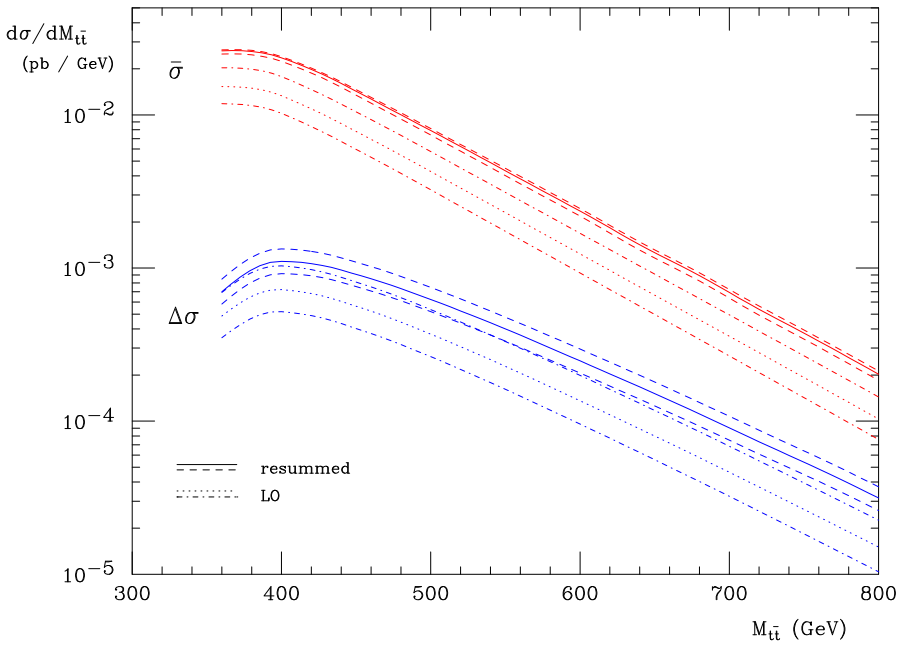

Figure 4.2: Scale dependence of the LO (dotted and dash-dotted) and NLL resummed (solid and dashed) cross sections, for a scale variation $M_{t\bar{t}}/2 \leq \mu \leq 2M_{t\bar{t}}$.

Figure 4.3 shows the charge asymmetries $A_c = d\Delta\sigma/d\Delta\bar{\sigma}$ corresponding to the various curves in Fig. 4.1, as functions of the pair mass. As before, the dotted line shows the LO result, the solid represents the full resummed result, and the dashed one is the expansion of the resummed cross section. For the latter we expand the cross section to $\mathcal{O}(\alpha_s^4)$ in the numerator of the asymmetry, and to $\mathcal{O}(\alpha_s^3)$ in the denominator, thus taking into account the first non-trivial QCD correction in both cases. Had we expanded both numerator and denominator to $\mathcal{O}(\alpha_s^3)$, the numerator would be at LO, and an artificially

small asymmetry would result. One can see that the various results are rather close, implying that the net effect of resummation on the charge asymmetry is not large. This is related to the fact that the double-logarithmic factors $\propto (\Delta_q(N))^2$ in the resummation formula are the same for the charge asymmetric and averaged parts. Towards lower $M_{t\bar{t}}$, where the speed of the produced top quark becomes small, all asymmetries become small on account of Eq. (4.26). At large pair masses, the additional single threshold logarithm enhances the asymmetry.

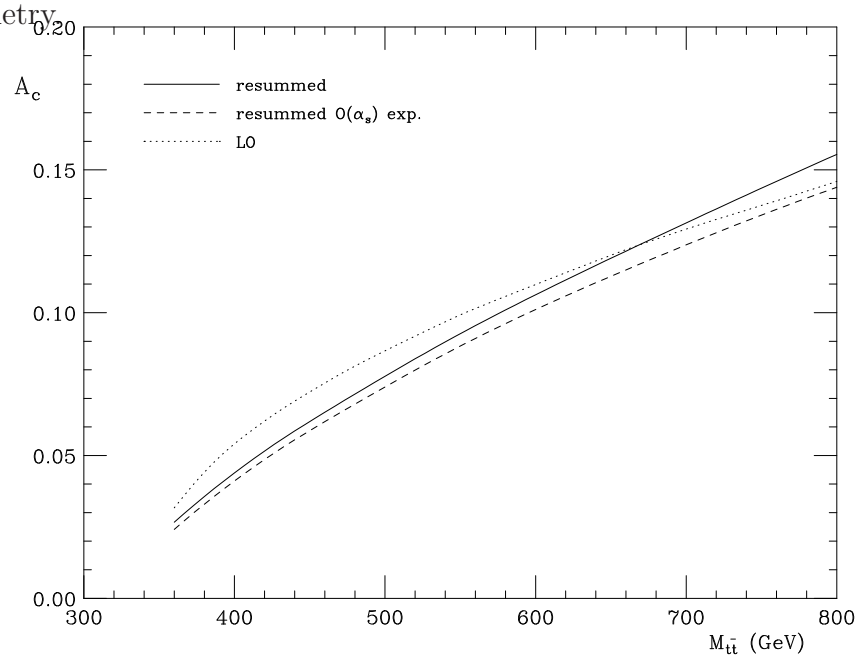

Figure 4.3: Charge asymmetry corresponding to the curves in Fig. 4.1.

In Fig. 4.4 we consider the asymmetry as a function of $\cos\theta$, with $M_{t\bar{t}}$ integrated over the allowed kinematic region. Again the net effect of resummation on the asymmetry is relatively moderate. This leads generally to a smaller asymmetry, because lower pair masses, at which the asymmetry decreases when going from the LO to the resummed case (see Fig. 4.3), dominate the cross section. As Figs. 4.3 and 4.4 show, the resummed asymmetries grow substantially with both pair mass, when integrated over rapidity, and with the relative rapidity of the pair. Interestingly, these results are consistent with the explicit NLO results presented in Refs. [75, 76], which indicate a decrease in the charge asymmetry, and even a reversal of its sign, for top pair plus jet cross sections. In such final states, the NLO virtual corrections to inclusive pair production are absent, and it is the latter corrections that determine the sign of the asymmetry itself.

We finally turn to the total charge asymmetry $A_c^{\text{tot.}}$, integrated over $M_{t\bar{t}}$

and $0 \leq \cos\theta \leq 1$. At LO, using the scale $\mu = M_{t\bar{t}}/2$, we find $A_c^{\text{tot.}} = 6.7\%$. Resummation results in only a small change, $A_c^{\text{tot.}} = 6.6\%$. We note that when varying the scale over the range $m_t \leq \mu \leq M_{t\bar{t}}$, the LO charge-symmetric part of the cross section varies by about $\pm 20\%$ around its central value, which is improved by resummation to a variation of about $\pm 3\%$. The scale dependence of the asymmetric part of the cross section improves from $\pm 28\%$ to $\pm 13\%$. The resummed asymmetry shows a variation over this range of scales of about $\pm 12\%$. Thus our results for the higher-order corrections to $A_c^{\text{tot.}}$ are well consistent with the estimate of a $\sim 30\%$ uncertainty made in Ref. [67].

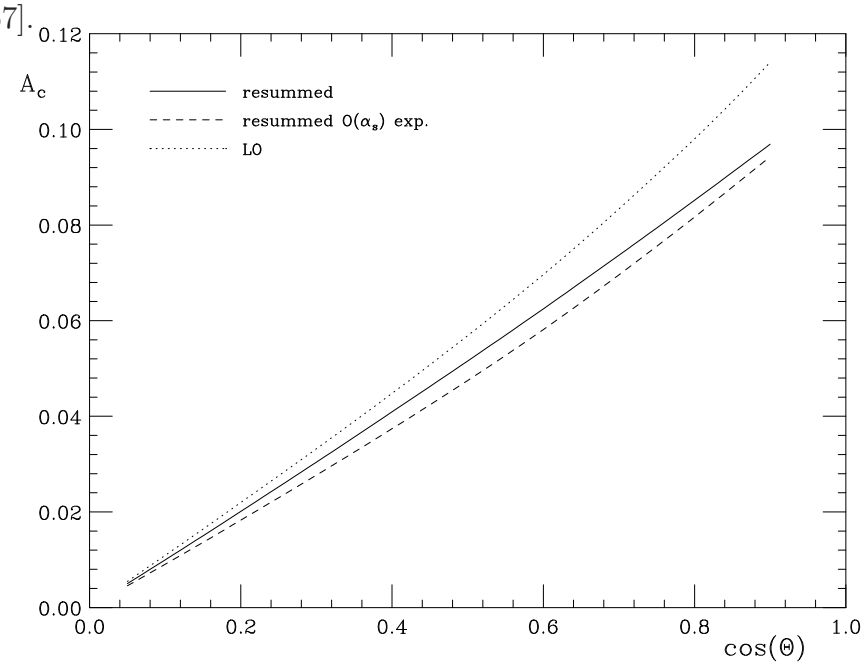

Figure 4.4: Same as Fig. 4.3, but as a function of $\cos\theta$, integrated over the $t\bar{t}$ pair mass.

4.5 Conclusions and Outlook

We have presented a study of the next-to-leading logarithmic QCD threshold resummation effects on the charge asymmetry in inclusive $t\bar{t}$ production at the Tevatron. We have found that the asymmetry is stable with respect to the higher-order corrections generated by threshold resummation. We have also found that resummation significantly decreases the dependence of the results on the factorization and renormalization scales, thus making the Standard Model prediction for the asymmetry more reliable.

It will be interesting to extend these studies to the case of $t\bar{t}$ jet production, for which sizable negative NLO corrections have been found [76]. Also, there will be interesting applications at the LHC in situations near partonic threshold, i.e., when the $t\bar{t}$ pair mass becomes of the order of 1 TeV or larger. Because the initial pp state is symmetric, one needs to apply additional cuts (for example, on the $t\bar{t}$ pair rapidity) here in order to generate a non-vanishing charge asymmetry [74].

Now we take a step back from resummation and look how logarithmic corrections arise in the study jet production and how such jet distributions are distinct from top jets distributions.

Chapter 5

Top Jets at the LHC

The Large Hadron Collider (LHC) is expected to uncover some of the most interesting mysteries of nature. We expect to probe the underlying principles of electroweak symmetry breaking (EWSB) and what stabilizes the weak scale against radiative corrections from unknown microscopic dynamics. Due to its large mass, the top quark induces the most severe contributions to the Higgs quadratic divergence. Furthermore, in almost every known natural model of EWSB, the top sector plays a crucial role in breaking the EW symmetry. Thus, the top sector might hold a key to a new physics (NP) discovery. Many interesting models of EWSB predict new particles with mass $\sim$ TeV scale. In several known examples, the new particles decay into highly boosted top quark pairs ($pp \to X \to t\bar{t}$), or other decay chains containing a single top quark ($pp \to X \to t\,Y$). In addition, the Standard Model (SM) predicts that the LHC will produce more than 10^5 top quarks with $p_T \geq 1\,\text{TeV}$, significantly enhancing our ability to study high p_T tops and resolving beyond the SM dynamics.

Top quarks decay dominantly into hadronic final states ($t \to bW \to bq\bar{q}$) with a branching ratio $\sim 2/3$, providing potentially enhanced statistics. In the present work, we focus on highly boosted top quarks (decaying through the hadronic channel), and on the dominant QCD jet background. We refer to a top quark that decays hadronically as a *hadronic top*. For moderately boosted top quarks ($p_T \sim 500$ GeV), conventional top quark reconstruction methods, which exploit the decay chain topology, remain adequately efficient (see *e.g.* [93]). As the top quark p_T approaches 1 TeV, the situation significantly changes [94–97].[1] The average separation of the top quark decay products approaches the limits of reliable jet reconstruction (cone size $R \sim 0.4$), and starts to encroach upon the detector resolution ($R \sim 0.1$). As a result, the

[1]For earlier works in the case of boosted EW bosons see also [148].

efficiency of conventional reconstruction methods drops quickly. The performance of b-tagging and light jet rejection is expected to drop substantially in this kinematic regime. At present, there is very little published data on b-tagging at $p_T \sim 1\,\text{TeV}$ [99]. We perform our analysis without accounting for the possible benefits of b-jet identification.[2]

We turn our focus away from this family of "conventional" reconstruction methods. We examine the situation where the decay products of at least one top quark are reconstructed as a single jet, or *top-jet*. In semileptonic $t\bar{t}$ events, for example, the leptonic top may still be reconstructed via semi-conventional reconstruction methods, giving up on lepton isolation cuts [94], see also [96, 100]. These methods call for further extensive study due to expected reducible backgrounds and uncertainties related to the ability to measure the collimated semi-leptonic top mass (dileptonic $t\bar{t}$ events are also analyzed in [101]). Hadronic top, on the other hand, will give rise to a top-jet. There will still be some small, but non-negligible, number of $t\bar{t}$ events where one of the top quarks reconstructs as a top-jet, but the other top quark can be reconstructed via conventional methods (or semi-conventional methods where one of the tops is manifested as a two-jet object). In this paper, we focus on the top-jet itself as a means of identifying $t\bar{t}$ events. The main reasoning behind that is as follows:

(i) We find that for $p_T > 1\,\text{TeV}$ the majority of hadronic-tops are manifested as top-jets, even for cone size as small as $R = 0.4$. Thus, it is clear that our tools will be applicable for a wide range of top momenta.

(ii) The distributions and shapes of both background and signal can be understood via first principle calculations as shown in this study and in Ref. [25]. It may allow for a cleaner analysis, in the sense that a more direct contact between actual data (expected to arrive soon) and the microscopical theory can be made.

Apart from substructure, to leading order, top jets provide four pieces of information, namely its energy, two angles and mass (just as any QCD jet, ignoring the possibility of b-tagging). Without a mass cut, the QCD jet background swamps the hadronic top signal by orders of magnitude. The most basic tagging method after giving up conventional methods is to use the jet mass as a discriminator between the QCD background and the hadronic top signal; the high-p_T top-jet mass distribution should peak around the top mass while the QCD jet mass distribution peaks near zero. However, using a

[2]The possibility of b-tagging jets, when the top quark reconstructs to 2 (or more) jets, one of which has a mass $\sim m_W$ and the sum of the two jets has a mass $\sim m_t$, is outside the main focus of this paper.

jet mass as a discriminator is more complicated for several reasons. Due to radiation, QCD jets acquire a large tail in the mass distribution. The cross section for acquiring large jet mass, for example near the top mass, increases substantially with p_T and cone size. Top-jets also broaden due to radiation, hardening their jet mass distribution.[3] Furthermore, a finite jet reconstruction cone size will not always capture all the daughters of the top quark decay chain, thus softening its mass distribution. The net effect is a smearing of the expected naive, broadened, Breit-Wigner distribution for the top jet mass distribution. Detector effects further smear the distribution, making the above idealized description unrealistic.

Nevertheless, jet mass cuts should retain some rejection power against the QCD background [103–105]. Our study addresses this issue in both quantitative and qualitative manner, by considering the experimental and theoretical aspects of the analysis. On the theoretical front, based on a factorization approach, we derive a simple approximation for the shape of the QCD jet mass spectrum. We demonstrate that there is good agreement between our simple analytic predictions and Monte Carlo (MC) results. We are able to compute from first principle various features related to a jet mass cut. We evaluate its significance in the form of a semi-analytical expression for the rejection power and show that it is independent of pseudorapidity. We provide a quantitative study of the distribution of the signal and background, via MadGraph/MadEvent [106–108](MG/ME) and Sherpa [109]. We consider the detector resolution by using transfer functions [110], smearing jets according to a profile obtained from full Geant4 Atlas simulation. Transfer functions provide a versatile mechanism to explore such effects as shifts in jet energy scale (JES), etc.

We apply the results of our studies to analyze boosted SM top quark pair production, an important discovery channel for NP [94–96, 100, 111–115]. To put results into perspective, we use both $25\,\mathrm{fb}^{-1}$ and $100\,\mathrm{fb}^{-1}$ of integrated luminosity as reference luminosities. At this time, these correspond to many years of data taking. We show that using single- and double-tagging methods with our jet functions (defined below) to analyze jet mass distributions, we can significantly separate the Standard Model $t\bar{t}$ signal from the QCD background. Our theoretical QCD jet mass distributions can efficiently characterize the background via sideband analyses. With 25 fb^{-1} of data, our approach allows us to resolve 1 TeV top-jets from the QCD background, and about 1.5 TeV top-jets with 100 fb^{-1}, if we exploit the kinematics of the so-called "away" side of the event, without relying on b-tagging. The essence of the away side mass cut is that it preferentially keeps the $t\bar{t}$ signal over the

[3]For a detailed recent study see [102] and references therein.

background. We analyze the mass distribution in more detailed manner, as simple counting methods are inadequate. As described above, the $t\bar{t}$ signal is expected to exhibit pronounced structure near the top quark mass. In order to resolve this "peak" against the QCD background, we need to understand the shape of both the $t\bar{t}$ signal and the QCD background. To characterize the background we perform a sideband analysis to reduce contamination by the signal. Our theory-driven ansatz for the QCD background is an admixture of quark- and gluon-jet functions, the coefficients of which we analyze by fitting in the sidebands (outside the top mass window). We interpolate the results of the fit into the top mass window ($140\,\mathrm{GeV} \leq m_J \leq 210\,\mathrm{GeV}$). Armed with *shapes* for the signal and background, we fit them into the data to obtain the normalization constants. These normalization constants are the magnitude of the signal and background. The errors associated with the normalization provides a measure of the significance of the measurement.

To further improve the significance we consider jet shapes [25], which resolve substructure of energy flow inside cone jets. In a companion paper [25], we explore the possibility that, requiring a large jet mass, perturbative predictions for jet shapes differ between jets that originate from the decay of heavy particles, and those which result from the showering of light quarks and gluons. With such additional handles, we might have a chance to distinguish boosted $t\bar{t}$ signal from the QCD background even at a smaller integrated luminosities.[4] We discuss jet substructure later in the text.

We turn our attention to the use of b-jets as spin analyzers for the top quarks. For highly boosted top quarks, chirality is approximately equal to helicity and is conserved to a good approximation. Information about the top chirality is encoded in the angular distribution of the decay products [94, 119, 120]. Naively, one would argue that for hadronic tops this information is inaccessible due to collimation and the absence of leptons which are known to be good spin analysers [119, 120]. We explore the possibility of using p_T of the b-quark for measuring the top quark polarization, which is important for exploring NP. For this, we explore the case when at least one of the boosted top quark can be resolved into more than two jets. We also consider the possibility of using p_T of the lepton for measuring the top quark polarization for semi-leptonically decaying tops.

This work has two main focal points, namely QCD jet mass distributions and hadronic $t\bar{t}$ signal, and is structured as follows. In the next section, we discuss the MC generation and detector simulation. In section 5.2 we focus on highly boosted QCD jets. The jet mass distribution is examined numerically,

[4]There are other approaches dealing with a similar situation in a different perspective in recent literature [97, 116, 153, 154].

via MC methods, and analytically, via jet functions. The salient points of the jet functions are introduced, leaving detailed derivations for the Appendix. Section 5.3 discusses the top-jet signal. In section 5.4, we compare high p_T hadronic $t\bar{t}$ events with QCD jets. In section 5.5 we discuss jet shapes [25], which can be used as additional discriminants against the background. Section 5.6 discusses the hadronic top quark polarization by using the transverse momentum of the bottom quark. We conclude in section 5.7.

5.1 Event Simulation

5.1.1 Monte Carlo Generation

The Sherpa [109] and MG/ME (version 4) [106, 108] MC generators were used to produce $t\bar{t}$ and QCD jet events, with parameters appropriate to the LHC. To effect partonic level cuts during the generation of QCD jets
($p_T\,(\geq 1$ parton$) \geq 800$ GeV), we used customized code provided by the Sherpa authors applicable to Sherpa V1.1.0. For technical reasons, $t\bar{t}$ events were generated using Sherpa version 1.0.9, whereas QCD jet events were generated with Sherpa version 1.1.0. MG/ME interfaces to Pythia V6.4 (for parton shower and fragmentation) [121]. For jet reconstruction, we used SISCone V1.3 [122] for both Sherpa and MG/ME. Cross sections are calculated to leading order. Jets are defined via the cone algorithm [123] with $R = 0.4$ and $R = 0.7$, referred to as C4 and C7, respectively. Jets have $p_T > 50\,\text{GeV}$ and $|\eta| \leq 2$. At the hard scatter level, final state partons are required to have $p_T \geq 20\,\text{GeV}$. For MG/ME events, the final state partons have $|\eta| \leq 4.5$.

We do not account for pile-up effects nor characterize the underlying event. Efficiencies for triggering and reconstruction of jets at these energies are very close to unity; the corrections are negligible and are not considered. The strong coupling constant was allowed to run. Throughout the analysis, we used Sherpa V1.0.9 with CTEQ6M parton distribution functions (PDF) [124]. Comparisons to MG/ME were made whenever appropriate, and also occasionally to Pythia (version 8.1) [125] for $2 \to 2$ process without matching. In such cases, the distinct curves are marked accordingly. The events used in the analysis were inclusive, i.e. $pp \to t\bar{t}(j)$ and $pp \to jj(j)$, with matching (see [126] for a detailed discussion): modified MLM [127] for MG/ME and CKKW [128] for Sherpa.

5.1.2 Cross Sections

In table 5.1 we present cross sections for producing final state (hadronic level) jets with $p_T \geq 1\,\text{TeV}$ for the different MC simulations. There are large uncertainties in the cross sections, due to differences between the MLM and CKKW matching, between MC generators, and between PDFs. It is outside the scope of this paper to explore the reasons behind these differences.[5] We estimate a 100% systematic uncertainty associated with the $t\bar{t}$ cross section, and a 20% systematic uncertainty in the QCD jet cross section.

Process	Generator	PDF	Matching	Cross Section
$pp \to t\bar{t}(j)$	SHERPA 1.0.9	CTEQ6M	CKKW	135 fb
$pp \to t\bar{t}(j)$	SHERPA 1.1.2	CTEQ6M	CKKW	149 fb
$pp \to t\bar{t}(j)$	MG/ME 4	CTEQ6M	MLM	68 fb
$pp \to t\bar{t}(j)$	MG/ME 4	CTEQ6L	MLM	56 fb
$pp \to t\bar{t}$	Pythia 6.4	CTEQ6L	-	157 fb
$pp \to t\bar{t}$	Pythia 8.1	CTEQ6M	-	174 fb
$pp \to jj(j)$	SHERPA 1.1.0	CTEQ6M	CKKW	10.2 pb
$pp \to jj(j)$	MG/ME 4	CTEQ6L	MLM	8.54 pb
$pp \to jj(j)$	MG/ME 4	CTEQ6M	MLM	9.93 pb
$pp \to jj$	Pythia 6.4	CTEQ6L	-	13.7 pb
$pp \to jj$	Pythia 8.1	CTEQ6M	-	13.3 pb

Table 5.1: Cross sections for producing final state $R = 0.4$ leading cone jets with $p_T \geq 1\,\text{TeV}$ and $|\eta| \leq 2$. Generation level cuts were imposed as follows. Final state partons from the hard scatter were required to have $p_T \geq 20\,\text{GeV}$. For MG/ME, final state partons have $|\eta| \leq 4.5$. Processes with a trailing (j) suffix indicate that $2 \to 2$ and $2 \to 3$ processes are represented.

5.1.3 Modelling Detector Effects

A transfer function, trained with full ATLAS detector simulation on high p_T jet and high p_T $t\bar{t}$ samples, was used to map particle level jets (Atlas truth jet reconstruction) onto a full simulation model [110]. Transfer functions work by feeding back the differences between the target collection (Full Simulation) and the source collection (Truth Jets). The differences and efficiencies are

[5] Sherpa data was generated with an invariant $t\bar{t}$ mass cut greater than 500 GeV; MadGraph was generated with a p_T cut > 700 GeV. The initial-state radiation (ISR) contributions to the cross sections do not significantly affect our analysis, as such jets populate the low mass spectrum.

stored as distributions, in the form of histograms, and binned in p_T and η. We refer to the collection of the smearing distributions as a *transfer function*. It is important to note that transfer functions are applicable on events with similar jet multiplicity and topology. We applied the transfer function (trained on Atlas truth jets) to SISCone truth jets, which preserve the salient characteristics of the Atlas truth jets. We used the transfer function to effect p_T and mass smearing, but not reconstruction efficiency. At the energies considered in this paper, reconstruction efficiency is very close to unity. In summary, the results of the transfer function should be viewed simply as realistic detector smearing.

In this paper, a jet is transferred as follows. The transverse momentum and mass of truth-level jets are smeared according to the appropriate distribution. For the purposes of modeling the effects of the JES, the means of the p_T distributions are shifted accordingly, without cross correlation to the mass smearing. This is a subtle point. Depending on the reconstruction mechanism, reported jet masses may depend proportionally on the JES; a JES shift results in a jet mass shift. In our study of the effects of the JES, we do not make a correlation between the p_T and mass distributions. This effect is much smaller, and such precision is not warranted in these studies.

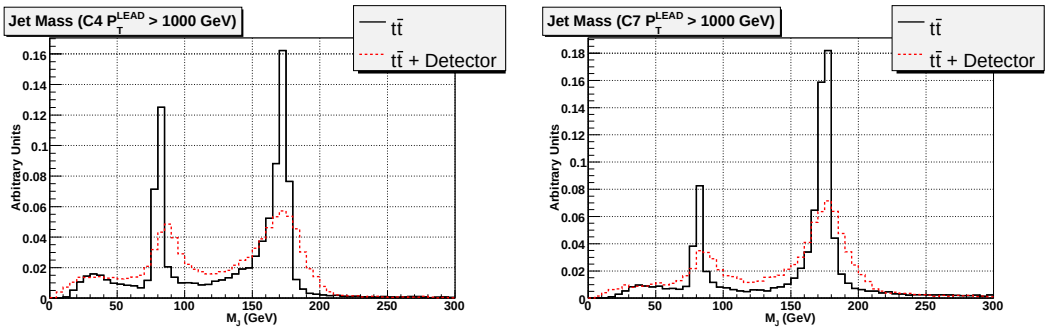

Figure 5.1: We compare the mass distribution of the leading jet $\left({p_T}^{lead} \geq 1000\,\mathrm{GeV}\right)$ for the $t\bar{t}$ signal with (the red dotted curve) and without (the black solid curve) leading detector effects. The plot on the left corresponds to C4 jets; the plot on the right corresponds to C7 jets.

In Fig. 5.1, we compare the $t\bar{t}$ jet mass distributions for C4 and C7 jets, with and without detector smearing, for ${p_T}^{lead} \geq 1000\,\mathrm{GeV}$. We see, as expected, that due to the finite cone size even the top jet mass distribution is far from the naive Breit-Wigner shape. In cases where the outgoing b quark is outside the cone, we expect that the top jet mass to be peaked around the W mass. In cases where one of the quarks from the W decay is outside the cone we expect a smooth distribution with a typical invariant mass of roughly $m_t/\sqrt{2}$,

etc. These effects are present even at the truth level, without detector effects. The black curve shows a smooth distribution with a spurious peak around the W mass. The red curve demonstrates how the detector effects further smear the top jet mass distribution.

5.2 QCD Jet Background

If jet mass methods are to be viable, we must be able to characterize the dominant QCD jet background [129]. One of the primary points in this work is that we are able to understand the QCD jet background *analytically* as well as through MC simulations. In this section, we present the summary of our analytic calculations of the QCD jet mass distribution based on the factorization formalism [155**?**], which is presented in the Appendix. We compare our theoretical prediction with simulated MC data. Note that the final states, which induce the jet masses, simulated by MC event generators are much more complicated (due to radiation, showering etc.) than our simple two body final states. Yet, as we shall see, we can consistently describe the simulated MC data.

5.2.1 Analytic Prediction

We are interested in looking at the following processes:

$$H_a(p_a) + H_b(p_b) \to J_1(m^2_{J_1}, p_{1,T}, R) + X$$

$$H_a(p_a) + H_b(p_b) \to J_1(m^2_{J_1}, p_{1,T}, R) + J_2(m^2_{J_2}, p_{2,T}, R) + X$$

where, H_i are the initial hadrons, p_i being the corresponding momenta, and the final states include jets in the direction of the outgoing partons of the underlying process, with a fixed jet mass, m_{J_i}, "cone size" $R^2 = \Delta\eta^2 + \Delta\phi^2$ and tranverse momenta, $p_{i,T}$.

We begin with the factorized hadronic cross section for single inclusive jet processes,

$$\frac{d\sigma_{H_A H_B \to J_1 X}(R)}{dp_T dm_J d\eta} = \sum_{abc} \int dx_a\, dx_b\, \phi_a(x_a)\, \phi_b(x_b) \frac{d\hat{\sigma}_{ab\to cX}}{dp_T dm_J d\eta}(x_a, x_b, p_T, \eta, m_J, R)\,, \tag{5.1}$$

which in the limit of small R, we can further factorize into (see Appendix B),

$$\begin{aligned}\frac{d\sigma_{H_A H_B \to J_1 X}(R)}{dp_T dm_J d\eta} &= \sum_{abc} \int dx_a\, dx_b\, \phi_a(x_a)\, \phi_b(x_b) H_{ab\to cX}(x_a, x_b, p_T, \eta, R) \\ &\quad \times J_1^c(m_J, p_T, R). \end{aligned} \tag{5.2}$$

The factorization and renormalization scales are chosen to be p_T, ϕ_i is the PDF for the initial hadrons, $H_{ab\to cX}$ denotes the perturbative cross section, and J^c denotes jet functions, whose matrix elements are defined in Appendix C (see *e. g.* [131] for recent reviews and references therein). Furthermore the J^cs are, by definition, normalized as

$$\int dm_J\, J^c = 1\,. \tag{5.3}$$

We have used the fact that the jet functions do not depend on η in the leading expansion (see Appendix C). Therefore, we can write Eq. (5.2) for the hadronic cross section as

$$\frac{d\sigma(R)}{dp_T dm_J} = \sum_c J^c(m_J, p_T, R)\, \frac{d\hat{\sigma}^c(R)}{dp_T}\,, \tag{5.4}$$

where c represents the flavour of the jet, and where

$$\frac{d\hat{\sigma}^c(R)}{dp_T} = \sum_{ab} \int dx_a\, dx_b\, \phi_a\, \phi_b \int d\eta \int dm_J\, \frac{d\hat{\sigma}_{ab\to cX}(R)}{dp_T dm_J d\eta}\,. \tag{5.5}$$

We employ the jet functions given in the Appendix by Eqs. (C.14) and (C.16), for fixed jet mass and R at the next-to-leading order (NLO) with running coupling effects. As we will see below, these results are consistent with the MC data for sufficiently large ($m_J \geq \mathcal{O}(100\,\text{GeV})$) jet masses.

At the lower end of the jet mass spectrum, where $m_J \ll p_T R$, the jet mass distribution is dominated by higher order corrections and non-perturbative physics [131], which are beyond the scope of our work, as our interest lies in the region of high jet mass. We note this causes complications when trying to predict the moments of the mass distributions, such as the mean and RMS, unless we introduce a lower cutoff on the mass.

In the Appendix, we provide the full NLO[2] result for the jet function in term of θ_S, the angle of the softer particle with respect to the jet axis. These exact results can be approximated by the eikonal approximation introduced

[2]Note that what we mean by NLO is "lowest nontrivial order".

in Appendix B as

$$J^{(eik),c}(m_J, p_T, R) = \alpha_s(p_T)\frac{4\,C_c}{\pi m_J}\log\left(\frac{1}{z}\tan\left(\frac{R}{2}\right)\sqrt{4-z^2}\right) \quad (5.6)$$
$$\simeq \alpha_s(p_T)\frac{4\,C_c}{\pi m_J}\log\left(\frac{R\,p_T}{m_J}\right),$$

where $\alpha_s(p_T)$ is the strong coupling constant at the appropriate scale, $z = \frac{m_J}{p_T}$, c represents the flavour of the parton which initiated the jet and C_c equals $C_F = 4/3$ for quarks, and $C_A = 3$ for gluons. These expressions agree with the full NLO jet functions to the level of about 1% and 10% for quark and gluon initiated jets in the region of the top mass window, respectively (checked for $R = 0.4$ and 0.7 and $p_T \gtrsim 1\,\text{TeV}$).

We can interpret the jet function as a probability density functions for a jet with a given p_T to acquire a mass between m_J and $m_J + \delta m_J$. Our rather simple treatment is valid for the higher end of the jet mass spectrum (above $m_J \sim \mathcal{O}(100\,\text{GeV})$), where NLO perturbative calculation captures the dominant physics. In Fig. 5.2 we show the gluon jet mass distribution from (C.16) with running (red, dashed), and fixed (blue, dotted) coupling, along with the eikonal jet function (green, dashed-dotted) with fixed coupling. The fixed scales are chosen to be p_T. For reference we also superimpose in the Fig. a $1/m_J$ curve which has the same dimension as that of our jet functions and is roughly of the form of the soft function (*cf* Appendix B). It is remarkable that our theory curves are significantly different from simple $1/m_J$ curve whose normalization is chosen such that this curve overlaps with our theory curves around the top mass. This indicates that logarithmic factor is very important in our theory prediction. Note that at lower masses the running is much harder than the fixed cases since the configurations associated with this mass region have lower k_T (the radiated gluon momenta), leading to a larger α_s. Also, the eikonal approximation is equivalent to a no recoil approximation, thus resulting overall in a harder process than the result in Eq. (C.16) at fixed scales.

For the purpose of comparing the mass distributions obtained from jet functions and the MC simulations, Eq. (5.5) can be matched to $(d\sigma^c(R)/dp_T)_{\text{MC}}$ obtained from MC, leading to the following relation,

$$\frac{d\sigma^c_{pred}(R)}{dp_T dm_J} = J^c\left(m_J, p_T, R\right)\left(\frac{d\sigma^c\left(R\right)}{dp_T}\right)_{\text{MC}}, \quad (5.7)$$

for the prediction of quark and gluon jet mass distribution based on perturbative calculated jet functions, Eqs. (C.14) and (C.16). Note, however, that

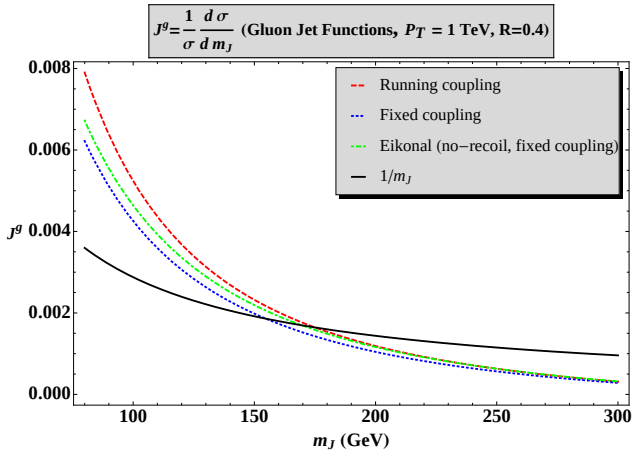

Figure 5.2: Various theoretical gluon-jet mass distributions, along with a $1/m_J$ curve, are plotted for $p_T = 1\,\text{TeV}$ and $R = 0.4$. Plotted are the jet mass distribution from (C.16) with running (red, dashed), and fixed (blue, dotted) coupling, along with the eikonal jet function (green, dashed-dotted) with fixed coupling. For the jet functions with no running the scales were chosen be p_T.

this would require us to split the MC output in terms of the parton flavours c, which for realistic simulation leads to ambiguities especially when matching is used. Therefore, for our analysis, instead, we use the analytic result to suggest bounds for the "data" distribution from the MC. There is, however, no a posteriori way to determine the flavour which initiated the jet (as with real data). Thus, we write

$$\left.\frac{d\sigma_{pred}(R)}{dp_T dm_J}\right|_{upper\ bound} = J^g\left(m_J, p_T, R\right) \sum_c \left(\frac{d\sigma^c\left(R\right)}{dp_T}\right)_{\text{MC}}, \tag{5.8}$$

$$\left.\frac{d\sigma_{pred}(R)}{dp_T dm_J}\right|_{lower\ bound} = J^q\left(m_J, p_T, R\right) \sum_c \left(\frac{d\sigma^c\left(R\right)}{dp_T}\right)_{\text{MC}}, \tag{5.9}$$

exploiting the fact that $J^g > J^q$ in the region of high jet mass, as can be seen in Eq. (5.7).

5.2.2 Jet Function, Theory vs. MC Data

In this section, we compare a set of theory-based bounds for the jet mass distribution to the mass distribution obtained via MC event generators. This part contains one of our main results, where we demonstrate that our theoretical

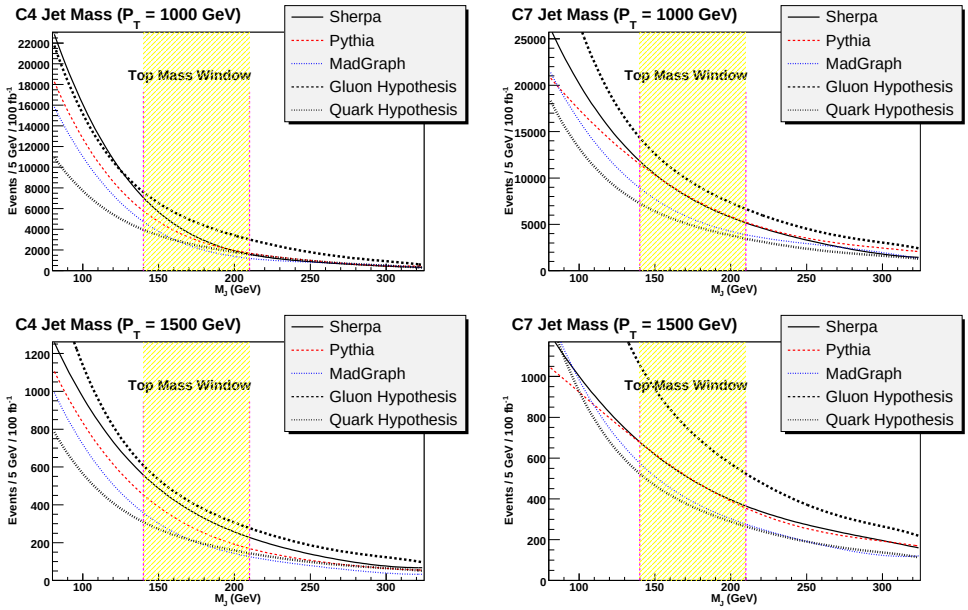

Figure 5.3: The jet mass distributions for Sherpa, Pythia and MG/ME are plotted for different p_T and jet cone sizes. The quark and gluon mass distributions from the jet functions are overlaid, using Eqs. (5.8) and (5.9). The upper left plot corresponds to $950\,\text{GeV} \leq p_T \leq 1050\,\text{GeV}$ and $R = 0.4$. The upper right plot corresponds to $950\,\text{GeV} \leq p_T \leq 1050\,\text{GeV}$ and $R = 0.7$. The lower left plot corresponds to $1450\,\text{GeV} \leq p_T \leq 1550\,\text{GeV}$ and $R = 0.4$. The lower right plot corresponds to $1450\,\text{GeV} \leq p_T \leq 1550\,\text{GeV}$ and $R = 0.7$.

predictions are in agreement with the MC data. In Fig. 5.3, we compare the quark and gluon jet mass distributions from Eqs. (5.8) and (5.9) to the distributions from different MC generators (MG/ME, Sherpa and Pythia). We perform this comparison at fixed p_T, since we are interested in the relative shapes of these distributions around the top mass window. Note that above $m_J \sim \mathcal{O}(100\,\text{GeV})$, the *shapes* of three MC distributions are very similar. Sherpa and MG/ME distributions interpolate between the quark jet function (lower bound) and the gluon jet function (upper bound) as expected. For the purposes of comparing shapes, Pythia and MG/ME are rescaled so that their total cross sections agree with Sherpa. This cross section scaling does not affect the predictive quality of the theory curves, since it affects both sides of Eqs. (5.8) and (5.9). The scaling allows us to present the results from the different event generators on a single plot. Note, as mentioned before, that for $m_J \ll p_T R$, higher order corrections will contribute, pushing the distribution down, with a Sudakov-like suppression, which can be seen in the lower mass region for $p_T = 1.5$ TeV and $R = 0.7$.

In a typical experimental setup, a lower cut over p_T will be assumed and the distributions will be integrated above that p_T^{min} cut. Thus we can integrate over the appropriate region on Eq. (5.7), which leads to the analog of Eqs. (5.8) and (5.9) for the p_T-integrated jet mass cross section,

$$\frac{d\sigma^c_{pred}(R)}{dm_J} = \int_{p_T^{min}}^{\infty} dp_T\, J^c\left(m_J, p_T, R\right) \sum_{c'} \left(\frac{d\sigma^{c'}(R)}{dp_T}\right)_{\text{MC}}, \qquad (5.10)$$

where J^c is defined as before. The MC differential cross section is obtained by summing over the contributions from both quark and gluon jets. Therefore, the cross section's shape is characterized by an admixture of quark and gluon jets and should interpolate between the two curves, $c = q$ and g. In Fig. 5.4, we compare leading jet mass distribution for events where the leading jet has $p_T \geq 1\,\text{TeV}$ obtained from Sherpa. The quark and gluon curves, obtained from Eq. (5.10), with use of the jet functions in Eqs. (C.14) and (C.16), correspond to the cases where the lead jets are all quark or gluons jets, respectively.

As before, we find the bounds for the total cross section

$$\sigma(R)_{upper\ bound} = \int_{p_T^{min}}^{\infty} dp_T \sum_c \left(\frac{d\sigma^c\left(R\right)}{d\,p_T}\right)_{\text{MC}} \int_{140\,GeV}^{210\,GeV} J^g\left(m_J, p_T, R\right) dm_J, \qquad (5.11)$$

$$\sigma(R)_{lower\ bound} = \int_{p_T^{min}}^{\infty} dp_T \sum_c \left(\frac{d\sigma^c\left(R\right)}{d\,p_T}\right)_{\text{MC}} \int_{140\,GeV}^{210\,GeV} J^q\left(m_J, p_T, R\right) dm_J, \qquad (5.12)$$

In table 5.2, we refer to the gluon and quark jets from the results in Eqs. (5.11)

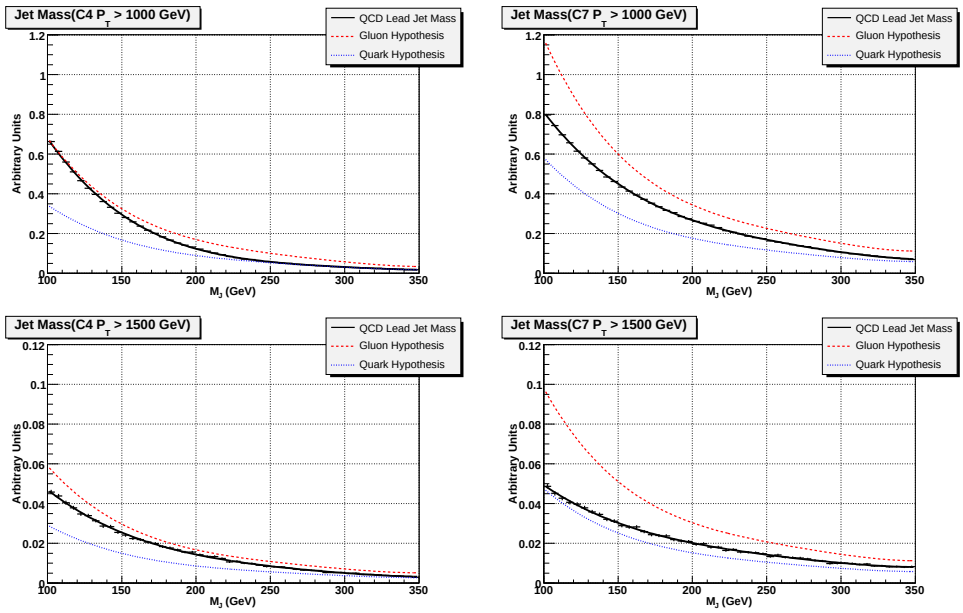

Figure 5.4: Comparison between the theoretical jet mass distributions and MC leading jet mass distribution from Sherpa. The minimum p_T and cone size are indicated on the plots. A gluon (quark) hypothesis is the prediction made if the entire contribution were from gluon (quark) jets (cf Eq. (5.10)).

and (5.12), respectively. The numbers in the table were calculated as follows. From a MC sample corresponding to 100 fb^{-1} of data, we extracted the number of events with C4 lead jet $p_T \geq 1000(1500)\,\text{GeV}$ and $140\,\text{GeV} < m_J < 210\,\text{GeV}$, the top mass window. We repeated this exercise for C7 jets. The *data* column contains these results.

${p_T}^{lead}$ cut	Cone Size	Data	Quark hypothesis	Gluon hypothesis
1000 GeV	C4	113749	70701	135682
1000 GeV	C7	197981	131955	260045
1500 GeV	C4	10985	6513	12785
1500 GeV	C7	13993	11164	22469

Table 5.2: Comparison of Sherpa MC data to predictions of pure-quark and pure-gluon hypothesis, for the number of events with leading jet with mass between 140 GeV and 210 GeV. The data is compared to the bounds given in Eqs. (5.11) and (5.12). The statistics reflect 100 fb^{-1} of integrated luminosity.

Fractional Fake Rate

With the theoretical machinery discussed in the previous section, we are able to make a prediction of the rate at which QCD jets will fake the mass signature of top-jets. We define the fractional fake rate as the fraction of jets with $140\,\text{GeV} \leq m_J \leq 210\,\text{GeV}$, for given p_T and R. We estimate the upper and lower bounds of the fractional fake rate as

$$\int_{140\ GeV}^{210\ GeV} dm_J\, J^q(m_J, p_T, R) \leq \text{ Fractional fake rate } \leq \int_{140\ GeV}^{210\ GeV} dm_J\, J^g(m_J, p_T, R)\,. \tag{5.13}$$

In Fig. 5.5, we plot the fractional fake rate as a function of jet transverse momentum. To predict the number of fakes in our sample, we fold the differential cross section for QCD jet production (Fig. 5.6) with the fractional fake rate (Fig. 5.5). Again we expect a Sudakov-like suppression when $m_J \ll p_T R$, thus flatting the theoretical fractional fake rate as p_T increases. This can be seen more predominately for $R = 0.7$ in Fig. 5.5.

Pseudorapidity Independence of the Jet Mass Distribution

In general, we expect that NP signals will have a pseudorapidity dependence. Therefore, the study of pseudorapidity dependence may provide a tool for NP

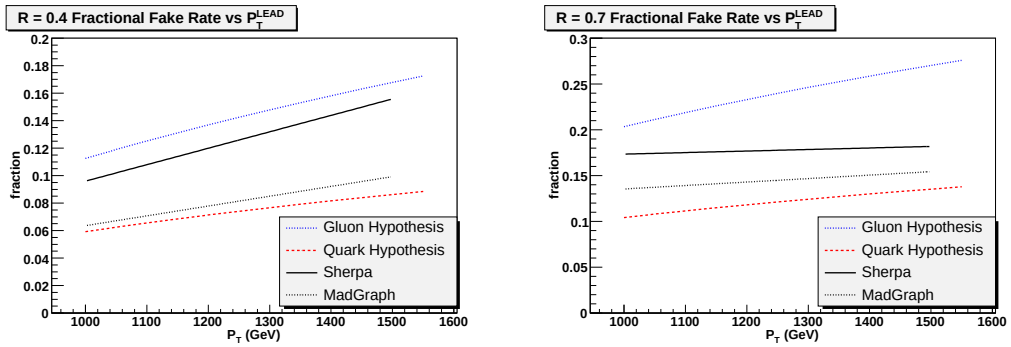

Figure 5.5: The fraction of jets which acquire $140\,\text{GeV} \leq m_J \leq 210\,\text{GeV}$ as a function of the transverse momentum of the leading jet. Quark- and gluon-hypothesis curves yield the prediction for the fractional fake rate, if all jets were either quark- or gluon-jets, respectively. The plot on the left corresponds to C4 jets; the plot on the right corresponds to C7 jets (cf Eq. (5.13)).

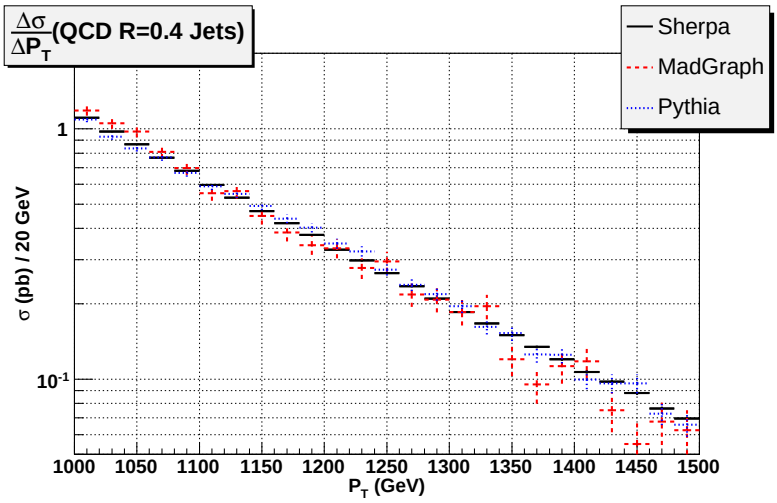

Figure 5.6: The differential cross section for QCD ($R = 0.4$) jet production with respect to the p_T of the leading jet. Sherpa, MG/ME and Pythia are represented.

searches (for an interesting discussion see [132]). In Fig. 5.7, we plot the jet mass distributions for central and outer jets. We observe consistency with the approximation that the distributions are to leading order, independent of pseudorapidity.

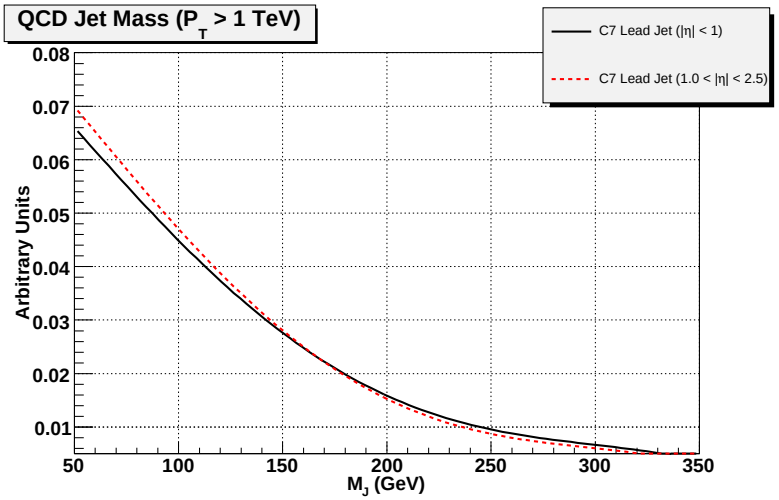

Figure 5.7: The $R = 0.7$ jet mass distribution for central jets ($|\eta| < 1$) and for jets with $1 \leq |\eta| \leq 2.5$. Jets have $p_T \geq 1\,\text{TeV}$. This plot is produced with the Sherpa MC.

5.3 High p_T Hadronic Top Quarks

In this section, we discuss the collimation of the top quark decay products at the partonic level. In Fig. 5.8, we plot the rate of collimation[3] as a function of the top p_T (for a related discussion and analysis see [96, 97, 100]). We define collimation rate as the fraction of top quarks which reconstruct to a jet having $140\,\text{GeV} \leq m_J \leq 210\,\text{GeV}$.

To examine the efficiency of the jet mass methods, it is instructive to look at mass distributions for the signal and background. We examine the distributions for events where the leading jet p_T exceeds 1000 GeV and 1500 GeV with

[3]Due to ISR, collimation rates for final state jets differ from naive expectation values based on partonic-level analysis. As discussed in the text, our analysis methods include a group mass criteria, a simple but powerful discriminant, against ISR jets. Therefore, our results are robust against such effects. Residual contributions are absorbed as a source of background. Refinement of methods to further reduce ISR contributions are analysis-dependent, and outside the scope of this work.

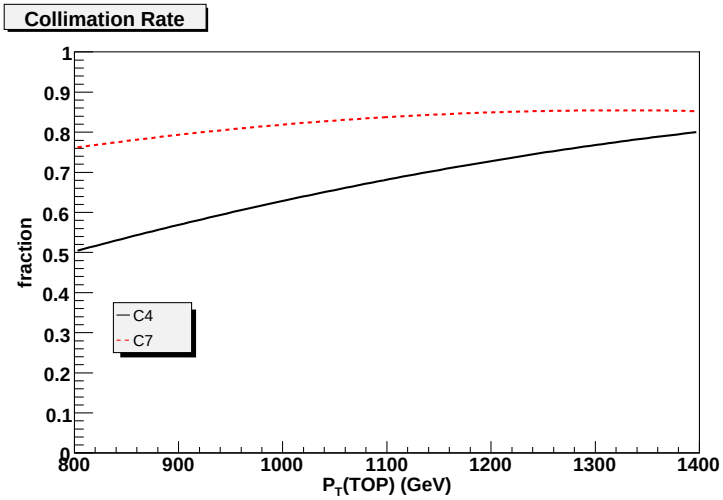

Figure 5.8: The collimation rate for top quarks as a function of their transverse momentum, for C4 (black solid curve) and C7 (red dashed curve) jets. Collimation rate is defined as the fraction of events with top quarks giving rise to a final state jet with $140\,\text{GeV} \leq m_J \leq 210\,\text{GeV}$.

C4 and C7 jets. In Fig. 5.1, we plot the jet mass distribution for the $t\bar{t}$ signal for ${p_T}^{lead} \geq 1000\,\text{GeV}$. The efficiency of C7 jets for capturing the hadronic top is greater than that for C4 jets. For C4 jets, we still observe pronounced structure around the W-mass (M_W), which diminishes for C7 jets. We also note that the peak for the C7 jets moves closer to the top mass, indicating a higher efficiency for capturing the hadronic top. We expect that detector effects will further smear the signal. Fig. 5.1 also shows the mass distributions including leading detector effects (using transfer functions).

We note that the analysis has an inherent tension with regard to choosing the cone size for the jet. The reconstruction cone should be sufficiently wide to capture all the daughter products of the hadronic top. On the other hand, we need to keep the cone appropriately small to keep out the QCD jet background and other soft contamination [97].

We describe the gross features of the top mass distribution, without providing a detailed analytic expression for the top jet. At lowest order in QCD and before decay, the top jet mass distribution is simply $\delta(m_J - m_t)$. This distribution is modified both by QCD radiation and electroweak decay.

We can describe QCD radiation by a top jet function, $J^t_{QCD}(m_{QCD}, R, p_T)$, similar to the functions for massless QCD jets, where J^t_{QCD} is a function of $m_{QCD} \equiv m_t + \delta m_{QCD}$. Gluon radiation from top quarks makes the top jet mass

harder, giving the additional mass contribution, δm_{QCD}. Using factorization, this process can be calculated by methods similar to the one discussed in the Appendix, fixing the mass of the parton to m_t and treating it as stable. For our purposes, the resulting broadening is subdominant for a top mass window of ± 35 GeV. [4] The QCD radiation that determines the shape of J^t_{QCD} at a resolution of $\sim$ 10 GeV is characterized by a very short time scale of $\mathcal{O}(1/(10\,\mathrm{GeV}))$ in the top rest frame.

Although long compared to $1/m_t$, the rest frame time scale on which the distribution in m_{QCD} is determined is substantially shorter than the electroweak time scale, which is set by $\Gamma_t = \mathcal{O}(1.5)$ GeV, the top quark width in the Standard Model [133, 134]. The difference in time scales implies a quantum mechanical incoherence between the QCD radiation, described by $J^t_{QCD}(m_{QCD}, R, p_T)$, and the top quark weak decay. These two physical processes are thus expected to factorize up to corrections that are determined by the ratio of Γ_t to the size of the top quark window, and we shall assume that this is the case. Using this assumption, we describe the effect of electroweak decay by an overall factor $\mathcal{F}^t_{EW}(\delta m_{EW}, m_{QCD}/(p_T R))$. This function is responsible for producing the two peaks corresponding to the top quark and W boson in the signal mass distribution Fig. 5.1, by acting on the underlying QCD top jet function J^t_{QCD}, which has a single peak at m_t.

We see from Fig. 5.1 that the effect of the decay on the jet mass, δm_{EW}, can be sizable. The actual distribution depends on cone size that we use to identify the jet. The main effect here is a softening of the jet mass, because the jet cone may not capture all the particles from the top quark decay chain. This kinematic effect depends solely on $m_{QCD}/(p_T R)$. As we see from Fig. 5.1, it reduces the mass of the top jet and produces a peak near the W mass. Since the top jet mass softening is a kinematic process, it should be well described by generators based on phase space.

In summary, we can schematically express the top jet mass squared as a sum of three contributions. [5]

$$m_J \sim m_t + \delta m_{QCD} + \delta m_{EW}\,, \tag{5.14}$$

where the jet mass function related to Fig. 5.1 can be schematically written

[4] However, a treatment of the broadening is crucial if one aim to improve the top mass measurement at the LHC. At the moment this has been studied only for the ILC [102].

[5] The choice of mass, as opposed to, say, mass squared for the convolution variable is a matter of convention, to keep our notation in J^t_{QCD} consistent with the light quark jet functions. Convolutions in jet mass squared, which are familiar from event shape distributions, can be obtained simply by changing variables and as necessary changing the normalizations of the functions J^t_{QCD} and $\mathcal{F}_{EW}$.

as a convolution of three different sources

$$J^t(m_J, R, p_T) \sim \int d(\delta m_{EW}) dm_{QCD}\, \delta(m_J - m_{QCD} - \delta m_{EW}) \times J^t_{QCD}(m_{QCD}, R, p_T)\, \mathcal{F}_{EW}(\delta m_{EW}, m_{QCD}/(p_T R)) \quad (5.15)$$

The top mass is large, so we are not concerned about uncertainties in the lower jet mass spectrum. In fact, the same considerations that lead to this result allow us to conclude that existing MC tools should well describe this part of our studies. We will thus rely on event generators rather than Eq. (5.15) in our numerical studies below.

5.4 $t\bar{t}$ Jets vs. QCD Jets at the LHC

In this section, we combine the results of the previous discussions, and apply them to analyze energetic SM $t\bar{t}$ events vis-a-vis QCD jet production at the LHC. The main purpose of this section is to understand how well we can discriminate our signal from the overwhelming QCD background. We illustrate an example analysis using the jet functions, and evaluate their performance on MC data. Unfortunately, it is very difficult to outline a one-size-fits-all analysis. Therefore, we perform a broad-strokes analysis that contains sufficient detail to provide general guidance. We do not attempt to invoke advanced, but analysis-specific, procedures that could provide further refinement. It is also important to bear in mind that the final evaluation of the jet functions, as precision analysis tools, can really only be done on real data. The primary reason is that we expect the jet functions to describe physics data. The MC distributions are, at this point, an approximation to what we believe will be LHC data. A precision analysis will show the strains between the jet function-based shape predictions and the effective distribution that MC uses to generate its mass distribution.

We examine two cases in detail, both at truth-level (no detector effects) and accounting for detector effects. The first case, *single tagging*, consists of "top-tagging" (requiring $140\,\text{GeV} \leq m_J \leq 210\,\text{GeV}$) the leading jets satisfying a p_T cut. The second case, *double tagging*, consists of top-tagging the leading and subleading jets, with a p_T cut only on the leading jet.

5.4.1 Peak Resolution

In this analysis, one objective is to resolve the excess of events where the mass of the leading jet lies in the top mass window ($140\,\text{GeV} \leq m_J \leq 210\,\text{GeV}$). It

is important to note that we are not hunting for a peak; we already know its location. The issue is that of resolving its magnitude and estimate the probability that the background would fluctuate to yield the observed data. To estimate the significance of such a measurement, we perform a rudimentary analysis for resolving peaks. We emphasize that it is misleading to estimate the significance as $S/\sqrt{B}$, where the signal and background are separate MC samples. These numbers represent an unrealizable scenario, and tend to be optimistic. In real data, there is no way to separate the signal from background with certainty. Furthermore, at the present time, we cannot trust MC to provide the precise shape of QCD jet mass distributions. Therefore, we derive our approximations to the background *shape* directly from the "data", via sideband analysis (outside the top mass window). We use our previous knowledge of the shape of the background in the sideband region, to minimize the number of degree of freedoms involved in the sideband fit. We will discuss this further in the next section.

After approximating the shape of the background in the sideband region, we interpolate the shape of the background into the top mass window. The primary challenges are that our background is large and also has large uncertainties, which induce large uncertainties in the signal. We discuss this in more detail at the conclusion of this section. For the shape of the $t\bar{t}$ signal inside the top mass window, we use MC. In principle, the shape of the top mass distribution can be also derived semi-analytically, as discussed in section 5.3 (see also [102]). However, to leading order we expect the MC data to provide us with a reliable shape (it should capture the radiation at the leading log approximation, also the, phase space, population of the top decay products is purely kinematical). For simplicity we use the simulation data for this step in our analysis. These shapes, after normalization to unit area, are referred to as *probability density functions*. Unfortunately, the standard acronym for probability density functions conflicts with existing usage for parton distribution functions in this paper. To avoid confusion, we simply refer to them as *shapes*. We use the approximate shapes for the signal and background to perform an extended maximum likelihood fit to the sample, with jet mass distribution $F\left(m_J\right)$, thereby obtaining the background and signal normalizations. We define a jet mass distribution $F\left(m_J\right)$ as

$$F\left(m_J\right) = N_B \times b\left(m_J\right) + N_S \times s\left(m_J\right), \tag{5.16}$$

where N_B is the predicted background, and N_S is the predicted signal in the top mass window. $b\left(m_J\right)$ and $s\left(m_J\right)$ are used to denote the background and signal shapes, respectively. Both N_B and N_S are allowed to float independently.

Sideband Background Analysis

We perform a sideband analysis in order to avoid the $t\bar{t}$ signal-rich region. The basic goal is to understand the shape of the background by examining a region where there is no signal. In the sidebands, in particular the low side, the signal contaminates the background. In Fig. 5.1, we see that the $t\bar{t}$ signal does not vanish outside the top mass window. Although it is small compared to the QCD background as can be seen in Fig. 5.10, this contamination substantially impacts resolution of the peak. We attempt to purify the background in this region, by rejecting energetic jets consistent with originating from a top quark decay, i.e. - signal, as follows. For a candidate event where the leading jet passes preselection criteria, all jets within a cone $R = 1$ are (vectorially) added into a single combined jet. We call this a group jet, although this definition differs slightly from that in J. Conway, *et al.*, in [97]. If the group mass, m_G, of the combined jet falls within the top mass window, the candidate event is rejected. This discriminant tends to reject events where the decay products of the top quarks are not fully collimated, i.e. reconstructed as a single jet. We must understand any biases introduced by this discriminant. Fig. 5.9 shows the effect of the m_G cuts on the background and signal. The background shape is left relatively intact, but the signal is substantially diminished.

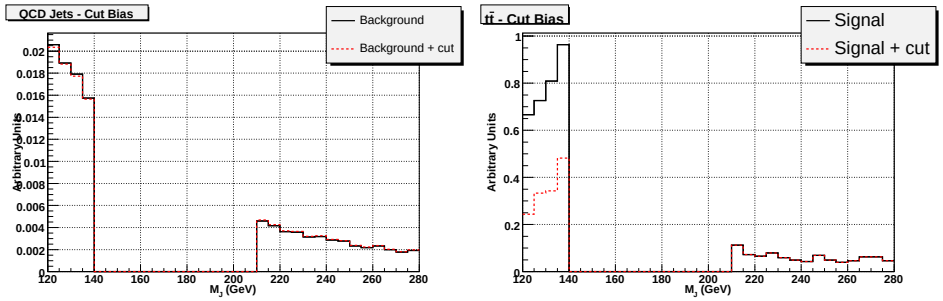

Figure 5.9: The jet mass distributions for the $t\bar{t}$ and QCD jet samples in the sidebands. The plot on the left depicts the shape of the QCD jet sample before and after making a combined jet mass cut on m_G, as described in Sec. 5.4.1. Both curves are normalized to unit area, to show the similarity of the shapes before and after the cut. The plot on the right depicts the effect of the combined jet mass cut on the $t\bar{t}$ signal. The red (dashed) curve shows the effect of the cut relative to the original jet mass distribution (black solid curve). Note: Unlike the left plot, these curves are not renormalized.

Advanced use of this m_G discriminant is outside the scope of this analysis, possibly leading to more sophisticated analyses (see *e. g.* J. Conway, *et al.*,

in [97]). We simply use it to efficiently reject signal events in the sidebands, while keeping the majority of background events.

We analyze the shape of the background in the sidebands using the jet functions derived in section 5.2. We expect real QCD jets to be an admixture of quark and gluon jets. Therefore, our Ansatz posits the admixture of quarks and gluons as a fraction. We expect small corrections (deviations from a constant admixture) to arise from different sources. For example, we do not consider events with a leading jet of fixed p_T, but rather impose a lower p_T cut. Our Ansatz for the jet mass distribution assumes the following form

$$b(m_J) \propto \beta\left(m_J\right) \times J^Q\left(m_J; p_T^{min}, R\right) + \left(1 - \beta\left(m_J\right)\right) \times J^G\left(m_J; p_T^{min}, R\right), \quad (5.17)$$

where $\beta\left(m_J\right)$ is a linear polynomial $\left(\beta_0 + \beta_1 \frac{m_J}{p_T^{min} R}\right)$. Note that with $b(m_J)$ defined above, along with Eq. (5.16), the total number of degree of freedom involved in the sideband fit is four: β_0, β_1, N_B and N_S.

Significance

After resolving the magnitude of the signal ($t\bar{t}$) peak against that of the QCD jet background, via the methods outlined in the previous sections, we now discuss how to interpret those results. Our analysis is based on *log-likelihood ratio* method.[6] A background+signal hypothesis to describe a data sample is only meaningful if a background-only hypothesis is unlikely to describe that sample. We estimate the *statistical* significance, n_σ, of the peak as

$$n_\sigma = \sqrt{2\ (\log \mathcal{L} - \log \mathcal{L}_0)}, \quad (5.18)$$

where $\mathcal{L}_0$ is the value of the maximized likelihood function obtained from fitting the data to the background shape alone (equivalent to setting N_S to zero in Eq. (5.16)), and $\mathcal{L}$ is the value of the maximized likelihood function obtained from fitting the data to the background shape and signal shape.[7] The functional form of the likelihood function is given by

$$\mathcal{L} = \prod_{k=1}^{N_{\text{BINS}}} \frac{\exp\left(-F\left(m_k\right)\right) \times \left[F\left(m_k\right)\right]^{N_k}}{N_k!}, \quad (5.19)$$

where we are fitting for the functional form of $F\left(m_J\right)$ as given by Eq. (5.16). Here, m_k and N_k refer to the value of the mass at the center, and the occupancy,

[6] An excellent discussion may be found in the The Review of Particle Physics [135].

[7] Except in pathological cases, the significance is well approximated by $\frac{S}{\Delta S}$, where S is the fitted signal, and ΔS is the error on S.

of the k-th bin, respectively.

5.4.2 Single Top-Tagging

For each of the signal ($t\bar{t}$) and background (QCD jets) samples, we preselect events with a p_T cut on the leading jet. In Fig. 5.10 we plot the jet mass distribution including detector effects for the signal and background, including the theoretical upper and lower bound for the background. We show the number of events with jet mass in the range $140\,\text{GeV} \leq m_J \leq 210\,\text{GeV}$. For reference, the number of events for the signal and background, at the truth-level, are presented in table 5.3. It is clear that the background is roughly two orders of magnitude larger than the signal. Once we add detector effects the significance of the signal is further deteriorated. We conclude that a simple counting method would not be effective here.

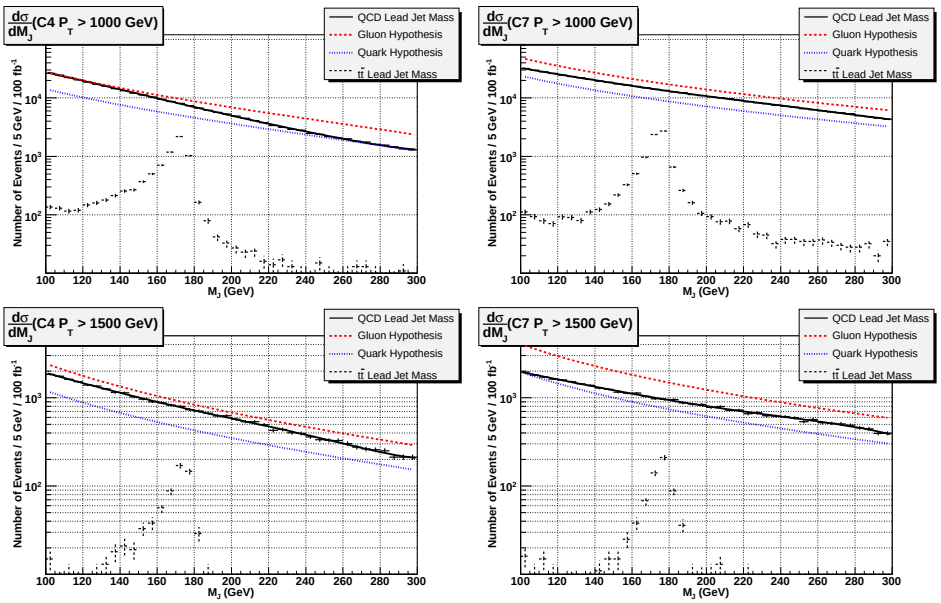

Figure 5.10: The jet mass distributions for the $t\bar{t}$ and QCD jet samples. The plots on the top row correspond to a ${p_T}^{lead} \geq 1000\,\text{GeV}$. The plots on the bottom row correspond to a ${p_T}^{lead} \geq 1500\,\text{GeV}$. The plots on the left correspond to $R = 0.4$; the plots on the right correspond to $R = 0.7$. The theoretical bounds, Eq. (5.10), are also plotted. These numbers are tabulated in table 5.3.

Detector Effects

Here, we repeat the truth-level procedure from above, accounting for the leading effects of detector resolution and ±5% jet energy scale. We also tabulate the relative change in acceptance of the signal and background, due to detector resolution and energy scale, which we define as

$$\Delta_{\text{JES}} = \frac{N_{\text{JES}} - N_{\text{TRUTH}}}{N_{\text{TRUTH}}}, \tag{5.20}$$

where N_{JES} is the number of events passing the selection criteria after detector smearing and JES effects have been applied. These results are tabulated in table 5.4, which shows how the signal and background are affected differently by smearing effects. We see that the net effects of the detector smearing plus the uncertainties in the JES lead to substantial uncertainties $\mathcal{O}(10\% - 30\%)$ in the signal and background. As anticipated, this leads to a clear failure of simple counting type analyses and calls for a different approach, which will be introduced in the following in the form of sideband analyses and jet shapes.

${p_T}^{lead}$ cut	Cone Size	$t\bar{t}$ (S)	Background (B)	S/B
1000 GeV	C4	6860	113749	0.060
1000 GeV	C7	8725	197981	0.044
1500 GeV	C4	630	10985	0.057
1500 GeV	C7	689	13993	0.049

Table 5.3: Truth-level (no detector effects) results for single-tag jet mass method, reflecting $100\,\text{fb}^{-1}$ of integrated luminosity. S and B reflect the number of jets with 140 GeV $< m_J <$ 210 GeV for the signal and background, respectively.

Results for single tagging

We now apply the analysis described in the previous sections to resolve the peak related to the top quark in the signal region, the top mass window. First we perform a sideband background analysis, to resolve the shape of the background. After applying the cuts described in Sec. 5.4.1, we fit the background to our Ansatz. Fig. 5.11 shows an example of such background fit to our Ansatz. The results of this fit described by Eq. (5.16) and below are shown in Fig. 5.12, which demonstrates how the detector affects the signal resolution.

p_T^{lead} cut	Cone	S (0% JES)	+5% JES	Δ_5	-5% JES	Δ_{-5}
1000 GeV	C4	5778	6562	-4.3%	4798	-30.1%
1000 GeV	C7	7367	8543	-2.1%	6037	-30.8%
1500 GeV	C4	741	934	48.3%	536	-14.9%
1500 GeV	C7	789	1119	62.4%	601	-12.8%
p_T^{lead} cut	Cone	B (0% JES)	+5% JES	Δ_5	-5% JES	Δ_{-5}
1000 GeV	C4	107661	122291	7.5%	90232	-20.7%
1000 GeV	C7	192710	224666	13.5%	154733	-21.8%
1500 GeV	C4	13615	18144	65.2%	10108	-8.0%
1500 GeV	C7	18712	25361	81.2%	13407	-4.2%

Table 5.4: Acceptance of signal and background for the single tag method, relative to truth-level analysis, accounting for the leading effects of detector resolution and jet energy scale (JES). The $t\bar{t}$ signal is represented in the top half; the QCD jet background is represented in the bottom half. The statistics reflect $100\,\mathrm{fb}^{-1}$ of integrated luminosity. Δ_{JES} is the relative change in background for the indicated JES, relative to truth-level analysis in table 5.3 (cf Eq. (5.20)).

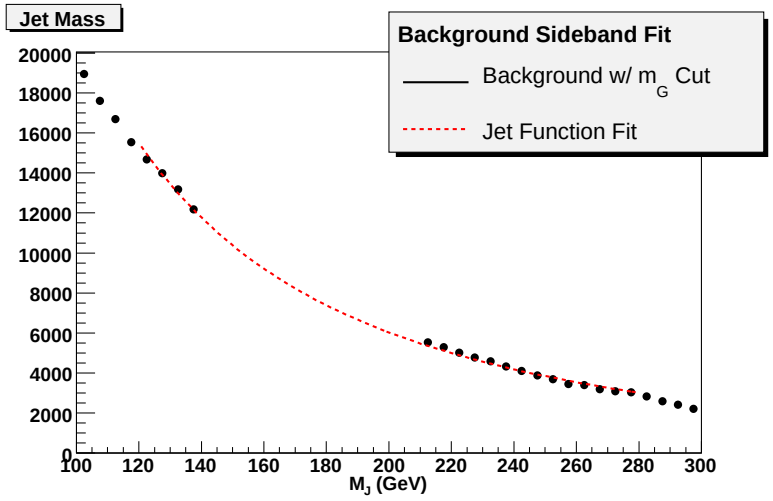

Figure 5.11: A typical example of fitting jet functions to the jet mass distribution in the sideband regions ($120\,\mathrm{GeV} \leq m_J \leq 140\,\mathrm{GeV}$) $\cup$ ($210\,\mathrm{GeV} < m_J < 280\,\mathrm{GeV}$). This plot corresponds to a single-tag analysis with C7 jets with $p_T \geq 1000\,\mathrm{GeV}$.

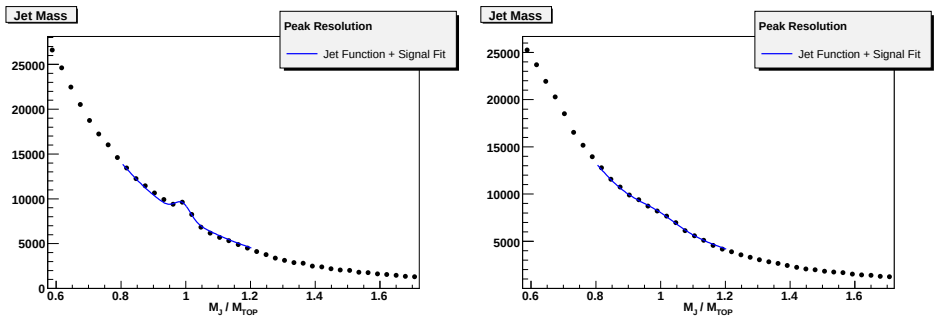

Figure 5.12: The results of fitting jet functions + signal shape to the jet mass distribution in the top mass window. The plot on the left corresponds to a truth-jet analysis. The plot on the right depicts the effects of detector smearing. The statistics reflect 100 fb^{-1} of integrated luminosity.

Our main results have been summarized in the tables below. The results of the fitting procedures for the different p_T cuts and cone sizes are shown in tables 5.5 and 5.6 for integrated luminosities of 100 fb^{-1} and 25 fb^{-1} respectively, and subsequently in tables 5.9 and 5.10 for the double top tagging case which is discussed in the following subsection. Our model for the background in these analyses was already introduced in subsection 5.4.1. Apart from the cone size and p_T^{min}, for each JES, we show the result of the fit regarding the number of background ($B_{\rm FIT}$) and signal ($S_{\rm FIT}$) events in the mass window and their ratio. ΔS is the error on $S_{\rm FIT}$ and p-value and χ^2/ndf are given to describe the quality of the fit in each case [135]. For our analysis, the total number of degree of freedom is 14 (18 bins $-$ 4 fit parameters: β_0, β_1, N_B and N_S).

Most importantly, we give the statistical significance, n_σ (defined in Eq. (5.18)), which is a measure of the probability that fluctuations of the *proposed* background yield in the observed data. The significance value is only as good as the p-value which indicates the goodness of fit. We point out that for entries in which the p-value is lower than, say 5%, the significance figure is probably not reliable. The fitting procedure on that data sample requires further examination, for residuals and bias analyses, for example, but this falls outside the scope of this work. We find two such instances of failed fits, both in table 5.5. This also suggests how we are to interpret the results of the tables. The relatively large background to signal ratio means that small errors in the background induce relatively large errors in the signal. Furthermore, we have not quantified correlations between the background and signal shapes. Similarities in the shapes can lead to small ambiguities, which are reflected in the

fitting parameter errors. The combination of these two difficulties gives rise to an effect, which, strictly speaking, is a defect in the analysis. We remind the reader that we have a large uncertainty in the $t\bar{t}$ signal cross section (see table 5.1), which we have not accounted for in the analysis. We have singled out Sherpa MC data for use in our analyses, and the reader should bear this in mind when interpreting the results in tables 5.5, 5.6, 5.9, 5.10. Small errors in the background shape can yield good fits with high significance figures, and still have relatively large errors in the signal. We are led to interpret the results in the tables as the significance of the peak, relative to the indicated background shape hypothesis (the jet functions in our case). We find that our single tagging method allows us to resolve the $t\bar{t}$ signal from the QCD background with $p_T^{min} \sim 1$ TeV and $25\,\text{fb}^{-1}$ of data. This jet mass analysis does not include any b-tagging or jet-shapes (to be discussed in the following section).

5.4.3 Double Top-Tagging

The above analyses related to single top-tagging are useful not only for $t\bar{t}$ production, but rather for general cases in which we expect to have at least one very energetic top jet. However, for the cases where there is more than one heavy high-p_T particle, we certainly have more information which can be used to distinguish signal from the QCD background. Clearly, $t\bar{t}$ events contain more information than what is encoded in a single top jet mass. We augment the single-tag analysis for the $t\bar{t}$ signal, by simply requiring that the subleading jet mass be in the top mass window, without imposing a p_T cut. This cut preferentially removes more background events than the signal events, without biasing the distributions. The sideband analysis, applied to the leading jet, remains the same as for the single top-tagging case. As we shall see even this simple treatment yields a sizable improvement in the significance. Roughly half of the events have smaller p_T than the minimum p_T for the leading jet as shown in Fig. 5.13. Although, by definition, a subleading jet has smaller p_T than the leading one, its p_T distribution is peaked at the ${p_T}^{min}$, and only small portion of events are in the smaller p_T tail region. The number of events for the signal and background, at the truth-level, are presented in table 5.7. To get an idea on how the subleading mass cut affects our signal and background samples, one can compare the numbers given in table 5.3 with the ones in 5.7. For example, we see that at truth level for $R = 0.4$ and ${p_T}^{min} = 1\,\text{TeV}$ the size of the signal sample is decreased by 50% while the background sample by roughly 12%. This is consistent with the results shown in Figs. 5.8 and 5.5 in which the analysis is done for a fixed p_T.

In principle, one could apply a sideband analysis to the subleading jet.

$p_T{}^{lead} \geq 1000\,\text{GeV}$ Cone $R = 0.4$

JES	B_{FIT}	S_{FIT}	ΔS	n_σ	p-value	χ^2/ndf	$(S/B)_{\text{FIT}}$
0%	106571	6868	671	10.3	0.73	0.74	0.064
5%	120717	8137	715	11.4	0.01	2.01	0.067
-5%	89136	5895	615	9.6	0.95	0.46	0.066

$p_T{}^{lead} \geq 1000\,\text{GeV}$ Cone $R = 0.7$

JES	B_{FIT}	S_{FIT}	ΔS	n_σ	p-value	χ^2/ndf	$(S/B)_{\text{FIT}}$
0%	189185	10892	800	13.7	0.09	1.52	0.058
5%	219189	14020	859	16.4	0.02	1.87	0.064
-5%	151556	9214	720	12.9	0.63	0.83	0.061

$p_T{}^{lead} \geq 1500\,\text{GeV}$ Cone $R = 0.4$

JES	B_{FIT}	S_{FIT}	ΔS	n_σ	p-value	χ^2/ndf	$(S/B)_{\text{FIT}}$
0%	13562	794	224	3.6	1.00	0.26	0.059
5%	17803	1275	256	5.0	0.89	0.58	0.072
-5%	10155	489	193	2.5	0.94	0.49	0.048

$p_T{}^{lead} \geq 1500\,\text{GeV}$ Cone $R = 0.7$

JES	B_{FIT}	S_{FIT}	ΔS	n_σ	p-value	χ^2/ndf	$(S/B)_{\text{FIT}}$
0%	18456	1045	252	4.2	0.75	0.72	0.057
5%	24921	1559	284	5.4	0.96	0.45	0.063
-5%	13315	693	213	3.3	1.00	0.20	0.052

Table 5.5: Estimate of upper limit on significance of peak resolution via single tag method, accounting for detector smearing. S_{FIT} and B_{FIT} are the results of an extended maximum likelihood fit. ΔS is the error on S_{FIT}. Significance n_σ is defined in Eq. (5.18). These results are derived with 100 fb^{-1} of integrated luminosity.

$p_T{}^{lead} \geq 1000\,\text{GeV}$ Cone $R = 0.4$

JES	B_{FIT}	S_{FIT}	ΔS	n_σ	p-value	χ^2/ndf	$(S/B)_{\text{FIT}}$
0%	26642	1712	335	5.1	1.00	0.19	0.064
5%	30206	1995	346	5.8	0.96	0.45	0.066
-5%	22371	1379	288	4.8	1.00	0.11	0.062

$p_T{}^{lead} \geq 1000\,\text{GeV}$ Cone $R = 0.7$

JES	B_{FIT}	S_{FIT}	ΔS	n_σ	p-value	χ^2/ndf	$(S/B)_{\text{FIT}}$
0%	47277	2730	399	6.8	0.98	0.38	0.058
5%	54870	3419	424	8.1	0.87	0.60	0.062
-5%	37910	2274	354	6.4	1.00	0.21	0.060

$p_T{}^{lead} \geq 1500\,\text{GeV}$ Cone $R = 0.4$

JES	B_{FIT}	S_{FIT}	ΔS	n_σ	p-value	χ^2/ndf	$(S/B)_{\text{FIT}}$
0%	3381	201	112	1.8	1.00	0.06	0.059
5%	4418	346	130	2.7	1.00	0.07	0.078
-5%	2519	136	96	1.4	1.00	0.09	0.054

$p_T{}^{lead} \geq 1500\,\text{GeV}$ Cone $R = 0.7$

JES	B_{FIT}	S_{FIT}	ΔS	n_σ	p-value	χ^2/ndf	$(S/B)_{\text{FIT}}$
0%	4609	259	125	2.1	1.00	0.18	0.056
5%	6231	382	144	2.6	1.00	0.12	0.061
-5%	3320	174	99	1.6	1.00	0.06	0.052

Table 5.6: Estimate of upper limit on significance of peak resolution via single tag method, accounting for detector smearing. S_{FIT} and B_{FIT} are the results of an extended maximum likelihood fit. ΔS is the error on S_{FIT}. Significance n_σ is defined in Eq. (5.18). These results are derived with 25 fb^{-1} of integrated luminosity.

However, due to the fact that the p_T is allowed to float, the required analysis would necessarily be more complicated. The double-tagging method increases the signal-to-background ratio, and the significance of the measurements increases. The leading effects of detector resolution and jet energy scale on the signal and background acceptance can be seen in Tables 5.9 and 5.10. We find that our double tagging method yields a reach of up to ${p_T}^{min} \sim 1.5\,\text{TeV}$ with 100 fb^{-1}, without relying on b-tagging or jet-shapes (to be discussed in the following section).

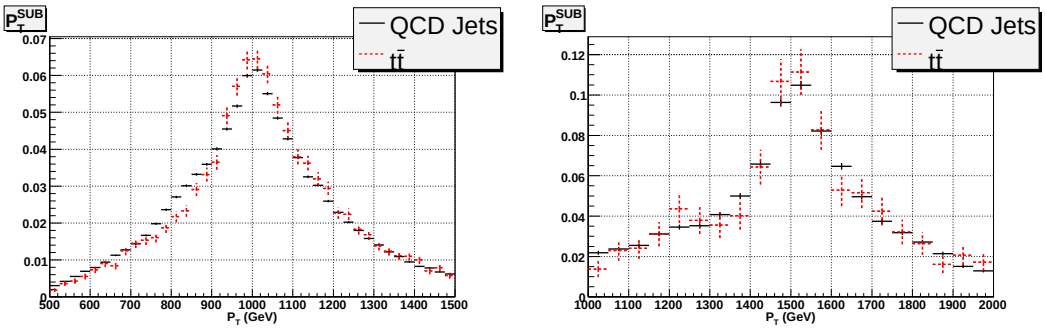

Figure 5.13: We compare the p_T distribution of the subleading jet for the $t\bar{t}$ signal with (the red dotted curve) and without (the black solid curve) leading detector effects. The plot on the left, right corresponds to C4 jets with $\left({p_T}^{lead} \geq 1000, 1500\,\text{GeV}\right)$ respectively.

${p_T}^{lead}$ cut	Cone Size	$t\bar{t}$ (S)	Background (B)	S/B
1000 GeV	C4	3430	13505	0.254
1000 GeV	C7	6302	36765	0.171
1500 GeV	C4	403	1874	0.215
1500 GeV	C7	458	2724	0.168

Table 5.7: Truth-level (no detector effects) results for double-tag jet mass method using, reflecting $100\,\text{fb}^{-1}$ of integrated luminosity.

5.5 Jet Substructure

We discussed simple single- and double-mass tagging methods, and we found that we may need additional handles in order to resolve SM $t\bar{t}$ signals for smaller integrated luminosities or higher p_T. We discuss briefly the possibility

$p_T{}^{lead}$ cut	Cone	S (0% JES)	+5% JES	Δ_5	-5% JES	Δ_{-5}
1000 GeV	C4	2601	2868	-16.4%	2228	-35.0%
1000 GeV	C7	4563	5351	-15.1%	3765	-40.3%
1500 GeV	C4	403	489	21.3%	292	-27.5%
1500 GeV	C7	487	688	50.2%	352	-23.1%
$p_T{}^{lead}$ cut	Cone	B (0% JES)	+5% JES	Δ_5	-5% JES	Δ_{-5}
1000 GeV	C4	13680	15187	12.5%	12054	-10.7%
1000 GeV	C7	39361	45596	24.0%	32192	-12.4%
1500 GeV	C4	2373	3109	65.9%	1746	-6.8%
1500 GeV	C7	4195	5651	107.5%	3014	10.6%

Table 5.8: Acceptance of signal and background for the double tag method, relative to truth-level analysis, accounting for the leading effects of detector resolution and jet energy scale (JES). The $t\bar{t}$ signal is represented in the top half; the QCD jet background is represented in the bottom half. The statistics reflect $100\,\mathrm{fb}^{-1}$ of integrated luminosity. Δ_{JES} is the relative change in background for the indicated JES, relative to truth-level analysis in table 5.7 (cf Eq. (5.20)).

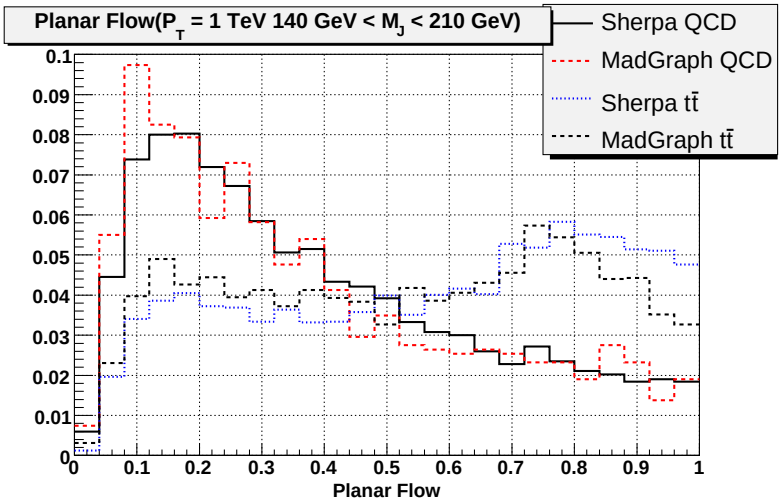

Figure 5.14: The planar flow distribution is plotted for $t\bar{t}$ and QCD jets with mass in the top mass window, $140\,\mathrm{GeV} \leq m_J \leq 210\,\mathrm{GeV}$. Sherpa and MG/ME distributions are represented.

$p_T{}^{lead} \geq 1000\,\text{GeV}$ Cone $R = 0.4$

JES	B_{FIT}	S_{FIT}	ΔS	n_σ	p-value	χ^2/ndf	$(S/B)_{\text{FIT}}$
0%	13488	2789	237	11.8	0.99	0.33	0.207
5%	14653	3395	255	13.3	0.94	0.50	0.232
-5%	11762	2516	212	11.9	0.99	0.31	0.214

$p_T{}^{lead} \geq 1000\,\text{GeV}$ Cone $R = 0.7$

JES	B_{FIT}	S_{FIT}	ΔS	n_σ	p-value	χ^2/ndf	$(S/B)_{\text{FIT}}$
0%	38101	5813	358	16.2	0.72	0.76	0.153
5%	43993	6943	386	18.0	0.66	0.81	0.158
-5%	31290	4655	320	14.6	0.57	0.89	0.149

$p_T{}^{lead} \geq 1500\,\text{GeV}$ Cone $R = 0.4$

JES	B_{FIT}	S_{FIT}	ΔS	n_σ	p-value	χ^2/ndf	$(S/B)_{\text{FIT}}$
0%	2341	430	94	4.6	0.99	0.35	0.184
5%	2968	624	110	5.7	0.96	0.45	0.210
-5%	1593	436	79	5.5	0.82	0.66	0.274

$p_T{}^{lead} \geq 1500\,\text{GeV}$ Cone $R = 0.7$

JES	B_{FIT}	S_{FIT}	ΔS	n_σ	p-value	χ^2/ndf	$(S/B)_{\text{FIT}}$
0%	4053	625	129	5.2	1.00	0.28	0.154
5%	5532	801	128	6.3	0.93	0.50	0.145
-5%	2965	399	100	4.0	1.00	0.14	0.135

Table 5.9: Estimate of upper limit on significance of peak resolution via double tag method, accounting for detector smearing, and jet energy scale (JES). S_{FIT} and B_{FIT} are the results of an extended maximum likelihood fit. ΔS is the error on S_{FIT}. Significance n_σ is defined in Eq. (5.18). These results are derived with 100 fb^{-1} of integrated luminosity.

$p_T{}^{lead} \geq 1000\,\mathrm{GeV}$ Cone $R = 0.4$

JES	B_{FIT}	S_{FIT}	ΔS	n_σ	p-value	χ^2/ndf	$(S/B)_{\mathrm{FIT}}$
0%	3367	696	119	5.9	1.00	0.08	0.207
5%	3658	848	128	6.7	1.00	0.12	0.232
-5%	2931	631	106	6.0	1.00	0.07	0.215

$p_T{}^{lead} \geq 1000\,\mathrm{GeV}$ Cone $R = 0.7$

JES	B_{FIT}	S_{FIT}	ΔS	n_σ	p-value	χ^2/ndf	$(S/B)_{\mathrm{FIT}}$
0%	9521	1452	181	8.1	1.00	0.19	0.152
5%	10997	1732	193	9.0	1.00	0.20	0.158
-5%	7817	1162	160	7.3	1.00	0.22	0.149

$p_T{}^{lead} \geq 1500\,\mathrm{GeV}$ Cone $R = 0.4$

JES	B_{FIT}	S_{FIT}	ΔS	n_σ	p-value	χ^2/ndf	$(S/B)_{\mathrm{FIT}}$
0%	577	111	47	2.4	1.00	0.08	0.192
5%	737	155	55	2.8	1.00	0.11	0.210
-5%	393	109	40	2.8	1.00	0.16	0.277

$p_T{}^{lead} \geq 1500\,\mathrm{GeV}$ Cone $R = 0.7$

JES	B_{FIT}	S_{FIT}	ΔS	n_σ	p-value	χ^2/ndf	$(S/B)_{\mathrm{FIT}}$
0%	1005	159	70	2.7	1.00	0.06	0.158
5%	1376	200	64	3.1	1.00	0.12	0.145
-5%	739	96	50	1.9	1.00	0.04	0.130

Table 5.10: Estimate of upper limit on significance of peak resolution via double tag method, accounting for detector smearing, and jet energy scale (JES). S_{FIT} and B_{FIT} are the results of an extended maximum likelihood fit. ΔS is the error on S_{FIT}. Significance n_σ is defined in Eq. (5.18). These results are derived with 25 fb^{-1} of integrated luminosity.

of using substructure to further analyze energetic jets in the top mass window. We defer the details to our recent work in [25] (see also [154]), where we derive simple analytic expressions to approximate the jet shape variable distributions. For developing additional tools to reslove $t\bar{t}$ signals, there are approaches which exploit information outside of hadronic calorimeter [136] such as tracker or electromagnetic calorimeter. But we limit ourselves to the information encoded only within the hadronic calorimeter to develop significance for resolving $t\bar{t}$ signals. We do not also discuss the possibility of b-tagging for high p_T top-jet [99], which is still under speculation for the range of p_T relevant for our analysis.

Jet shapes are the extensions of well-known event shapes, used at lepton colliders, applied to the analysis of energy flow inside single jets. The fact that we consider only jets with high mass is crucial since it allows us to control the shape of various distributions related to energy flow in a perturbative manner. As an example, we examine the *planar flow* variable, which measures the extent

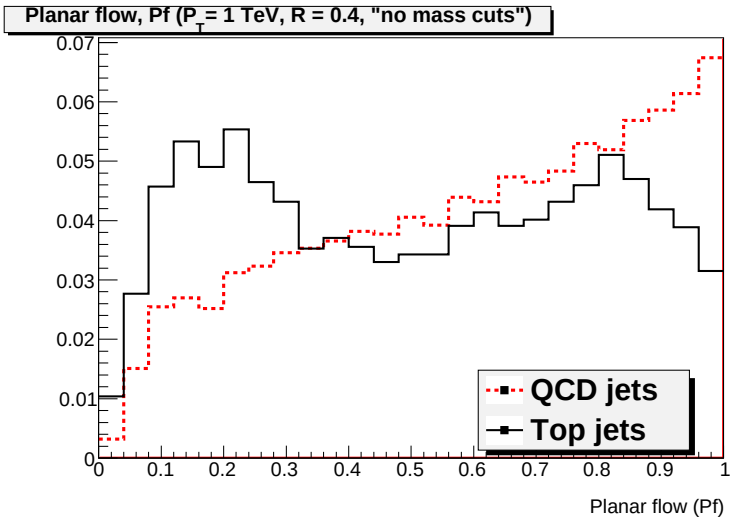

Figure 5.15: The planar flow distribution is plotted for $t\bar{t}$ and QCD jets without fixing jet mass. MG/ME distributions are represented.

to which the energy flow inside the jet is linear or planar. Planar flow (Pf) is defined as follows. We first define an (unnormalized) event shape tensor I_w as[8]

$$I_w^{kl} = \sum_i w_i \frac{p_{i,k}}{w_i} \frac{p_{i,l}}{w_i}\,, \tag{5.21}$$

[8]The overall normalization is not important to this discussion.

where w_i is the energy of particle i in the jet, and $p_{i,k}$ is the k^{th} component of its transverse momentum relative to the thrust axis, which typically coincides with the jet axis. Given I_w, we define Pf as

$$Pf = \frac{4\det(I_w)}{\mathrm{tr}(I_w)^2} = \frac{4\lambda_1\lambda_2}{(\lambda_1+\lambda_2)^2}\,, \tag{5.22}$$

where $\lambda_{1,2}$ are the eigenvalues of I_w. Pf approaches zero for linear shapes and approaches unity for isotropic depositions of energy. In Fig. 5.14, we plot the planar flow distributions for QCD jets and $t\bar{t}$. As can be seen by comparing Figs. 5.14 and 5.15, it is crucial to consider only events in the top mass window. Without a jet mass cut, the jet shape analysis loses its rejection power.

5.6 Top Quark Polarization Measurement

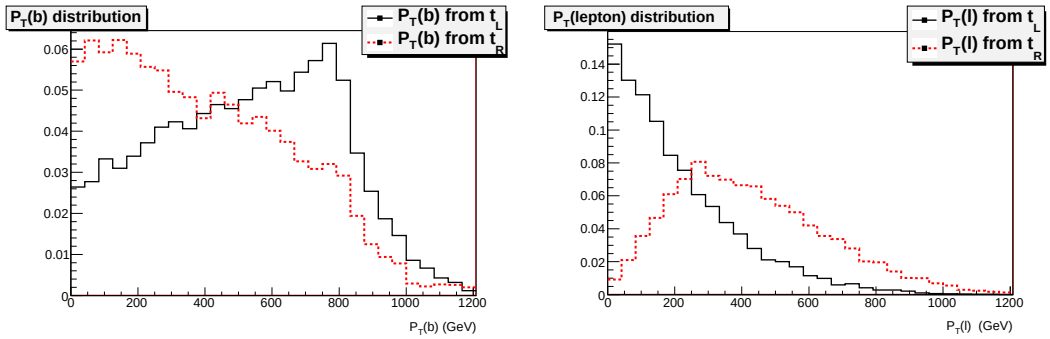

Figure 5.16: In the plot on the left, we show a comparison of the p_T distribution of b quark from t_L (the solid curve) vs. t_R (the dashed curve). In the plot on the right we show the p_T distribution of the charged lepton from t_L (the solid curve) vs. t_R (the dashed curve). We have imposed a lower cut, $p_T^{min} = 1000$ GeV.

In this section, we consider how to exploit b-quarks to measure the polarization of highly boosted hadronic tops. Various new physics models have particle spectra which couple preferentially to one chirality, giving rise to parity violation. Since chirality equals helicity for ultra-relativistic fermions, highly boosted top quarks can help us probe parity violation in the bottom/top quark sector. As is well-known, the top quark decays before the hadronization process occurs, and measurement of the top quark polarization from its leptonic daughters has been studied [94, 95]. We propose using the transverse momentum of the b-quark, inferred from the b-tagged jet, to perform similar measurements. The p_T distribution for the b-quark depends on the chirality of

the top-quark. The b-tagged jets should, therefore, also act as good spin analyzers. In Fig. 5.16, we compare the p_T distributions for leptons and b-quarks, for both left- and right-handed top quarks.

As mentioned earlier, the issue of b-tagging at high p_T is quite challenging at this time (for recent studies see [99]), and a fully quantitative study is not yet available. The main idea is to examine the p_T distribution of b-tagged jets, in events where we believe these jets originate from $t \to bW$. In order to measure the p_T of the b quark, we need to require at least one of the top-jets should be resolved into more than two jets, since we cannot measure the p_T of the b quark inside a single top-jet. As shown in Fig. 5.8, even for high p_T ($p_T \geq 1000\,\text{GeV}$) top jet, with cone size $R = 0.4$, $\sim 30\%$ of top-jets can be resolved into more than two jets. By fixing the cone size for jet reconstruction, it is important to understand any biases towards right-handed or left-handed top quarks. Bottom quarks from t_L have a harder p_T distribution than those from t_R, while the opposite is true for leptons from leptonic top quark decays. If one uses a small reconstruction cone, the efficiencies for jet mass reconstruction between the t_L and t_R may differ. We found a negligible bias using cone jets with $R = 0.4$.

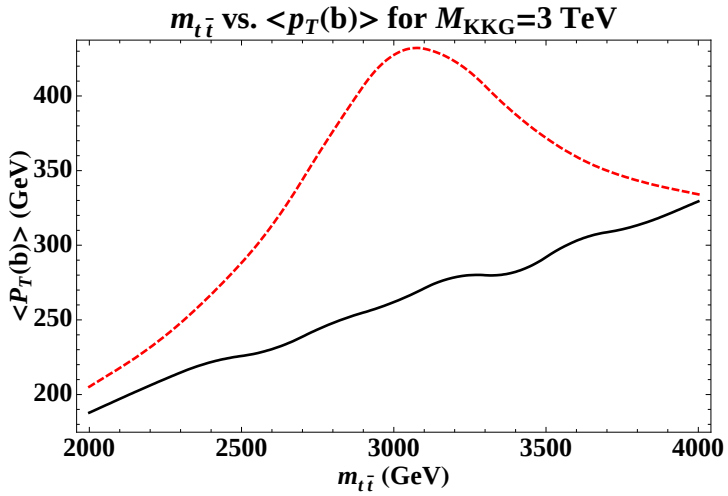

Figure 5.17: We compare the $\langle p_T \rangle$ distribution of the b quark, as predicted by the Standard Model (black solid curve) and by RS1 model with SM fields propagating in the bulk (red dashed curve).

We can develop this discussion further with an example, namely the Randall Sundrum (RS) [137] model with the SM fields propagating in the bulk. We consider the case where the first Kaluza-Klein (KK) excitation of the gluon

has a mass $M_{KKG} = 3$ TeV. We perform this analysis at partonic level. In the model we are considering for using b-quark $\langle p_T \rangle$, KK excitations of the gluon couple to left-handed top quarks $\sim 5\times$ stronger than to right-handed top quarks. Typical cross sections for KK gluon production are relatively small. The (background) SM top quarks are produced dominantly via parity-invariant QCD processes, and tend to wash out the signal. In order to resolve the signature, we are compelled to correlate deviations in the b-quark $\langle p_T \rangle$ spectrum to an excess in KK gluon production. In Fig. 5.17, we compare the mean value of the b-quark p_T spectrum, for the Standard Model and RS1 scenarios with SM fields propagating in the bulk. When correlated to the invariant mass of the KK gluon, we see a substantial deviation in the distribution of the b-quark $\langle p_T \rangle$. In Fig. 5.18, we compare the mean value of the lepton p_T spectrum, for the Standard Model and RS1 scenarios with SM fields propagating in the bulk, where KK excitations of the gluon couple to right-handed top quarks $\sim 5\times$ stronger than to left-handed top quarks.

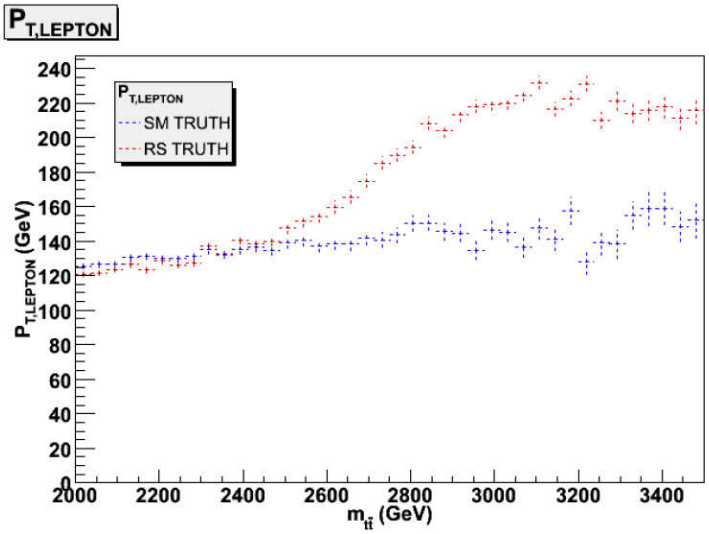

Figure 5.18: We compare the $\langle p_T \rangle$ distributions of the lepton, as predicted by the Standard Model (blue curve) and by RS1 model with SM fields propagating in the bulk (red curve).

5.7 Conclusions

In this study we have mainly focused on high p_T, hadronically decaying, tops in cases where they are fully collimated. Above p_T of 1 TeV the majority of

the top daughters particles will be found inside a single cone jet even when the cone size is as small as $R = 0.4$. Therefore, they are simply denoted as top-jets. The leading background for top-jets comes from high p_T QCD jets. We provided analytic expressions for the QCD jet functions which approximate the background and show consistency with MC data. As an example we consider the case of SM $t\bar{t}$ production, and demonstrate how these jet functions, via side band analysis, allow us to efficiently resolve 1 TeV top-jet from the QCD background with $25\,\mathrm{fb}^{-1}$, and $\sim 1.5\,\mathrm{TeV}$ top-jets with $100\,\mathrm{fb}^{-1}$.

A wide class of new physics models posits $t\bar{t}$ production mechanisms which would significantly contribute to the mass distributions, possibly allowing resolution of excess production with less data. To further improve the significance we consider jet shapes (recently analyzed in [25] and also in [154]), which resolve substructure of energy flow inside cone jets. Augmentation of the analysis, such as the use of jet substructure in combination with a jet mass cut and b-tagging, may improve the signal resolution, allowing us to discover NP signal through top quark channel even with lower luminosity or higher p_T cut. We provided such an example using the *planar flow* jet shape variable, and a detailed analysis is presented in our recent work [25]. We also proposed using the transverse momentum of the bottom quarks to measure top quark polarization as a probe of parity violation.

In this paper we mostly focused on fairly extreme (but not uncommon at the LHC) kinematical configurations where the tops are fully collimated. This has several advantages such as having direct contact with theoretical based calculation of the jet functions and also the ability to consider arbitrarily high top momenta (at least in principle). However, it is clear that some fraction of the hadronic tops will be reconstructed in 2-jet (intermediate) or $\geq$ 3-jet (conventional) topologies. The fraction of events related to the different topologies is a function of the cone size and p_T. Solid reconstruction algorithms and analyses must be flexible enough to interpolate between these different regions. We note that our approach is complimentary to others that have been proposed recently [97, 148, 153, 154]. In most cases, the difference is related to the fact that the tops considered are not fully collimated and a two-jet topology is exploited to increase the signal to background ratio. It would be very interesting and important to derive theoretically based techniques to control the corresponding distribution of the background relevant to the intermediate region. It is likely that there are overlaps between the different regions. Such issues are important to examine in detail. Mastering these complimentary methods may help to make potential new physics observations more robust, if verified via multiple and independent techniques.

Finally, we want to emphasize that the analysis proposed herein is also

applicable to other processes involving, highly boosted, heavy particles such as electroweak gauge bosons, the Higgs and other new physics particles, to which QCD is a leading background as well.

Chapter 6

Jet Event Shapes

At the Large Hadron Collider (LHC), events with highly-boosted massive particles, tops [144], W, Z and Higgs [145] may be the key ingredient for the discovery of physics beyond the standard model [146–148]. In many decay channels, these particles would be identified as high-p_T jets, and any such signal of definite mass must be disentangled from a large background of light-parton ("QCD") jets with a continuous distribution. This background far exceeds such signals, and relying solely on jet mass as a way to reject QCD background from signal would probably not suffice in most cases [25], even using a narrow window for dijets in the search for massive particles such as tops, produced in pairs.

In this chapter, we argue that for massive, high-p_T jets, infrared (IR) safe observables may offer an additional tool to distinguish heavy particle decays from QCD background, perhaps even on an event-by-event basis. We will refer to inclusive observables dependent on energy flow within individual jets as *jet shapes*. A jet within a cone of radius 0.4, for example, may be identified from the energy recorded in roughly fifty 0.1×0.1 calorimeter towers. It thus contains a great deal of information. Perturbatively-calculable, infrared safe jet shapes combined, of course, with IR-safe jet finding algorithms [141–143, 149], may enable us to access that information systematically, and to form a bridge between event generator output and direct theory predictions.

Essentially, any observable that is a smooth functional of the distribution of energy flow among the cells defines an IR-safe jet shape [150]. The jet mass is one example, but a single jet may be analyzed according to a variety of shapes. In particular, the jet mass distribution has large corrections when the ratio of the jet mass to jet energy is small [151], but can be computed at fixed order when the logarithm of that ratio has an absolute value of order unity. Once the jet mass is fixed at a high scale, a large class of other jet shapes becomes perturbatively calculable with nominally small corrections. Indeed,

a jet whose mass exceeds $\mathcal{O}(100\,\mathrm{GeV})$ becomes, from the point of view of perturbation theory, much like the final state in leptonic annihilation at a similar scale. At such energies, event shapes, which in the terminology of this paper are jet shapes extended over all particles, have been extensively studied in perturbation theory [152]. In this study we explore the possibility that perturbative predictions for jet shapes differ between those jets that originate from the decay of heavy particles, and those which result from the showering of light quarks and gluons. Very interesting related studies have recently appeared in [147, 153, 154].

6.1 Jet Shapes and Jet Substructure

We would like to identify jet shapes for which perturbative predictions differ significantly between QCD and other high-p_T jets, focusing on relatively narrow windows in jet mass. In our companion paper [25] we have discussed how to calculate the jet mass distribution for the QCD background. We now extend this argument to the computation of other jet shape observables.

We emphasize that, because the observables under consideration are IR-safe, we may calculate them as power series in α_s, starting at first order for the QCD background, and zeroth order for an electroweak decay signal.

Our approximation for the jet cross sections is based on factorization for the relatively-collinear partons that form a jet from the remainder of the process [151]. For a jet of cone size R, contributions that do not vanish as a power of R are generated by a function that depends only on the flavor of the parent parton, its transverse momentum, and the factorization scale. Denoting a jet shape by e, we then have,

$$\frac{d\sigma}{dm_J\,de} = \sum_c \int_{{p_T}^{min}}^{\infty} dp_T \frac{d\hat{\sigma}_c(p_T)}{dp_T}\ \frac{dJ_c(e, m_J, p_T, R)}{de}\,, \tag{6.1}$$

where $d\hat{\sigma}/dp_T$ includes the hard scattering and the parton distributions of the incoming hadrons, and where the jet function for partons c in the final state is defined formally as in Refs. [25, 155].

In Ref. [25], we have found that the distribution of QCD jet masses in the range of hundreds of GeV is fairly well described by the jet function in Eq. (6.1) at order α_s, based on two-body final states. It thus seems natural to anticipate that for QCD jets, energy flow inside the cone would produce a *linear* deposition in the detector [147, 148, 153, 154, 156]. While this is certainly the case for an event consisting of two sub-jets, it is a simpler condition, and more easily quantified. Indeed, such a linear flow should also characterize jets

from the two-body decay of a highly-boosted, massive particle. We will see below that relatively simple jet shapes can help distinguish QCD jets from many top-decay jets that involve three-body decay. We will also see that jet shapes can help separate samples that contain both QCD jets and jets from two-body decays, such as those of the W, Z or Higgs. We emphasize that a single event may be analyzed by a variety of jet shapes, so that the resolution associated with each one need not be dramatic, so long as they are effectively independent.

6.2 Top decay and planar flow

The linear flow of QCD jets at leading order should be compared with a $\geq$ 3-body decay where the energy deposition tends to be *planar*, covering a two-dimensional region of the detector. An IR-safe jet shape, which we denote as *planar flow*, a two-dimensional version of the "D parameter" [157–160], distinguishes planar from linear configurations. The utility of a closely-related observable was emphasized in Ref. [154].

Planar flow is defined as follows. We first construct for a given jet a matrix I_ω as

$$I_\omega^{kl} = \frac{1}{m_J} \sum_i \omega_i \frac{p_{i,k}}{\omega_i} \frac{p_{i,l}}{\omega_i} \,, \tag{6.2}$$

where m_J is the jet mass, ω_i is the energy of particle i in the jet, and $p_{i,k}$ is the k^{th} component of its transverse momentum relative to the axis of the jet's momentum. Given I_ω, we define Pf for that jet as

$$Pf = \frac{4 \det(I_\omega)}{\mathrm{tr}(I_\omega)^2} = \frac{4\lambda_1\lambda_2}{(\lambda_1+\lambda_2)^2} \,, \tag{6.3}$$

where $\lambda_{1,2}$ are the eigenvalues of I_ω. Pf vanishes for linear shapes and approaches unity for isotropic depositions of energy.

Jets with pure two-body kinematics have a differential jet function fixed at zero planar flow,

$$\frac{1}{J} \left(\frac{dJ}{dPf} \right)_{\text{2body}} = \delta(Pf) \,. \tag{6.4}$$

This would apply to leading order for events with highly boosted weak gauge boson, Higgs and QCD jets. On the other hand, events that are characterized by $\geq$ 3-body kinematics have a smooth distribution.

Realistic QCD jets have, of course, nonzero Pf. Because Pf is an IR safe observable, however, its average value can depend only on the hard momentum scales of the jet, that is, m_J and p_T. This suggests an average Pf of order

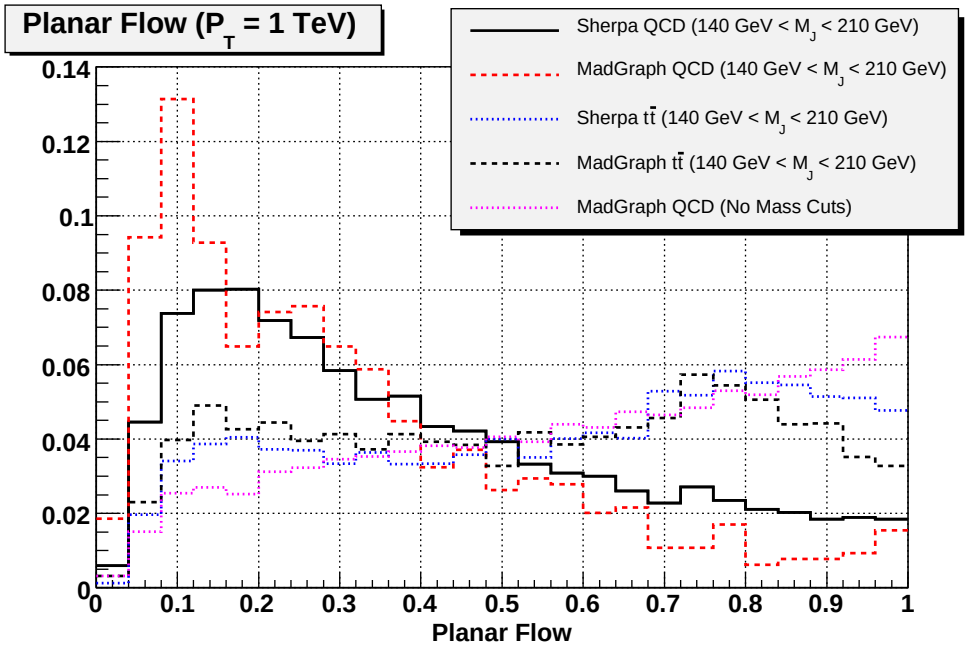

Figure 6.1: The planar flow distribution for QCD and top jets obtained from MadGraph and Sherpa. Distributions are normalized to the same area.

$\alpha_s(m_J) \sim 0.1$ for high jet masses, times at most logarithms that are order unity for these heavy jets. Correspondingly, higher order corrections should, by analogy to two-jet event shapes [152], replace the delta function of Eq. (6.4) with a differential distribution that peaks near the origin and then falls off. For jets resulting from three-body decay, on the other hand, we anticipate that corrections in α_s shift the already-smooth distribution modestly, without affecting its overall shape. Finally, for the vast majority of high-p_T QCD jets, with masses $m_J \ll p_T$, planar flow corrections associated with multi-gluon emission may be expected to be large, and to shift Pf to order unity.

These considerations are confirmed in Fig. 6.1, where we show the Pf distribution for QCD jet and hadronic $t\bar{t}$ events, for $R = 0.4$, $p_T = 1000\,\text{GeV}$ and $m_J = 140 - 210\,\text{GeV}$ as obtained from MadGraph [161] and Sherpa [162] with jet reconstruction via (the IR-safe algorithm) SISCone [143]. We see that QCD jets peak around small values of Pf, while the top jet events are more dispersed. A planar flow cut around 0.5 would clearly remove a considerably larger proportion of QCD jets than top jets. Figure 6.1 also shows that if we do not impose these mass cuts, for the QCD jets planar flow becomes larger and almost indistinguishable from that of top jets.

6.3 Two-body decay

While planar flow can help enrich samples with characteristically three- and higher-body kinematics, other jet shapes can also provide additional information on events with relatively low Pf. Here, we will still wish to distinguish the QCD background from highly boosted electroweak gauge bosons or Higgs [156] as well as from top jets whose Pf happens to be relatively low. We begin with jets that are linear at lowest order, and identify a set of jet shapes that have some power to distinguish between the two. Fixing p_T, R and m_J leaves only one free parameter to characterize the shape.

The QCD jet function for two-body kinematics is defined as a matrix element in [25] and is readily expressed as an integral over θ_s, the angle of the softer particle relative to the jet momentum axis. For a quark jet, for example, the integrand is therefore the differential jet function,

$$\frac{dJ^{QCD}}{d(c\theta_s)} = \frac{\alpha_s C_F \beta_z z^2}{4\pi m_J^2 (1-\beta_z c\theta_s)(2(1-\beta_z c\theta_s)-z^2)} \times \left[\frac{(2(1+\beta_z)(1-\beta_z c\theta_s)-z^2(1+c\theta_s))^2}{z^2(1+c\theta_s)(1-\beta_z c\theta_s)} + 3(1+\beta_z) + \frac{z^4(1+c\theta_s)^2}{(1-\beta_z c\theta_s)(2(1+\beta_z)(1-\beta_z c\theta_s)-z^2(1+c\theta_s))} \right], \tag{6.5}$$

where $z \equiv m_J/p_T$, $\beta_z \equiv \sqrt{1-z^2}$ and $c\theta_s \equiv \cos\theta_s$. The jet mass function, for a jet cone of size R, is found by the integral

$$J(R,z) = \int_{\theta_m}^{R} d\theta_s \left(\frac{dJ}{d\theta_s}\right), \tag{6.6}$$

where $\theta_m = \cos^{-1}\left(\sqrt{1-z^2}\right)$ is the minimum angle the softer particle can make with the jet axis. At $\theta_s = \theta_m$, both particles have the same energy and angle to the jet axis.

It is natural to ask how the integrated jet function, Eq. (6.6) depends of the jet algorithm used to define the jet, and in particular how results for cone jets compare to results when jets are identified by k_t or the newer "anti-k_t" algorithms [142, 149]. For the low orders and small cones discussed here, this relationship is straightforward.

Reference [149] introduces a class of k_t algorithms, for which two particles

are within the same jet if their distance d_{ij} is less than d_B, given by

$$\begin{aligned} d_{ij} &= \min(k_{T,i}^{2p}, k_{T,j}^{2p}) \frac{r_{ij}^2}{R_{k_t}^2}\,, \qquad (6.7) \\ d_B &= \min(k_{T,i}^{2p}, k_{T,j}^{2p})\,, \qquad (6.8) \end{aligned}$$

where $r_{ij} = \sqrt{\Delta\eta^2 + \Delta\phi^2}$ is the distance between particles i and j in the rapidity-azimuthal angle plane. The choice $p = 1$ defines a standard k_t algorithm, and $p = -1$ the anti-k_t. For small cones, $r_{ij} \approx \theta_{ij}$, where θ_{ij} is the angle between two particles. At lowest order, that is for two particles in the final state, for both positive and negative values of p, these algorithms constrain r_{ij}^2, and therefore θ_{ij}, by

$$0 < \frac{r_{ij}^2}{R_{k_t}^2} < 1\,. \qquad (6.9)$$

As in Eq. (6.6) the energy and angles of the massless two particles are related at fixed jet mass and fixed transverse momentum, through

$$\begin{aligned} m_J^2 &= 2k_{T,i}k_{T,j}(\cosh\Delta\eta - \cos\Delta\phi) \\ &\approx k_{T,i}k_{T,j}\left((\Delta\eta)^2 + (\Delta\phi)^2\right)\,, \qquad (6.10) \end{aligned}$$

where again we assume small angles. Changing variables from θ_s to r_{ij}, or equivalently θ_{ij}, is straightforward, and the basic integral for an inclusive jet function in Eq. (6.6) is of the same form for a cone and a k_t (or anti-k_t) jet at lowest nontrivial order. At this order the difference is that in k_t algorithms the parameter R_{k_t} directly restricts the distance between the two particles, in contrast to a cone size R, which restricts the distance of each particle to the jet axis. The only difference is in the upper limit of Eq. (6.6). The integral found with a cone jet of size R corresponds to a generalized k_t algorithm with parameter $R_{k_t}(R)$. Their relation can be easily found from the dependence of r_{ij} in θ_s,

$$\begin{aligned} R_{k_t}(R) &= R + \sin^{-1}\left(\frac{z^2\sin R}{(1+\beta_z^2) - 2\beta_z\cos R}\right) \\ &= R + \frac{z^2}{2}\frac{\sin R}{1-\cos R} + \mathcal{O}(z^4)\,, \qquad (6.11) \end{aligned}$$

a result that depends on z, the ratio of the jet energy to its mass. We see that for highly boosted heavy jets, or for jets of low mass, with $z \ll 1$, $R_{k_t}(R) \to R$, and the two integrated jet functions are identical. The k_t algorithm parameter, R_{k_t}, approaches the cone jet parameter, R, from above because the k_t

algorithm is slightly more restrictive at this order. For the remainder of our discussion, we shall assume a cone jet algorithm.

For signal events from highly-boosted massive gauge bosons, we consider separately the cases when it is longitudinal and when it has helicity ($h = \pm 1$),

$$\begin{aligned} \frac{dJ^{\rm Long}}{d(c\theta_s)} &= \frac{C}{(1-\beta_z c\theta_s)^2}\,, \\ \frac{dJ^{h=\pm 1}}{d(c\theta_s)} &= \frac{C}{(1-\beta_z c\theta_s)^2}\left(1-\frac{(zs\theta_s)^2}{2(1-\beta_z c\theta_s)^2}\right), \end{aligned} \tag{6.12}$$

where $s\theta_s \equiv \sin\theta_s$ and C is a proportionality coefficient, totally determined from the two-body decay kinematics. We can interpret the appropriately normalized differential jet functions, $P^x(\theta_s) = (dJ^x/d\theta_s)/J^x$ as the probability to find the softer particle at an angle between θ_s and $\theta_s + \delta\theta_s$. As the ratio z decreases, the decay products become boosted and the cone shrinks. For QCD jets from light partons, however, this shrinkage is much less pronounced. From Fig. 6.2 we can see that the jet functions for the gauge boson distributions of Eq. (6.12) fall off with θ_s faster than do QCD jets, Eq. (6.5). This observation suggests that the signal (vector boson-jet) and background (QCD jets) have different shapes for fixed p_T, R and jet mass. This may be used to obtain an improved rejection power against background events. We now consider a class of jet shapes, *angularities*, originally introduced in Refs. [155, 163] for two-jet events in e^+e^- annihilation. A natural generalization of these jet shapes to single-cone jets of large mass m_J is

$$\tilde{\tau}_a(R, p_T) = \frac{1}{m_J}\sum_{i\in jet}\omega_i\,\sin^a\left(\frac{\pi\theta_i}{2R}\right)\left[1-\cos\left(\frac{\pi\theta_i}{2R}\right)\right]^{1-a}, \tag{6.13}$$

with m_J the jet mass. The arguments of the trigonometric functions vary from zero to $\pi/2$ as θ increases from zero to R, that is, over the size of the cone. These weights revert to the angularities as defined in for leptonic annihilation in [155, 163] when $R = \pi/2$, so that the cone is enlarged to a hemisphere and m_J is replaced by the center-of-mass energy in a two-jet event. For massive jets, the angularities are clearly non-zero at lowest order, in contrast to the lowest order planar flow, Eq. (6.4). Then, precisely because of their IR safety, higher-order corrections to the τ_a distributions should be moderate.

As the parameter a varies, the angularities give more or less weight to particles at the edge of the cone compared to those near the center. From the differential jet distribution functions in Eqs. (6.5) and (6.12) and the definition of $\tilde{\tau}_a$ we can obtain expressions for $P^x(\tilde{\tau}_a)$ [as before x= sig (signal) or QCD], the probability to find a jet with an angularity value between $\tilde{\tau}_a$ and $\tilde{\tau}_a + \delta\tilde{\tau}_a$

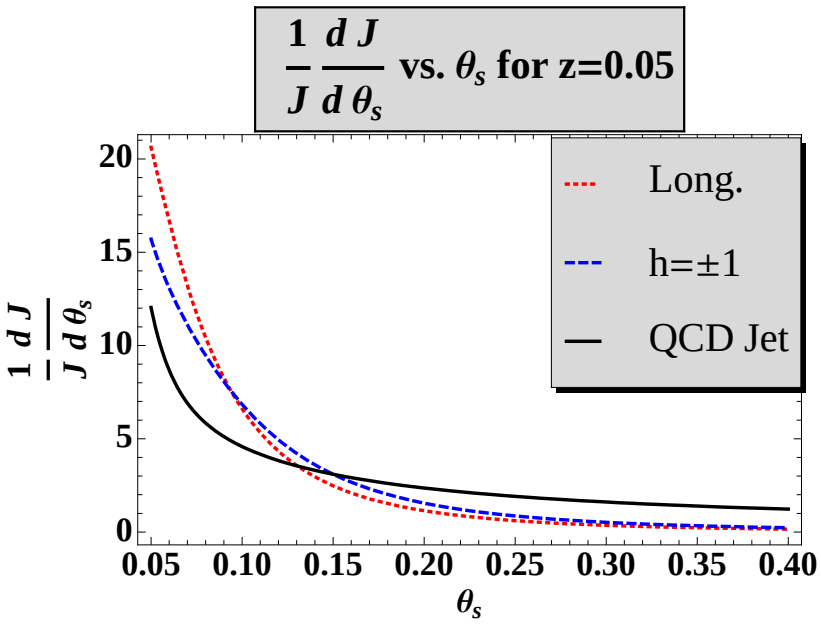

Figure 6.2: Normalized jet distributions for gauge bosons, in Eq. (6.12), and QCD in Eq. (6.5).

at fixed p_T, R, m_J and a. Our focus is not on the form of the individual distributions but rather on the ratio of the signal to background

$$R(\tilde{\tau}_a) = \frac{P^{\rm sig}(\tilde{\tau}_a)}{P^{\rm QCD}(\tilde{\tau}_a)} \,. \tag{6.14}$$

In Fig. 6.3 we show $R^{\tilde{\tau}_a}$ for $a = -2$ and $z = 0.05$, for the different vector boson polarizations. In Fig. 6.4 we show the corresponding angularity distributions at the event generator level, comparing the output of MadGraph for longitudinal Z boson production to QCD jets in the same mass window. The pattern suggested by the lowest-order prediction of Fig. 6.3 is confirmed by the output of the event generator, with signal and data curves crossing in Fig. 6.3 near $\tilde{\tau}_{-2} = 0.02$, where $R(\tilde{\tau}_{-2}) \sim 1$. Comparing Eqs. (6.5) and (6.12), we observe that the QCD jet distribution is more peaked as $\theta_s \to \theta_m$ than the Z boson jet, corresponding to a sharper falloff with increasing $\tilde{\tau}_{-2}$. In this case, $\theta_m \sim 4 \times 10^{-3}$, and the maximum of the lowest-order angularity distribution would be in the lowest bin of the figure. In the event generator output, we see a slight shift to the right for the QCD distribution, due to radiation. This, however, does not affect the clear contrast between the QCD and Z boson cases.

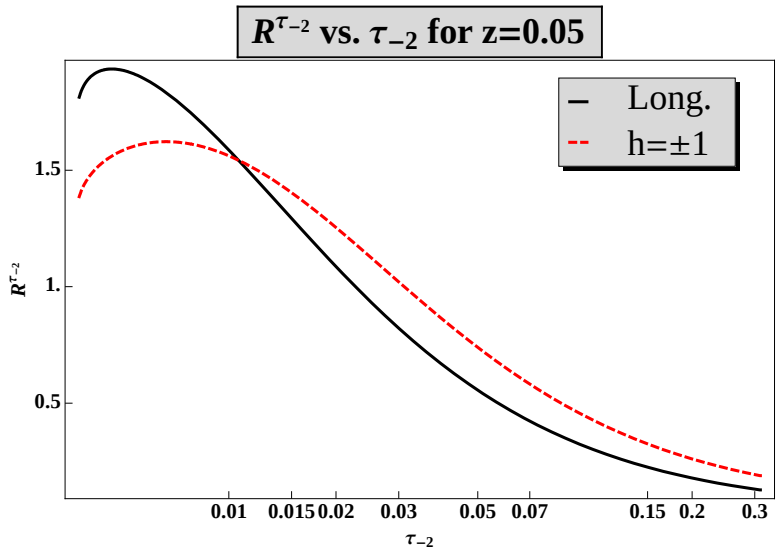

Figure 6.3: The ratio between the signal and background probabilities to have jet angularity $\tilde{\tau}_{-2}$, $R^{\tilde{\tau}_{-2}}$.

6.4 Linear three-body decay

The leading-order differential top jet function can be obtained by considering its three-body decay kinematics. The analytic expression is similar to Eq. (6.12) for the two-body case, although a bit more elaborate. In the following we simply point out a few features that may help angularities to distinguish top jets from background, even when they have relatively linear flow.

The lowest-order three-body distribution is fully characterized by three angles. The first, θ_b, is the angle between the b quark and the jet axis. The second, θ_{Wq}, is the angle of the quark (from W-decay) relative to the W. The third, ϕ, is the angle of the same quark relative to the plane defined by the W and the b. For an on-shell W, the distributions peak around $\theta_b = \theta_m$ (as in two-body kinematics) and $\theta_{Wq} = \theta_{m(W)}$ the minimal angle relative to the W momenta in the W rest frame. Because it is massive, the W's decay products move in somewhat different directions, even in the boosted frame, and their relative orientation induces the ϕ-dependence. Clearly, planar flow has maxima for odd multiples of $\phi = \pi/2$, and vanishes at lowest order at multiples of π. To tag top events at zero planar flow, angularities can be of use. In Fig. 6.5 we plot $\tilde{\tau}_{-5}$ as a function of the azimuthal angle of the $W(q\bar{q})$ pair, ϕ, for a typical top jet event. We also show the corresponding value for the two-body case (clearly ϕ independent). For illustration we choose

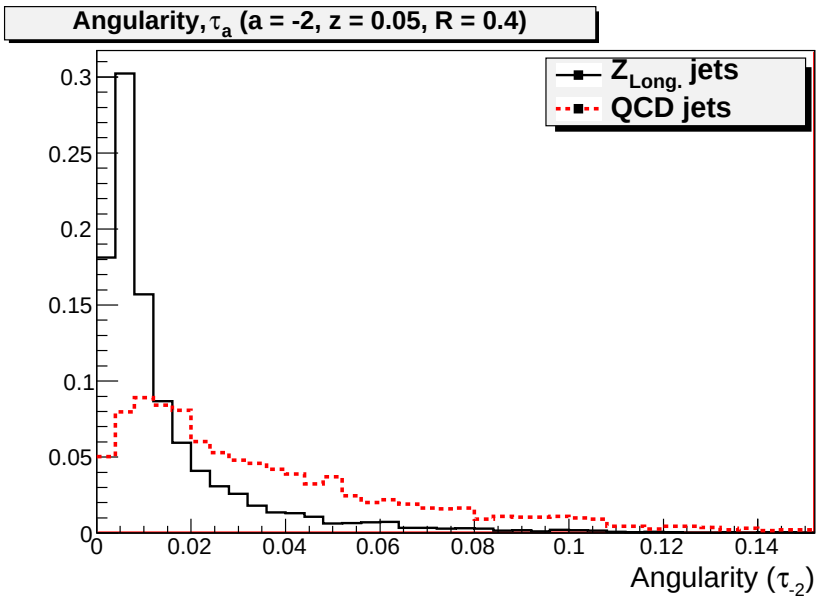

Figure 6.4: The angularity distribution for QCD (red-dashed curve) and longitudinal Z (black-solid curve) jets obtained from MadGraph. Both distributions are normalized to the same area.

the kinematical configuration that maximizes the corresponding differential jet distributions. We notice that this top angularity has maxima with ϕ at zero and π at values far above the most likely two-body configuration. The reason is simply that angularities with large negative values of a tend to emphasize flow at the edge of the cone. Other values of a weight individual jets differently in general. We consider this simple plot, along with the forgoing examples from event generators, as strong evidence for the potential of jet shape analysis.

In summary, planar flow, angularities, and jet shapes that are as yet to be invented, may afford a variety of tools with which to distinguish the quantum mechanical histories of jets, whether resulting from heavy particle decay, or strong interactions. Our approach is complementary to others that have been proposed recently [147, 148, 153, 154]. For the most part, these references analyze a subclass of highly boosted tops that are not fully collimated as seen for a specific choice of jet-finder. Efficiencies for these event may then be quite high. Here, we take a less exclusive approach, accepting all data in a given mass range. This enables us to readily identify analytic approximations inspired by factorization. As demonstrated in this paper and its companion [25], our treatment allows one to have fairly straightforward theoretical control over the expected observed distributions. This allows us to interpret the data (only

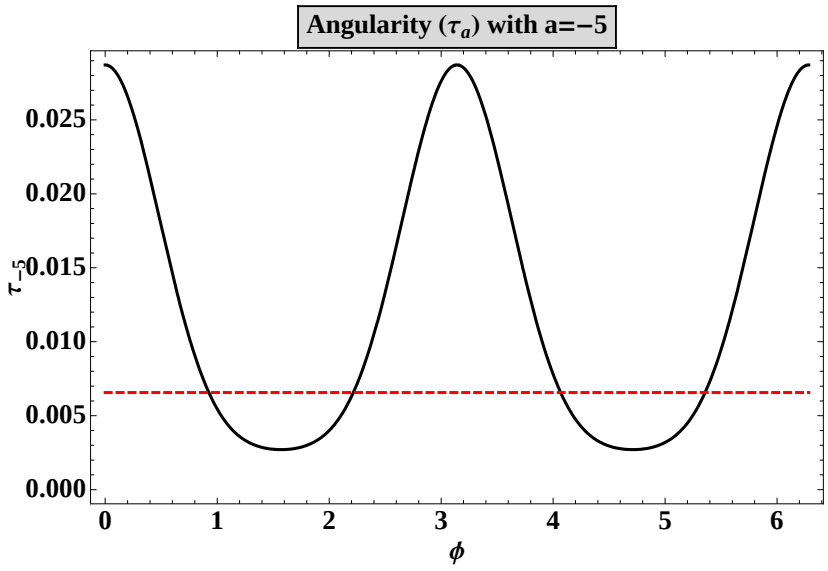

Figure 6.5: Angularity, $\tilde{\tau}_{-5}$ as a function of the azimuthal angle of the $W(q\bar{q})$ pair, ϕ_q, for a typical top jet event, compared to the typical case two-body kinematics.

from Monte-Carlo at this point) in the light of simple predictions that are based directly on theory.

Bibliography

[1] T. P. Cheng and L. F. Li, "Gauge Theory Of Elementary Particle Physics," *Oxford, Uk: Clarendon (1984) 536 P. (Oxford Science Publications)*

[2] O. W. Greenberg, Phys. Rev. Lett. **13**, 598 (1964) M. Han, Y. Phys. Rev. **139B**, 1609 (1965)

[3] D.J. Gross and F. Wilczek, Phys. Rev. Lett. **30**, 1343 (1973), H.D. Politzer, Phys. Rev. Lett. **30**,1346 (1973), S. Weinberg,Phys. Rev. Lett. **31** 494, (1973)

[4] C. Aubin et al. (HPQCD Collab.), Phys. Rev. D70, 031504 (2004), C. Aubin et al. (MILC Collab.), Phys. Rev. D70, 114501 (2004), T. Ishikawa et al. (CP-PACS Collab.), Nucl. Phys. (Proc. Supp.) B140, 225 (2005),D. Becirevic et al. (SPQcdR Collab.), Nucl. Phys. (Proc. Supp.) B140, 246 (2005), M. Gockeler et al. (QCDSF Collab.), hep-ph/0409312, M. Della Morte et al. (ALPHA Collab.), hep-lat/0507035, S. Aoki et al. (JLQCD Collab.), Phys. Rev. D68, 054502 (2003), A. Ali Khan et al. (CP-PACS Collab.), Phys. Rev. D65, 054505 (2002); Erratum ibid., D67, 059901 (2003).

[5] M. Creutz, "Quarks, Gluons And Lattices," *Cambridge, Uk: Univ. Pr. (1983) 169 P. (Cambridge Monographs On Mathematical Physics)*

[6] L. D. Faddeev and V. N. Popov, Phys. Lett. B **25**, 29 (1967).

[7] G. Sterman, "An Introduction to quantum field theory," *Cambridge, UK: Univ. Pr. (1993) 572 p*

[8] J. C. Collins, "Renormalization. An Introduction To Renormalization, The Renormalization *Cambridge, UK: Univ. Pr. (1984) 380p*

[9] S. Weinberg, "The quantum theory of fields. Vol. 2: Modern applications," *Cambridge, UK: Univ. Pr. (1996) 489 p*

[10] T. van Ritbergen, J. A. M. Vermaseren and S. A. Larin, Phys. Lett. B **400**, 379 (1997) [arXiv:hep-ph/9701390]. M. Czakon, Nucl. Phys. B **710**, 485 (2005) [arXiv:hep-ph/0411261].

[11] J. Smith, arXiv:hep-ph/0003193.

[12] J. C. Collins, D. E. Soper and G. Sterman, Adv. Ser. Direct. High Energy Phys. **5**, 1 (1988) [arXiv:hep-ph/0409313].

[13] G. Sterman, arXiv:hep-ph/9606312.

[14] G. Sterman, Phys. Rev. D **17**, 2773 (1978). Phys. Rev. D **17**, 2789 (1978).

[15] S. B. Libby and G. Sterman, Phys. Rev. D **18**, 3252 (1978).

[16] S. Coleman and R. E. Norton, Nuovo Cim. **38**, 438 (1965).

[17] J. C. Collins and D. E. Soper, Nucl. Phys. B **193**, 381 (1981) [Erratum-ibid. B **213**, 545 (1983)].

[18] G. Sterman, Nucl. Phys. B **281**, 310 (1987).

[19] H. Contopanagos, E. Laenen and G. Sterman, Nucl. Phys. B **484**, 303 (1997) [arXiv:hep-ph/9604313].

[20] N. Kidonakis and G. Sterman, Nucl. Phys. B **505**, 321 (1997) [arXiv:hep-ph/9705234].

[21] N. Kidonakis, G. Oderda and G. Sterman, arXiv:hep-ph/9805279; N. Kidonakis, G. Oderda and G. Sterman, Nucl. Phys. B **531**, 365 (1998) [arXiv:hep-ph/9803241].

[22] L. G. Almeida, G. Sterman and W. Vogelsang, Phys. Rev. D **78**, 014008 (2008) [arXiv:0805.1885 [hep-ph]].

[23] L. G. Almeida, G. Sterman and W. Vogelsang, Phys. Rev. D **80**, 074016 (2009) [arXiv:0907.1234 [hep-ph]].

[24] L. G. Almeida, S. J. Lee, G. Perez, G. Sterman, I. Sung and J. Virzi, Phys. Rev. D **79**, 074017 (2009) [arXiv:0807.0234 [hep-ph]].

[25] L. G. Almeida, S. J. Lee, G. Perez, I. Sung and J. Virzi, Phys. Rev. D **79**, 074012 (2009) [arXiv:0810.0934 [hep-ph]]. Dihadron

[26] P. Aurenche, M. Fontannaz, J. P. Guillet, B. A. Kniehl and M. Werlen, Eur. Phys. J. C **13**, 347 (2000) [arXiv:hep-ph/9910252].

[27] U. Baur *et al.*, arXiv:hep-ph/0005226.

[28] C. Bourrely and J. Soffer, Eur. Phys. J. C **36**, 371 (2004) [arXiv:hep-ph/0311110].

[29] B. A. Kniehl, G. Kramer and B. Pötter, Nucl. Phys. B **597**, 337 (2001) [arXiv:hep-ph/0011155].

[30] D. de Florian and W. Vogelsang, Phys. Rev. D **71**, 114004 (2005) [arXiv:hep-ph/0501258].

[31] A. Adare *et al.* [PHENIX Collaboration], Phys. Rev. D **76**, 051106 (2007) [arXiv:0704.3599 [hep-ex]]; Phys. Rev. D **79**, 012003 (2009) [arXiv:0810.0701 [hep-ex]].

[32] J. Adams *et al.* [STAR Collaboration], Phys. Rev. Lett. **97**, 152302 (2006) [arXiv:nucl-ex/0602011].

[33] I. Arsene *et al.* [BRAHMS Collaboration], Phys. Rev. Lett. **98**, 252001 (2007) [arXiv:hep-ex/0701041].

[34] C. De Marzo *et al.* [NA24 Collaboration], Phys. Rev. D **42**, 748 (1990).

[35] H. B. White *et al.* [E711 Collaboration], Phys. Rev. D **48**, 3996 (1993); H. B. White, *A Study of angular dependence in parton-parton scattering from massive hadron pair production*, PhD Thesis, FERMILAB-THESIS-1991-39, FSU-HEP-910722, UMI-92-02321, 1991.

[36] M. Begel [E706 Collaboration], *Production of high mass pairs of direct photons and neutral mesons in a Tevatron fixed target experiment*, PhD Thesis, FERMILAB-THESIS-1999-05, UMI-99-60725, 1999; see also: L. Apanasevich *et al.* [E706 Collaboration], Phys. Rev. Lett. **81**, 2642 (1998) [arXiv:hep-ex/9711017].

[37] A. L. S. Angelis *et al.* [CCOR Collaboration], Nucl. Phys. B **209**, 284 (1982).

[38] P. Chiappetta, R. Fergani and J. P. Guillet, Z. Phys. C **69**, 443 (1996).

[39] J. F. Owens, Phys. Rev. D **65**, 034011 (2002) [arXiv:hep-ph/0110036].

[40] T. Binoth, J. P. Guillet, E. Pilon and M. Werlen, Eur. Phys. J. C **24**, 245 (2002); Eur. Phys. J. direct C **4**, 7 (2002) [arXiv:hep-ph/0203064].

[41] G. Sterman, Nucl. Phys. B **281**, 310 (1987); S. Catani and L. Trentadue, Nucl. Phys. B **327**, 323 (1989); Nucl. Phys. B **353**, 183 (1991).

[42] A. Idilbi, X. d. Ji and F. Yuan, Nucl. Phys. B **753**, 42 (2006) [arXiv:hep-ph/0605068]; T. Becher, M. Neubert and G. Xu, JHEP **0807**, 030 (2008) [arXiv:0710.0680 [hep-ph]].

[43] N. Kidonakis, G. Oderda and G. Sterman, Nucl. Phys. B **525**, 299 (1998) [arXiv:hep-ph/9801268]; Nucl. Phys. B **531**, 365 (1998) [arXiv:hep-ph/9803241].

[44] N. Kidonakis and J. F. Owens, Phys. Rev. D **63**, 054019 (2001) [arXiv:hep-ph/0007268].

[45] E. Laenen and G. Sterman, in *The Fermilab Meeting, DPF 1992* (World Scientific, Singapore, 1993) Vol. 1, p. 987.

[46] G. Sterman and W. Vogelsang, JHEP **0102**, 016 (2001) [arXiv:hep-ph/0011289].

[47] A. Mukherjee and W. Vogelsang, Phys. Rev. D **73**, 074005 (2006) [arXiv:hep-ph/0601162].

[48] G. Bozzi, S. Catani, D. de Florian and M. Grazzini, Nucl. Phys. B **791**, 1 (2008) [arXiv:0705.3887 [hep-ph]].

[49] G. Sterman and W. Vogelsang, Phys. Rev. D **74**, 114002 (2006) [arXiv:hep-ph/0606211].

[50] M. Cacciari and S. Catani, Nucl. Phys. B **617**, 253 (2001) [arXiv:hep-ph/0107138].

[51] M. Sjödahl, arXiv:0906.1121 [hep-ph].

[52] N. Kidonakis, E. Laenen, S. Moch and R. Vogt, Phys. Rev. D **64**, 114001 (2001) [arXiv:hep-ph/0105041].

[53] for related studies in heavy flavor production, see: R. Bonciani, S. Catani, M. L. Mangano and P. Nason, Nucl. Phys. B **529**, 424 (1998) [Erratum-ibid. B **803**, 234 (2008)] [arXiv:hep-ph/9801375]; S. Moch and P. Uwer, Phys. Rev. D **78**, 034003 (2008) [arXiv:0804.1476 [hep-ph]]; M. Czakon and A. Mitov, arXiv:0812.0353 [hep-ph].

[54] A. Kulesza, G. Sterman and W. Vogelsang, Phys. Rev. D **66**, 014011 (2002) [arXiv:hep-ph/0202251].

[55] S. Catani, D. de Florian and M. Grazzini, JHEP **0105**, 025 (2001) [arXiv:hep-ph/0102227]; see also: M. Krämer, E. Laenen and M. Spira, Nucl. Phys. B **511**, 523 (1998) [arXiv:hep-ph/9611272]; R. V. Harlander and W. B. Kilgore, Phys. Rev. D **64**, 013015 (2001) [arXiv:hep-ph/0102241].

[56] W. K. Tung, H. L. Lai, A. Belyaev, J. Pumplin, D. Stump and C. P. Yuan, JHEP **0702**, 053 (2007) [arXiv:hep-ph/0611254].

[57] D. de Florian, R. Sassot and M. Stratmann, Phys. Rev. D **75**, 114010 (2007) [arXiv:hep-ph/0703242].

[58] T. O. Eynck, E. Laenen and L. Magnea, [arXiv:hep-ph/0305179]; E. Laenen and L. Magnea, Phys. Lett. B **632**, 270 (2006) [arXiv:hep-ph/0508284]; E. Laenen, G. Stavenga and C. D. White, JHEP **0903**, 054 (2009) [arXiv:0811.2067 [hep-ph]]; E. Laenen, L. Magnea and G. Stavenga, Phys. Lett. B **669**, 173 (2008) [arXiv:0807.4412 [hep-ph]].

[59] M. J. Tannenbaum, Nucl. Phys. A **749**, 219 (2005) [arXiv:nucl-ex/0412004].

[60] S. M. Aybat, L. J. Dixon and G. Sterman, Phys. Rev. D **74**, 074004 (2006) [arXiv:hep-ph/0607309]; Phys. Rev. Lett. **97**, 072001 (2006) [arXiv:hep-ph/0606254]; E. Gardi and L. Magnea, JHEP **0903**, 079 (2009) [arXiv:0901.1091 [hep-ph]]; T. Becher and M. Neubert, JHEP **0906**, 081 (2009) [arXiv:0903.1126 [hep-ph]].

[61] W. L. van Neerven, Nucl. Phys. B **268**, 453 (1986).

[62] K. D. Lane, Phys. Rev. D **52**, 1546 (1995) [arXiv:hep-ph/9501260].

[63] For recent work, see contribution of D.G.E. Walker in G. Brooijmans *et al.*, – New Physics Working Group," arXiv:0802.3715 [hep-ph].

[64] D. Atwood, S. Bar-Shalom, G. Eilam and A. Soni, Phys. Rept. **347**, 1 (2001) [arXiv:hep-ph/0006032].

[65] For review, see: W. Bernreuther, arXiv:0805.1333 [hep-ph].

[66] L. M. Sehgal and M. Wanninger, Phys. Lett. B **200**, 211 (1988); J. Bagger, C. Schmidt and S. King, Phys. Rev. D **37**, 1188 (1988).

[67] O. Antuñano, J. H. Kühn and G. V. Rodrigo, Phys. Rev. D **77**, 014003 (2008) [arXiv:0709.1652 [hep-ph]]; G. Rodrigo, "Axigluon signatures at hadron colliders," arXiv:0803.2992 [hep-ph].

[68] F. Halzen, P. Hoyer and C. S. Kim, Phys. Lett. B **195**, 74 (1987).

[69] R. W. Brown, K. O. Mikaelian, V. K. Cung and E. A. Paschos, e- $\rightarrow$ muon+ muon-," Phys. Lett. B **43**, 403 (1973); F. A. Berends, K. J. F. Gaemers and R. Gastmans, Nucl. Phys. B **63**, 381 (1973); S. J. Brodsky, C. E. Carlson and R. Suaya, Phys. Rev. D **14**, 2264 (1976).

[70] S. Catani, D. de Florian, G. Rodrigo and W. Vogelsang, Phys. Rev. Lett. **93**, 152003 (2004) [arXiv:hep-ph/0404240].

[71] W. Beenakker, H. Kuijf, W. L. van Neerven and J. Smith, Phys. Rev. D **40**, 54 (1989); W. Beenakker, W. L. van Neerven, R. Meng, G. A. Schuler and J. Smith, Nucl. Phys. B **351**, 507 (1991).

[72] P. Nason, S. Dawson and R. K. Ellis, Nucl. Phys. B **327**, 49 (1989) [Erratum-ibid. B **335**, 260 (1990)].

[73] J. Riedl, A. Schäfer and M. Stratmann, Eur. Phys. J. C **52**, 987 (2007) [arXiv:0708.3010 [hep-ph]].

[74] J. H. Kühn and G. Rodrigo, Phys. Rev. Lett. **81**, 49 (1998) [arXiv:hep-ph/9802268]; Phys. Rev. D **59**, 054017 (1999) [arXiv:hep-ph/9807420].

[75] M. T. Bowen, S. D. Ellis and D. Rainwater, Phys. Rev. D **73**, 014008 (2006) [arXiv:hep-ph/0509267].

[76] S. Dittmaier, P. Uwer and S. Weinzierl, Phys. Rev. Lett. **98**, 262002 (2007) [arXiv:hep-ph/0703120].

[77] V. M. Abazov *et al.* [D0 Collaboration], arXiv:0712.0851 [hep-ex].

[78] J. Weinelt, Masters thesis, Universität Karlsruhe, FERMILAB-MASTERS-2006-05; IEKP-KA-2006-21; D. Hirschbuehl, Ph.D. Thesis, Universität Karlsruhe, FERMILAB-THESIS-2005-80.

[79] E. Laenen, J. Smith and W. L. van Neerven, Phys. Lett. B **321**, 254 (1994) [arXiv:hep-ph/9310233]; S. Catani, M. L. Mangano, P. Nason and L. Trentadue, Phys. Lett. B **378**, 329 (1996) [arXiv:hep-ph/9602208]; E. L. Berger and H. Contopanagos, Phys. Rev. D **54**, 3085 (1996) [arXiv:hep-ph/9603326].

[80] R. Bonciani, S. Catani, M. L. Mangano and P. Nason, Nucl. Phys. B **529**, 424 (1998) [arXiv:hep-ph/9801375].

[81] N. Kidonakis, E. Laenen, S. Moch and R. Vogt, Phys. Rev. D **64**, 114001 (2001) [arXiv:hep-ph/0105041]; N. Kidonakis and R. Vogt, Phys. Rev. D **68**, 114014 (2003) [arXiv:hep-ph/0308222].

[82] M. Cacciari, S. Frixione, M. M. Mangano, P. Nason and G. Ridolfi, arXiv:0804.2800 [hep-ph].

[83] R. Bonciani, S. Catani, M. L. Mangano and P. Nason, Phys. Lett. B **575**, 268 (2003) [arXiv:hep-ph/0307035].

[84] J. Kodaira and L. Trentadue, Phys. Lett. B **112**, 66 (1982); Phys. Lett. B **123**, 335 (1983);
S. Catani, E. D'Emilio and L. Trentadue, Phys. Lett. B **211**, 335 (1988).

[85] S. Frixione, M. L. Mangano, P. Nason and G. Ridolfi, Nucl. Phys. B **412**, 225 (1994) [arXiv:hep-ph/9306337].

[86] M. L. Mangano, P. Nason and G. Ridolfi, Nucl. Phys. B **373**, 295 (1992).

[87] S. Catani, M. L. Mangano, P. Nason and L. Trentadue, Nucl. Phys. B **478**, 273 (1996) [arXiv:hep-ph/9604351].

[88] J. Pumplin, D. R. Stump, J. Huston, H. L. Lai, P. Nadolsky and W. K. Tung, JHEP **0207**, 012 (2002) [arXiv:hep-ph/0201195].

[89] G. Bozzi, S. Catani, D. de Florian and M. Grazzini, Phys. Lett. B **564**, 65 (2003) [arXiv:hep-ph/0302104]; D. de Florian and J. Zurita, Phys. Lett. B **659**, 813 (2008) [arXiv:0711.1916 [hep-ph]].

[90] CDF and D0 Collaborations, arXiv:hep-ex/0703034.

[91] G. Sterman and W. Vogelsang, in: *High Energy Physics 99*, Proceedings of the "International Europhysics Conference on High-Energy Physics", ed. K. Huitu *et al.* (Institute of Physics Publishing, Bristol, UK, 2000), hep-ph/9910371.

[92] see, for example: S. Catani, M. L. Mangano, P. Nason, C. Oleari and W. Vogelsang, JHEP **9903**, 025 (1999) [arXiv:hep-ph/9903436]; N. Kidonakis and J. F. Owens, Phys. Rev. D **61**, 094004 (2000) [arXiv:hep-ph/9912388]; G. Sterman and W. Vogelsang, JHEP **0102**, 016 (2001) [arXiv:hep-ph/0011289]; S. Catani, D. de Florian, M. Grazzini and P. Nason, JHEP **0307**, 028 (2003) [arXiv:hep-ph/0306211]; D. de Florian and W. Vogelsang, Phys. Rev. D **72**, 014014 (2005) [arXiv:hep-ph/0506150]; Phys. Rev. D **71**, 114004 (2005) [arXiv:hep-ph/0501258].

[93] ATLAS Detector and physics performance TDR, CERN-LHCC-99-14; CMS Physics and performance TDR, Volume II: CERN-LHCC-2006-021

[94] K. Agashe, A. Belyaev, T. Krupovnickas, G. Perez and J. Virzi, Phys. Rev. D **77**, 015003 (2008) [arXiv:hep-ph/0612015].

[95] A. L. Fitzpatrick, J. Kaplan, L. Randall and L. T. Wang, JHEP **0709**, 013 (2007) [arXiv:hep-ph/0701150].

[96] U. Baur and L. H. Orr, Phys. Rev. D **76**, 094012 (2007) [arXiv:0707.2066 [hep-ph]].

[97] G. Brooijmans, ATLAS note, ATL-PHYS-CONF-2008-008; J. Conway, *et al.*, LPC Workshop on Early Physics at CMS, UC Davis (2007); G. Brooijmans *et al.*, arXiv:0802.3715 [hep-ph]; M. Vos, talk given in the *ATLAS Flavour Tagging Meeting*, CERN (2008).

[98] D. Benchekroun, C. Driouichi, A. Hoummada, SN-ATLAS-2001-001, ATL-COM-PHYS-2000-020, EPJ Direct 3, 1 (2001); J. M. Butterworth, B. E. Cox and J. R. Forshaw, Phys. Rev. D **65**, 096014 (2002) [arXiv:hep-ph/0201098]; J. M. Butterworth, A. R. Davison, M. Rubin and G. P. Salam, arXiv:0809.2530 [hep-ph].

[99] See, for example, L. March, E. Ros and B. Salvachúa, ATL-PHYS-PUB-2006-002, ATL-COM-PHYS-2005-032; L. March, E. Ros and S.G.d.l. Hoz, ATL-COM-PHYS-2006-031, ATL-PHYS-CONF-2006-007; L. March, E. Ros, B. Salvacha, ATL-Phys-PUB-2006-002; M. Vos, ATL-PHYS-PUB-2008-000, ATL-PHYS-CONF-2008-016;

[100] U. Baur and L. H. Orr, arXiv:0803.1160 [hep-ph].

[101] Y. Bai and Z. Han, arXiv:0809.4487 [hep-ph].

[102] S. Fleming, A. H. Hoang, S. Mantry and I. W. Stewart, arXiv:0711.2079 [hep-ph]; S. Fleming, A. H. Hoang, S. Mantry and I. W. Stewart, Phys. Rev. D **77**, 074010 (2008) [arXiv:hep-ph/0703207]; A. H. Hoang and I. W. Stewart, arXiv:0808.0222 [hep-ph]. A. Jain, I. Scimemi and I. W. Stewart, Phys. Rev. D **77**, 094008 (2008) [arXiv:0801.0743 [hep-ph]].

[103] W. Skiba and D. Tucker-Smith, Phys. Rev. D **75**, 115010 (2007) [arXiv:hep-ph/0701247].

[104] B. Holdom, JHEP **0708**, 069 (2007) [arXiv:0705.1736 [hep-ph]].

[105] K. Agashe *et al.*, Phys. Rev. D **76**, 115015 (2007) [arXiv:0709.0007 [hep-ph]].

[106] F. Maltoni and T. Stelzer, JHEP **0302**, 027 (2003) [arXiv:hep-ph/0208156].

[107] T. Stelzer and W. F. Long, Comput. Phys. Commun. **81**, 357 (1994) [arXiv:hep-ph/9401258].

[108] J. Alwall *et al.*, JHEP **0709**, 028 (2007) [arXiv:0706.2334 [hep-ph]].

[109] T. Gleisberg et al., JHEP **0402** (2004) 056 [arXiv:hep-ph/0311263].

[110] J. Virzi, "ATLAS Transfer Function, https://twiki.cern.ch/twiki/bin/view/Atlas/TransferFunction."

[111] R. Frederix and F. Maltoni, arXiv:0712.2355 [hep-ph].

[112] V. Barger, T. Han and D. G. E. Walker, Phys. Rev. Lett. **100**, 031801 (2008) [arXiv:hep-ph/0612016].

[113] T. Han, R. Mahbubani, D. G. E. Walker and L. T. E. Wang, arXiv:0803.3820 [hep-ph].

[114] K. Agashe, H. Davoudiasl, G. Perez and A. Soni, Phys. Rev. D **76**, 036006 (2007) [arXiv:hep-ph/0701186]; B. Lillie, L. Randall and L. T. Wang, JHEP **0709**, 074 (2007) [arXiv:hep-ph/0701166]; B. Lillie, J. Shu and T. M. P. Tait, Phys. Rev. D **76**, 115016 (2007) [arXiv:0706.3960 [hep-ph]]; H. Davoudiasl, G. Perez and A. Soni, Phys. Lett. B **665**, 67 (2008) [arXiv:0802.0203 [hep-ph]].

[115] For a recent review see: T. Han, arXiv:0804.3178 [hep-ph].

[116] S. D. Ellis, Z. Kunszt and D. E. Soper, Phys. Rev. Lett. **69**, 3615 (1992) [arXiv:hep-ph/9208249].

[117] D. E. Kaplan, K. Rehermann, M. D. Schwartz and B. Tweedie, arXiv:0806.0848 [hep-ph].

[118] J. Thaler and L. T. Wang, JHEP **0807**, 092 (2008) [arXiv:0806.0023 [hep-ph]].

[119] F. Hubaut, E. Monnier, P. Pralavorio, K. Smolek and V. Simak, Eur. Phys. J. C **44S2**, 13 (2005) [arXiv:hep-ex/0508061].

[120] W. Bernreuther, J. P. Ma and T. Schroder, Phys. Lett. B **297**, 318 (1992); S. Choi, FERMILAB-THESIS-1999-07; K. A. Johns [D0 Collaboration], Int. J. Mod. Phys. A **16S1A** (2001) 366; W. Bernreuther, A. Brandenburg, Z. G. Si and P. Uwer, Phys. Lett. B **509**, 53 (2001) [arXiv:hep-ph/0104096]; B. Abbott *et al.* [D0 Collaboration], Phys. Rev. Lett. **85**, 256 (2000) [arXiv:hep-ex/0002058]; T. Torma, JHEP **0111**, 055 (2001) [arXiv:hep-ph/9912281]; V. D. Barger, J. Ohnemus and R. J. N. Phillips, Int. J. Mod. Phys. A **4**, 617 (1989); G. L. Kane, G. A. Ladinsky and C. P. Yuan, Phys. Rev. D **45**, 124 (1992); G. Mahlon and S. J. Parke, Phys. Rev. D **53**, 4886 (1996) [arXiv:hep-ph/9512264]; D. Atwood, A. Aeppli and A. Soni, Phys. Rev. Lett. **69**, 2754 (1992); D. Atwood, S. Bar-Shalom, G. Eilam and A. Soni, Phys. Rept. **347**, 1 (2001) [arXiv:hep-ph/0006032]; M. Arai, N. Okada, K. Smolek and V. Simak, Phys. Rev. D **70**, 115015 (2004) [arXiv:hep-ph/0409273]; C. Csaki, J. Heinonen and M. Perelstein, JHEP **0710**, 107 (2007) [arXiv:0707.0014 [hep-ph]]; M. M. Nojiri and M. Takeuchi, arXiv:0802.4142 [hep-ph].

[121] T. Sjostrand, S. Mrenna and P. Skands, JHEP **0605**, 026 (2006) [arXiv:hep-ph/0603175].

[122] G. P. Salam and G. Soyez, JHEP **0705**, 086 (2007) [arXiv:0704.0292 [hep-ph]].

[123] J.E. Huth *et al.*, *Proceedings of Research Directions For The Decade: Snowmass Accord 1990.*

[124] J. Pumplin, A. Belyaev, J. Huston, D. Stump and W. K. Tung, JHEP **0602**, 032 (2006) [arXiv:hep-ph/0512167]; J. Campbell and R. K. Ellis, "MCFM, A Monte Carlo for FeMtobarn processes at Hadron Colliders, http://mcfm.fnal.gov."

[125] T. Sjostrand, S. Mrenna and P. Skands, Comput. Phys. Commun. **178**, 852 (2008) [arXiv:0710.3820 [hep-ph]].

[126] J. Alwall *et al.*, Eur. Phys. J. C **53**, 473 (2008) [arXiv:0706.2569 [hep-ph]].

[127] M. L. Mangano, M. Moretti, F. Piccinini, R. Pittau and A. D. Polosa, JHEP **0307**, 001 (2003) [arXiv:hep-ph/0206293].

[128] S. Catani, F. Krauss, R. Kuhn and B. R. Webber, JHEP **0111**, 063 (2001) [arXiv:hep-ph/0109231].

[129] S. D. Ellis, J. Huston, K. Hatakeyama, P. Loch and M. Tonnesmann, Prog. Part. Nucl. Phys. **60**, 484 (2008) [arXiv:0712.2447 [hep-ph]]; A. Banfi, G. P. Salam and G. Zanderighi, JHEP **0707**, 026 (2007) [arXiv:0704.2999 [hep-ph]].

[130] C. F. Berger, T. Kucs and G. Sterman, Phys. Rev. D **68**, 014012 (2003) [arXiv:hep-ph/0303051].

[131] G. Sterman, arXiv:hep-ph/0412013; I. M. Dremin, AIP Conf. Proc. **828**, 30 (2006) [arXiv:hep-ph/0510250]; T. Han, arXiv:hep-ph/0508097; G. Sterman, arXiv:hep-ph/9606312.

[132] P. Meade and L. Randall, arXiv:0708.3017 [hep-ph].

[133] A. Czarnecki and K. Melnikov, Nucl. Phys. B **544**, 520 (1999) [arXiv:hep-ph/9806244].

[134] K. G. Chetyrkin, R. Harlander, T. Seidensticker and M. Steinhauser, Phys. Rev. D **60**, 114015 (1999) [arXiv:hep-ph/9906273].

[135] C. Amsler *et al.* [Particle Data Group], Phys. Lett. B **667** (2008) 1, `http://www-pdg.lbl.gov/2008/reviews/statrpp.pdf`.

[136] M. Strassler, "Unusual Physics Signatures at the LHC," talk presented at the 2007 Phenomenology Symposium - Pheno 07, University of Wisconsin, Madison, May 7-9, 2007.

[137] L. Randall and R. Sundrum, Phys. Rev. Lett. **83**, 3370 (1999) [arXiv:hep-ph/9905221].

[138] M. Furman, Nucl. Phys. B **197**, 413 (1982).

[139] F. Aversa, P. Chiappetta, M. Greco and J. P. Guillet, Nucl. Phys. B **327**, 105 (1989), Z. Phys. C **46**, 253 (1990).

[140] N. Kidonakis and J. F. Owens, Phys. Rev. D **63**, 054019 (2001) [arXiv:hep-ph/0007268].

[141] M. H. Seymour, Nucl. Phys. B **513**, 269 (1998) [arXiv:hep-ph/9707338]; S. D. Ellis, J. Huston, K. Hatakeyama, P. Loch and M. Tonnesmann, Prog. Part. Nucl. Phys. **60**, 484 (2008) [arXiv:0712.2447 [hep-ph]].

[142] S. Catani, Y. L. Dokshitzer, M. Olsson, G. Turnock and B. R. Webber, Phys. Lett. B **269**, 432 (1991); S. Catani, Y. L. Dokshitzer, M. H. Seymour and B. R. Webber, Nucl. Phys. B **406**, 187 (1993); S. D. Ellis

and D. E. Soper, Phys. Rev. D **48**, 3160 (1993) [arXiv:hep-ph/9305266]; Y. L. Dokshitzer, G. D. Leder, S. Moretti and B. R. Webber, JHEP **9708**, 001 (1997) [arXiv:hep-ph/9707323].

[143] G. P. Salam and G. Soyez, JHEP **0705**, 086 (2007) [arXiv:0704.0292 [hep-ph]].

[144] For recent studies see *e.g*: K. Agashe *et al.*, Phys. Rev. D **77**, 015003 (2008) [arXiv:hep-ph/0612015]; B. Lillie, L. Randall and L. T. Wang, JHEP **0709**, 074 (2007) [arXiv:hep-ph/0701166].

[145] See *e.g*: K. Agashe *et al.*, Phys. Rev. D **76**, 115015 (2007) [arXiv:0709.0007 [hep-ph]]; K. Agashe, H. Davoudiasl, G. Perez and A. Soni, Phys. Rev. D **76**, 036006 (2007) [arXiv:hep-ph/0701186]; J. Hirn, A. Martin and V. Sanz, JHEP **0805**, 084 (2008) [arXiv:0712.3783 [hep-ph]].

[146] D. Benchekroun, C. Driouichi, A. Hoummada, SN-ATLAS-2001-001, ATL-COM-PHYS-2000-020, EPJ Direct 3, 1 (2001); J. Conway, *et al.*, LPC Workshop on Early Physics at CMS, UC Davis (2007); G. Brooijmans *et al.*, arXiv:0802.3715 [hep-ph]; M. Vos, talk given in the *ATLAS Flavour Tagging Meeting*, CERN (2008).

[147] G. Brooijmans, ATLAS note, ATL-PHYS-CONF-2008-008.

[148] J. M. Butterworth, B. E. Cox and J. R. Forshaw, Phys. Rev. D **65**, 096014 (2002) [arXiv:hep-ph/0201098].

[149] M. Cacciari, G. P. Salam and G. Soyez, JHEP **0804**, 063 (2008) [arXiv:0802.1189 [hep-ph]].

[150] G. Sterman, Phys. Rev. D **19**, 3135 (1979).

[151] N. Kidonakis, G. Oderda and G. Sterman, Nucl. Phys. B **525**, 299 (1998) [arXiv:hep-ph/9801268]; D. de Florian and W. Vogelsang, Phys. Rev. D **76**, 074031 (2007) [arXiv:0704.1677 [hep-ph]].

[152] M. Dasgupta and G. P. Salam, J. Phys. G **30**, R143 (2004) [arXiv:hep-ph/0312283]; C. F. Berger, Mod. Phys. Lett. A **20**, 1187 (2005) [arXiv:hep-ph/0505037]; M. Dasgupta, L. Magnea and G. P. Salam, JHEP **0802**, 055 (2008) [arXiv:0712.3014 [hep-ph]].

[153] D. E. Kaplan, K. Rehermann, M. D. Schwartz and B. Tweedie, arXiv:0806.0848 [hep-ph].

[154] J. Thaler and L. T. Wang, arXiv:0806.0023 [hep-ph].

[155] C. F. Berger, T. Kucs and G. Sterman, Phys. Rev. D **68**, 014012 (2003) [arXiv:hep-ph/0303051].

[156] J. M. Butterworth, A. R. Davison, M. Rubin and G. P. Salam, arXiv:0802.2470 [hep-ph].

[157] G. Parisi, Phys. Lett. B **74**, 65 (1978).

[158] J. F. Donoghue, F. E. Low and S. Y. Pi, Phys. Rev. D **20**, 2759 (1979).

[159] R. K. Ellis, D. A. Ross and A. E. Terrano, Nucl. Phys. B **178**, 421 (1981).

[160] A. Banfi, Y. L. Dokshitzer, G. Marchesini and G. Zanderighi, JHEP **0105**, 040 (2001) [arXiv:hep-ph/0104162].

[161] F. Maltoni and T. Stelzer, JHEP **0302**, 027 (2003) [arXiv:hep-ph/0208156]; T. Stelzer and W. F. Long, Comput. Phys. Commun. **81**, 357 (1994) [arXiv:hep-ph/9401258], JHEP **0709**, 028 (2007) [arXiv:0706.2334 [hep-ph]].

[162] T. Gleisberg et al., JHEP **0402** (2004) 056 [arXiv:hep-ph/0311263].

[163] C. F. Berger and L. Magnea, Phys. Rev. D **70**, 094010 (2004) [arXiv:hep-ph/0407024].

Appendix A: NLO Dihadron cross-section

In this appendix we present some details for the calculation of the NLO partonic cross-sections near threshold. The virtual corrections have the $2 \to 2$ kinematics of the Born terms and therefore fully contribute. They are proportional to $\delta(1-\hat{\tau})$. The real-emission $2 \to 3$ contributions require more effort. We consider the reaction $a(p_1) + b(p_2) \to c(k_1) + d(k_2) + e(k_3)$, where partons d and e fragment into the observed pair of hadrons and have pair mass $\hat{m}^2$. It is convenient to work in the c.m.s. of the observed outgoing hadrons. We can then write the three-body phase space in $4-2\varepsilon$ dimensions as

$$\begin{aligned}\Phi_3 &= \frac{s}{(4\pi)^4\Gamma(1-2\varepsilon)}\left(\frac{4\pi}{s}\right)^{2\varepsilon}\int_0^1 d\hat{\tau}\hat{\tau}^{-\varepsilon}(1-\hat{\tau})^{1-2\varepsilon}\int_0^\infty d\rho\rho^{-\varepsilon}(1+\rho)^{-2+2\varepsilon} \\ &\quad\times\int_0^\pi d\psi\sin^{1-2\varepsilon}\psi\int_0^\pi d\theta\,\sin^{-2\varepsilon}\theta\,. \qquad \text{(A.1)}\end{aligned}$$

Here we define

$$\rho = (p_1-k_2)^2/(p_2-k_2)^2 = \mathrm{e}^{-2\Delta\eta}\,. \qquad \text{(A.2)}$$

Near threshold, the integration variables are given in terms of the Mandelstam variables of the process as follows:

$$
\begin{aligned}
&(p_1+p_2)^2=\hat{s}\;,\quad (k_2+k_3)^2=\hat{m}^2=\hat{\tau}\hat{s}\;,\\
&(p_1-k_1)^2=-\frac{\hat{s}(1-\hat{\tau})}{2}(1-\cos\psi)\;,\quad (p_2-k_1)^2=-\frac{\hat{s}(1-\hat{\tau})}{2}(1+\cos\psi)\;,\\
&(p_1-k_2)^2=-\frac{\hat{s}\rho}{1+\rho}=(p_2-k_3)^2\;,\quad (p_2-k_2)^2=-\frac{\hat{s}}{1+\rho}=(p_1-k_3)^2\;,\\
&(k_1+k_2)^2=\frac{\hat{s}(1-\hat{\tau})}{2}\left(1+\sin\psi\cos\theta\,\frac{2\sqrt{\rho}}{1+\rho}-\cos\psi\,\frac{1-\rho}{1+\rho}\right)\;,\\
&(k_1+k_3)^2=\frac{\hat{s}(1-\hat{\tau})}{2}\left(1-\sin\psi\cos\theta\,\frac{2\sqrt{\rho}}{1+\rho}+\cos\psi\,\frac{1-\rho}{1+\rho}\right)\;.
\end{aligned}
\tag{A.3}
$$

The phase space in Eq. (A.1) is used to integrate the squared $2\to 3$ matrix elements $|\mathcal{M}_{ab\to cde}|^2$. For the latter one also assumes near-threshold kinematics. Since we want the partonic cross section at fixed $\hat{\tau}$ and $\Delta\eta$, we only need to perform the last two integrations in Eq. (A.1). The basic integral for these is [61]

$$
\begin{aligned}
&\int_0^\pi d\psi\int_0^\pi d\theta\,\frac{\sin^{1-2\varepsilon}\psi\sin^{-2\varepsilon}\theta}{(1-\cos\psi)^j(1-\cos\psi\cos\chi-\sin\psi\cos\theta\sin\chi)^k}\\
&\quad=2\pi\frac{\Gamma(1-2\varepsilon)}{\Gamma(1-\varepsilon)^2}\,2^{-j-k}\,B(1-\varepsilon-j,1-\varepsilon-k)\\
&\qquad\times\,{}_2F_1\left(j,k,1-\varepsilon,\cos^2\frac{\chi}{2}\right)\;,
\end{aligned}
\tag{A.4}
$$

where ${}_2F_1$ is the Hypergeometric function. After integration over phase space and addition of the virtual corrections, infrared singularities cancel and only collinear singularities remain. These are removed by mass factorization, which we do in the $\overline{\rm MS}$ scheme. Notice that since we are close to threshold only the diagonal splitting functions $P_{ii}^{(1)}$ contribute in this procedure. Combining all contributions, one arrives at the near-threshold structure of the partonic cross sections given in Eq. (3.17), for each subprocess that is already present at LO. The final step is to take Mellin moments in $\hat{\tau}$ of the result, as described in

Eq. (3.26). This gives for the partonic cross sections to NLO:

$$\begin{aligned}\tilde{\omega}^{\mathrm{thr,LO+NLO}}_{ab\to cd}\left(N,\Delta\eta,\alpha_s(\mu),\mu/\hat{m}\right) &= \omega^{(0)}_{ab\to cd}(\Delta\eta) \\ &+\frac{\alpha_s(\mu)}{\pi}\left[\omega^{(1,0)}_{ab\to cd}(\Delta\eta,\mu/\hat{m}) - \ln\bar{N}\;\omega^{(1,1)}_{ab\to cd}(\Delta\eta,\mu/\hat{m})\right. \\ &\left.+\frac{1}{2}\left(\ln^2\bar{N}+\zeta(2)\right)\;\omega^{(1,2)}_{ab\to cd}(\Delta\eta)\right]\,, \end{aligned} \tag{A.5}$$

where terms subleading in N have been neglected. The "C-coefficients" defined in Eq. (3.41) are obtained from this as

$$C^{(1)}_{ab\to cd}\left(\Delta\eta,\mu/\hat{m}\right) = \frac{\omega^{(1,0)}_{ab\to cd}(\Delta\eta,\mu/\hat{m}) + \frac{1}{2}\zeta(2)\,\omega^{(1,2)}_{ab\to cd}(\Delta\eta)}{\omega^{(0)}_{ab\to cd}(\Delta\eta)}\,. \tag{A.6}$$

Appendix B: Hard Coefficients

In this section we give the coefficients $C^{(1)}_{ab\to cd}$ for each subprocess contributing to the production of our di-hadron final state, resulting from the calculation outlined in Appendix A. In all expressions below, μ is the renormalization scale. The dependence on the factorization scale is already included in the function $\mathcal{E}_i$ in Eq. (3.43). As before, we define $\rho \equiv \mathrm{e}^{-2\Delta\eta}$.

$\underline{qq' \to qq'}$:

We define:

$$Q_{qq'} \equiv 1 + (1+\rho)^2 \,. \tag{B.1}$$

We then have:

$$\begin{aligned} C^{(1)}_{qq'\to qq'}(\Delta\eta, \mu/\hat{m}) \;=\; & 2\pi b_0 \ln\frac{\mu^2}{\hat{m}^2} + \left(\frac{5}{6Q_{qq'}} + \frac{13}{12}\right)\ln^2\rho \\ & + \left(\frac{5}{6} - \frac{1}{3Q_{qq'}}\right)\ln^2(1+\rho) + \left(-\frac{8}{3} + \frac{14+9\rho}{6Q_{qq'}}\right)\ln\rho \\ & + \left(-\frac{4}{3} + \frac{2}{3Q_{qq'}}\right)\ln(1+\rho)\ln\rho - \frac{\rho}{3Q_{qq'}}\ln(1+\rho) \\ & + \frac{7\pi^2}{6Q_{qq'}} + \frac{N_f}{3}\ln\frac{\rho}{1+\rho} - \frac{5N_f}{9} + \frac{8}{3}\mathrm{Li}_2\left(\frac{\rho}{1+\rho}\right) \\ & + \frac{3}{2}\ln(1+\rho) + \frac{47\pi^2}{36} + \frac{7}{2}\,. \end{aligned} \tag{B.2}$$

$\underline{q\bar{q}' \to q\bar{q}'}$:

We have:

$$\begin{aligned} C^{(1)}_{q\bar{q}'\to q\bar{q}'}(\Delta\eta,\mu/\hat{m}) &= C^{(1)}_{qq'\to qq'}(\Delta\eta,\mu/\hat{m}) \\ &+\frac{5}{6}\left\{\left(1-\frac{2}{Q_{qq'}}\right)\left[(1+\ln\rho)\ln\rho+\frac{\pi^2}{2}\right]-\frac{\rho}{Q_{qq'}}\ln(1+\rho)\right. \\ &\left.+\left(\frac{3}{2}-\frac{1}{Q_{qq'}}\right)\ln(1+\rho)\ln\frac{1+\rho}{\rho^2}-2\mathrm{Li}_2\left(\frac{\rho}{1+\rho}\right)\right\}\ . \end{aligned} \tag{B.3}$$

<u>$qq\to qq$:</u>

We define:

$$Q_{qq}\equiv\frac{(1-\rho+\rho^2)(3+5\rho+3\rho^2)}{(1+\rho(1+\rho))}\ . \tag{B.4}$$

We then have:

$$\begin{aligned} C^{(1)}_{qq\to qq}(\Delta\eta,\mu/\hat{m}) &= 2\pi b_0\ln\frac{\mu^2}{\hat{m}^2}+\frac{8}{Q_{qq}}\left(1-\rho^2\right)\mathrm{Li}_2\left(\frac{\rho}{1+\rho}\right) \\ &+\left(\frac{7}{6}-\frac{59\rho}{48Q_{qq}}+\frac{5}{4\ Q_{qq}}-\frac{\rho+4}{16\left(3+5\rho+3\rho^2\right)}\right)\ln^2\rho \\ &-\frac{(12\rho^2+3\rho-4)}{2Q_{qq}}\ln^2(1+\rho)+\frac{\ln\rho}{12Q_{qq}}\left(37\rho-71+\frac{(17-8\rho)\,Q_{qq}}{3+5\rho+3\rho^2}\right) \\ &+\left(\frac{7}{3}-\frac{7}{4Q_{qq}}\left(6-5\rho\right)-\frac{53\rho-6}{12\left(3+5\rho+3\rho^2\right)}\right)\ln(1+\rho)\ln\rho \\ &+\left(\frac{3}{2}-\frac{\rho}{4Q_{qq}}-\frac{\rho}{4\left(3+5\rho+3\rho^2\right)}\right)\ln(1+\rho) \\ &+N_f\left(\frac{2-\rho}{2Q_{qq}}+\frac{\rho}{3\left(3+5\rho+3\rho^2\right)}\right)\ln\rho-\frac{1}{3}N_f\ln(1+\rho)-\frac{5N_f}{9} \\ &+\frac{7}{2}\left(1+\frac{2}{3}\pi^2\right)-\frac{\pi^2}{3Q_{qq}}\left(4+\frac{41}{16}\rho\right)-\frac{71\pi^2\rho}{144\left(3+5\rho+3\rho^2\right)}\ . \end{aligned} \tag{B.5}$$

<u>$q\bar{q}\to q'\bar{q}'$:</u>

We define:

$$Q_{q'\bar{q}'}\equiv 1+\rho^2\ . \tag{B.6}$$

We then have:

$$
\begin{aligned}
C^{(1)}_{q\bar{q}\to q'\bar{q}'}\left(\Delta\eta,\mu/\hat{m}\right) &= 2\pi b_0 \ln\frac{\mu^2}{\hat{m}^2} + \frac{7}{4}\left(1-\frac{2}{3Q_{q'\bar{q}'}}\right)\ln^2\rho \\
&\quad -\frac{5}{12}\left(1+\frac{2}{Q_{q'\bar{q}'}}\right)\ln^2(1+\rho) + \frac{7(1+\rho)}{6Q_{q'\bar{q}'}}\ln\rho \\
&\quad -\frac{7}{6}\left(1-\frac{2}{Q_{q'\bar{q}'}}\right)\ln(1+\rho)\ln\rho - \frac{1}{3}\left(1+\frac{5+9\rho}{2Q_{q'\bar{q}'}}\right)\ln(1+\rho) \\
&\quad -\frac{5N_f}{9} - \frac{5}{3}\mathrm{Li}_2\left(\frac{\rho}{1+\rho}\right) + \frac{1}{6}\left(21+4\pi^2\right) \ . \qquad \text{(B.7)}
\end{aligned}
$$

<u>$q\bar{q}\to q\bar{q}$:</u>

We define:

$$
\begin{aligned}
Q^{(1)}_{q\bar{q}} &\equiv 3+\rho(1+\rho) \ , \\
Q^{(2)}_{q\bar{q}} &\equiv 1+3\rho(1+\rho) \ . \qquad \text{(B.8)}
\end{aligned}
$$

We then have:

$$
\begin{aligned}
C^{(1)}_{q\bar{q}\to q\bar{q}}(\Delta\eta,\mu/\hat{m}) &= 2\pi b_0 \ln\frac{\mu^2}{\hat{m}^2} \\
&+N_f\left(\frac{1}{6}+(1+2\rho)\left(\frac{1}{8Q^{(1)}_{q\bar{q}}}+\frac{1}{8Q^{(2)}_{q\bar{q}}}\right)\right)\ln\left(\frac{\rho}{1+\rho}\right) \\
&+\mathrm{Li}_2\left(\frac{\rho}{1+\rho}\right)\left(\frac{5+4\rho}{2Q^{(1)}_{q\bar{q}}}+\frac{1+4\rho}{2Q^{(2)}_{q\bar{q}}}-\frac{1}{3}\right) \\
&+\pi^2\left(\frac{5(9+14\rho)}{96Q^{(1)}_{q\bar{q}}}+\frac{155+282\rho}{288Q^{(2)}_{q\bar{q}}}+\frac{43}{36}\right) \\
&+\left(\frac{4\rho-79}{64Q^{(1)}_{q\bar{q}}}+\frac{61+180\rho}{576Q^{(2)}_{q\bar{q}}}+\frac{65}{36}\right)\ln^2\rho \\
&+\left(\frac{13+124\rho}{64Q^{(1)}_{q\bar{q}}}+\frac{361+972\rho}{576Q^{(2)}_{q\bar{q}}}+\frac{29}{36}\right)\ln^2(1+\rho) \\
&+\left(\frac{7-\rho}{16Q^{(1)}_{q\bar{q}}}-\frac{35+71\rho}{48Q^{(2)}_{q\bar{q}}}-\frac{11}{12}\right)\ln\rho \\
&+\left(\frac{61-64\rho}{32Q^{(1)}_{q\bar{q}}}-\frac{247+576\rho}{288Q^{(2)}_{q\bar{q}}}-\frac{22}{9}\right)\ln(1+\rho)\ln\rho \\
&+\left(\frac{8+\rho}{16Q^{(1)}_{q\bar{q}}}+\frac{36+71\rho}{48Q^{(2)}_{q\bar{q}}}+\frac{7}{12}\right)\ln(1+\rho)-\frac{5N_f}{9}+\frac{7}{2}\,. \qquad \text{(B.9)}
\end{aligned}
$$

$\underline{q\bar{q}\to gg}$:

We define:

$$G_{q\bar{q}} \equiv (1+\rho^2)(4-\rho+4\rho^2)\,. \qquad \text{(B.10)}$$

We then have:

$$
\begin{aligned}
C^{(1)}_{q\bar{q}\to gg}\left(\Delta\eta, \mu/\hat{m}\right) &= 2\pi b_0 \ln\frac{\mu^2}{\hat{m}^2} - \frac{27}{2G_{q\bar{q}}}\left(1-\rho^4\right)\mathrm{Li}_2\left(\frac{\rho}{1+\rho}\right) \\
&+\frac{1}{48}\left(1+\frac{2\rho}{G_{q\bar{q}}}\left(133+13\rho\right)+\frac{124-311\rho}{4-\rho+4\rho^2}\right)\ln^2\rho \\
&+\frac{1}{48}\left(69+\frac{52\rho^2}{G_{q\bar{q}}}-\frac{\rho+648}{4-\rho+4\rho^2}\right)\ln^2(1+\rho) \\
&+\frac{1}{6}\left(-\frac{\rho}{G_{q\bar{q}}}\left(3+89\rho\right)+\frac{48+5\rho}{4-\rho+4\rho^2}\right)\ln\rho \\
&+\left(\frac{89\rho^2}{3G_{q\bar{q}}}-\frac{19\rho}{6\left(4-\rho+4\rho^2\right)}-2\right)\ln(1+\rho) \\
&+\frac{1}{24}\left(-19-\frac{2\rho}{G_{q\bar{q}}}\left(133+13\rho\right)+\frac{200+149\rho}{4-\rho+4\rho^2}\right)\ln\rho\ln(1+\rho) \\
&-\frac{15}{4G_{q\bar{q}}}\rho(1-\rho)^2+\frac{9\pi^2(4-\rho)}{16\left(4-\rho+4\rho^2\right)}+\frac{191\pi^2}{144}-\frac{14}{3}\,. \qquad \text{(B.11)}
\end{aligned}
$$

$\underline{qg\to qg}$:

We define:

$$
\begin{aligned}
Q^{(1)}_{qg} &\equiv 2(1+\rho)+\rho^2\,, \\
Q^{(2)}_{qg} &\equiv 9(1+\rho)+4\rho^2\,. \qquad \text{(B.12)}
\end{aligned}
$$

We then have:

$$
\begin{aligned}
C^{(1)}_{qg\to qg}(\Delta\eta,\mu/\hat{m}) &= 2\pi b_0 \ln\frac{\mu^2}{\hat{m}^2} - \frac{14}{3} + \frac{15(1+\rho)(2+\rho)^2}{4Q^{(1)}_{qg}Q^{(2)}_{qg}} \\
&+\pi^2\left(\frac{146+13\rho}{24Q^{(1)}_{qg}} - \frac{3(109+13\rho)}{16Q^{(2)}_{qg}} + \frac{241}{144}\right) \\
&+\left((1+\rho)\left(\frac{13}{12Q^{(1)}_{qg}} - \frac{15}{16Q^{(2)}_{qg}}\right) + \frac{17}{16}\right)\ln^2\rho \\
&+(1+\rho)\left(\frac{89}{3Q^{(1)}_{qg}} - \frac{231}{2Q^{(2)}_{qg}}\right)\ln\rho + \left(\frac{31}{24} + \frac{27(\rho-3)}{8Q^{(2)}_{qg}}\right)\mathrm{Li}_2\left(\frac{\rho}{1+\rho}\right) \\
&+\left(\frac{13\rho-120}{24Q^{(1)}_{qg}} + \frac{3(173+41\rho)}{16Q^{(2)}_{qg}} - \frac{27}{16}\right)\ln^2(1+\rho) \\
&+\left(-\frac{86+89\rho}{6Q^{(1)}_{qg}} + \frac{3(43+39\rho)}{2Q^{(2)}_{qg}} - 2\right)\ln(1+\rho) \\
&+\left(\frac{120-13\rho}{12Q^{(1)}_{qg}} - \frac{3(155+23\rho)}{8Q^{(2)}_{qg}} + \frac{31}{24}\right)\ln\rho\ln(1+\rho)\,. \qquad \text{(B.13)}
\end{aligned}
$$

<u>$gg \to q\bar{q}$:</u>

We have:

$$
C^{(1)}_{gg\to q\bar{q}}(\Delta\eta,\mu/\hat{m}) = C^{(1)}_{q\bar{q}\to gg}(\Delta\eta,\mu/\hat{m})\,. \qquad \text{(B.14)}
$$

<u>$gg \to gg$:</u>

We define:

$$
G_{gg} \equiv 1+\rho(1+\rho)\,. \qquad \text{(B.15)}
$$

We then have:

$$
\begin{aligned}
C^{(1)}_{gg\to gg}(\Delta\eta,\mu/\hat{m}) &= 2\pi b_0 \ln\frac{\mu^2}{\hat{m}^2} \\
&+N_f\left(\frac{5}{9}+\frac{3\rho^2(1+\rho)^2}{8G_{gg}^3}+\frac{\pi^2\rho\,(1+\rho^2)\,(1+\rho)^2}{16\;G_{gg}^3}\right) \\
&-\frac{3\rho^2(1+\rho)^2}{8\;G_{gg}^3}(3+\pi^2)+\frac{3}{4}\left(\frac{(1+\rho)^3}{G_{gg}^3}+1\right)\ln^2\rho \\
&+\frac{N_f}{16G_{gg}^2}(1+\rho)\left(\frac{2}{G_{gg}}(1+\rho)^2+\rho^2-2(1+\rho)\right)\ln^2\rho \\
&+\frac{N_f}{24G_{gg}^2}\left(8\left(1+\rho^2\right)+5\rho\right)(1+\rho)^2\ln(1+\rho) \\
&+\frac{N_f}{16G_{gg}^2}(1+\rho)^2\left(\frac{2}{G_{gg}}(1+\rho)-2-\rho\right)\ln^2(1+\rho) \\
&+\frac{N_f}{8G_{gg}^2}(1+\rho)\left(2\rho+1-\frac{1}{G_{gg}}(1+\rho)^2\right)\ln\rho\ln(1+\rho) \\
&+\frac{1}{G_{gg}^2}\left(-\frac{11}{2}\left(1+\rho^2\right)-\frac{7}{4}\rho\right)(1+\rho)^2\ln(1+\rho) \\
&+\frac{3\pi^2(1+\rho)}{4\;G_{gg}^2}+\left(\frac{3}{2}-\frac{3(1+\rho)^3}{4G_{gg}^3}+\frac{3(2\rho+1)\,(1+\rho^2)}{4G_{gg}^2}\right)\ln\rho\ln(1+\rho) \\
&+\frac{1}{G_{gg}^2}\left(\frac{7}{4}\rho^2+\frac{11}{2}(1+\rho)\right)(1+\rho)\ln\rho-\frac{N_f}{24G_{gg}^2}(1+\rho)\left(5\rho^2+8(1+\rho)\right)\ln\rho \\
&+\left(\frac{3(1+\rho)^3}{4\;G_{gg}^3}-\frac{3(2\rho+1)}{4G_{gg}^2}-\frac{3\;(1+\rho)}{2G_{gg}}-\frac{3}{4}\right)\ln^2(1+\rho) \\
&-\frac{3}{2G_{gg}}\left(1-\rho^2\right)\;\mathrm{Li}_2\left(\frac{\rho}{1+\rho}\right)-\frac{\pi^2(1+\rho)}{2G_{gg}}+\frac{11\pi^2}{4}-\frac{67}{6}\;. \qquad \text{(B.16)}
\end{aligned}
$$

Appendix C: Jets at Fixed Invariant Mass

Here we give details of the definitions and calculations for the jet functions that we employ in section 3. Single inclusive Jet cross sections have been studied intensively [129, 138–140]. Here, we are interested in computing the QCD background to jets of measured mass. The main background to the production of $t\bar{t}$ pairs is from dijet production from hadronic collisions,

$$H_a(p_a) + H_b(p_b) \to J_1(m^2_{J_1}, p_{1,T}, \eta_1, R) + J_2(m^2_{J_2}, p_{2,T}, \eta_2, R) + X, \qquad \text{(C.1)}$$

where the final states are jets in the directions of the outgoing partons, each with a fixed jet mass m^2_J , a "cone size" $R^2 = \Delta\eta^2 + \Delta\phi^2$, and transverse momenta, $p_{i,T}$. For simplicity we choose the cone sizes equal for the two jets, although they can be different. For $R < 1$, we can isolate the leading (R^0) dependence of such cross-sections in factorized "jet" functions,

$$\begin{aligned}\frac{d\sigma_{H_A H_B \to J_1 J_2}}{dp_T dm^2_{J_1} dm^2_{J_2} d\eta_1 d\eta_2} &= \sum_{abcd} \int dx_a\, dx_b\, \phi_a(x_a)\, \phi_b(x_b) \\ &\times H_{ab\to cd}\left(x_a, x_b, p_T, \eta_1, \eta_2, \alpha_s(p_T)\right) \\ &\times J_1^c(m^2_{J_1}, p_T \cosh\eta_1, R, \alpha_s(p_T))\; J_2^d(m^2_{J_2}, p_T \cosh\eta_2, R, \alpha_s(p_T)), \qquad \text{(C.2)}\end{aligned}$$

with corrections that vanish as powers of R. Here the ϕ's are parton distribution functions for the initial hadrons, $H_{ab\to cd}$ is a perturbative $2 \to 2$ QCD hard-scattering function, equal to the dijet Born cross section at lowest order, and the J_i are jet functions, which are defined below. Jet function J_i summarizes the formation of a set of final state particles with fixed invariant mass and momenta collinear to the i^{th} outgoing parton. Corrections to the cross section of order R^0 can only occur through collinear enhancements which factorize into these functions [21].

Following Ref. [155] we define jet function for quarks at fixed jet mass by

$$\begin{aligned} J_i^q(m_J^2, p_{0,J_i}, R) &= \frac{(2\pi)^3}{2\sqrt{2}\,(p_{0,J_i})^2}\frac{\xi_\mu}{N_c} \\ &\times \sum_{N_{J_i}} \mathrm{Tr}\left\{\gamma^\mu \,\langle\, 0|q(0)\Phi_\xi^{(\bar{q})\dagger}(\infty,0)|N_{J_i}\,\rangle\,\langle\, N_{J_i}|\Phi_\xi^{(\bar{q})}(\infty,0)\bar{q}(0)|0\,\rangle\right\} \\ &\times\delta\left(m_J^2-\tilde{m}_J^2(N_{J_i},R)\right)\delta^{(2)}(\hat{n}-\tilde{n}(N_{J_i}))\delta(p_{0,J_i}-\omega(N_{J_c})), \quad \text{(C.3)} \end{aligned}$$

where $\tilde{m}_J^2(N_{J_i}, R)$ is the invariant mass of all particles within the cone centered on direction $\hat{n}$ in state N_{J_i}. Correspondingly, gluon jet functions are defined by

$$\begin{aligned} J_i^g(m_J^2, p_{0,J_i}, R) &= \frac{(2\pi)^3}{2(p_{0,J_i})^3}\sum_{N_{J_i}} \langle\, 0|\xi_\sigma F^{\sigma\nu}(0)\Phi_\xi^{(g)\dagger}\,(0,\infty)\,|N_{J_i}\,\rangle \\ &\times \langle\, N_{J_i}|\Phi_\xi^{(g)}\,(0,\infty)\,F_\nu^\rho(0)\xi_\rho|0\,\rangle \\ &\times\delta\left(m_J^2-\tilde{m}_J^2(N_{J_i},R)\right)\delta^{(2)}(\hat{n}-\tilde{n}(N_{J_i}))\delta(p_{0,J_i}-\omega(N_{J_c})). \quad \text{(C.4)} \end{aligned}$$

These functions absorb collinear enhancements to the outgoing particles that emerge from the underlying hard perturbative process and fragment into the observed jets. The Φ's are path ordered exponentials (Wilson lines) defined by

$$\Phi_\xi^{(f)}(\infty,0;0) = \mathcal{P}\left\{e^{-ig\int_0^\infty d\eta\,\xi\cdot A^{(f)}(\eta\,\xi^\mu)}\right\}, \quad \text{(C.5)}$$

where $\mathcal{P}$ indicates ordering along the integral and where ξ is a direction with at least one component in the direction opposite to the jet. The full hadronic cross-section is independent of the choice for ξ. As indicated, the gauge field $A^{(f)}$ is a matrix in the representation of the generators for parton f. In general the jet function depends on $\vec{\xi}\cdot\hat{n}$, but for simplicity we suppress this dependence below. Finally the jet functions in Eqs. (C.3) and (C.4) are normalized such that at lowest order we have

$$J_i^{(0)}(m_{J_i}^2, p_{0,J_i}, R) = \delta(m_{J_i}^2). \quad \text{(C.6)}$$

C.0.1 Jet Functions at Next-to-Leading Order

At next-to-leading order, contributions to the jet mass distributions for light quark or gluon jets have only two particles in their final states. For the quark

jet we have the following matrix element which has to be calculated to $\mathcal{O}(g^2)$,

$$
\begin{aligned}
J_i^q(m_J^2, p_{0,J_i}, R) &= \frac{(2\pi)^3}{2(p_{0,J_i})^2}\frac{\xi_\mu}{N_c\sqrt{2}}\sum_{\sigma,\lambda}\int\frac{d^3p}{(2\pi)^3 2\omega_p}\frac{d^3k}{(2\pi)^3 2\omega_k} \\
&\times \mathrm{Tr}\left\{\gamma^\mu \langle\, 0|q(0)\Phi_\xi^{(\bar{q})\dagger}(\infty,0)|p,\sigma;k,\lambda\,\rangle\, \langle\, p,\sigma;k,\lambda|\Phi_\xi^{(\bar{q})}(\infty,0)\bar{q}(0)|0\,\rangle\right\} \\
&\times \delta\left(m_J^2-(p+k)^2\right)\,\delta^{(2)}(\hat{n}-\hat{n}_{\vec{p}+\vec{k}})\,\delta(p_{0,J_i}-p^0-k^0), \qquad \text{(C.7)}
\end{aligned}
$$

where σ and λ denote the polarizations , and p and k the momenta of the final-state quark and gluon respectively with $\hat{n}_{\vec{p}+\vec{k}} \equiv \frac{\vec{p}+\vec{k}}{|\vec{p}+\vec{k}|}$. Similarly, for the gluon jet we have

$$
\begin{aligned}
J_i^g(m_J^2, p_{0,J_i}, R) &= \frac{(2\pi)^3}{4(p_{0,J_i})^3}\sum_{N_{J_i}}\int\frac{d^3p}{(2\pi)^3 2\omega_p}\frac{d^3k}{(2\pi)^3 2\omega_k} \\
&\times \langle\, 0|\xi_\sigma F^{\sigma\nu}(0)\Phi_\xi^{(g)\dagger}(0,\infty)\,|p,\sigma;k,\lambda\,\rangle\, \langle\, p,\sigma;k,\lambda|\Phi_\xi^{(g)}(0,\infty)\,F_\nu{}^\rho(0)\xi_\rho|0\,\rangle \\
&\times \delta\left(m_J^2-(p+k)^2\right)\,\delta^{(2)}(\hat{n}-\hat{n}_{\vec{p}+\vec{k}})\,\delta(p_{0,J_i}-p^0-k^0), \qquad \text{(C.8)}
\end{aligned}
$$

where p and k are the final state momenta within the cone size, R. To evaluate these matrix elements, we need the rules for vertices shown in Fig. C.1 for the field strengths. The double lines represent the perturbative expansion of the Wilson lines (C.5) in the ξ-direction (see Eq. (C.11)), whose vertices and propagators are shown in Fig. C.2. The resulting diagrammatic contributions to the quark and gluon jet functions at next-to-leading order are shown in Fig. C.3 and Fig. C.4 respectively.

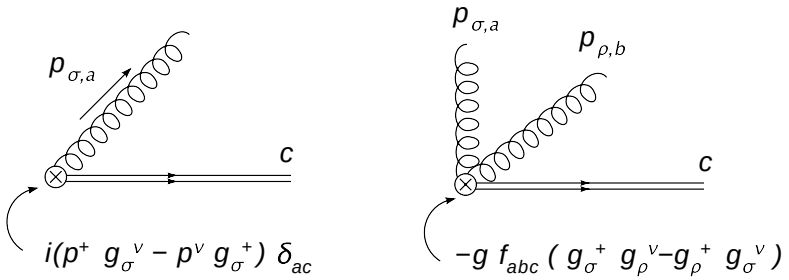

Figure C.1: Feynman rules associated with the $F^{+\nu}$ operator at the end of a Wilson line.

We choose a frame where the jet is in the $\eta_J = \phi_J = 0$ direction and the

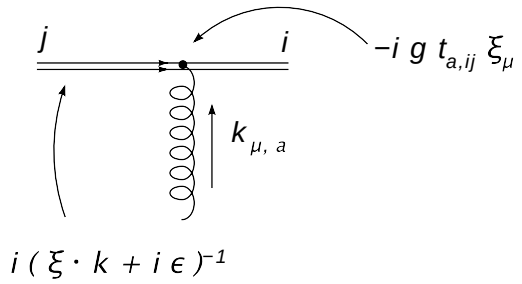

Figure C.2: Feynman rules associated with eikonal lines, from the expansion of the Wilson lines.

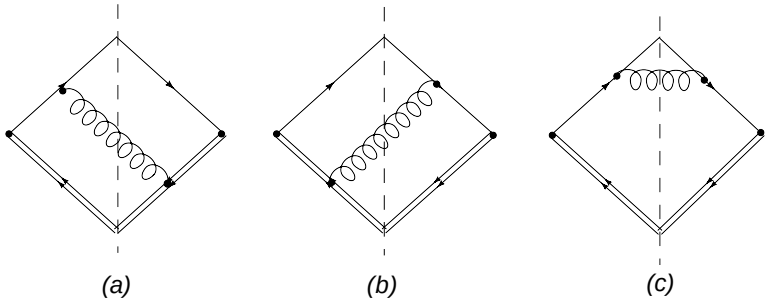

Figure C.3: Real contributions to the quark jet function at order α_s.

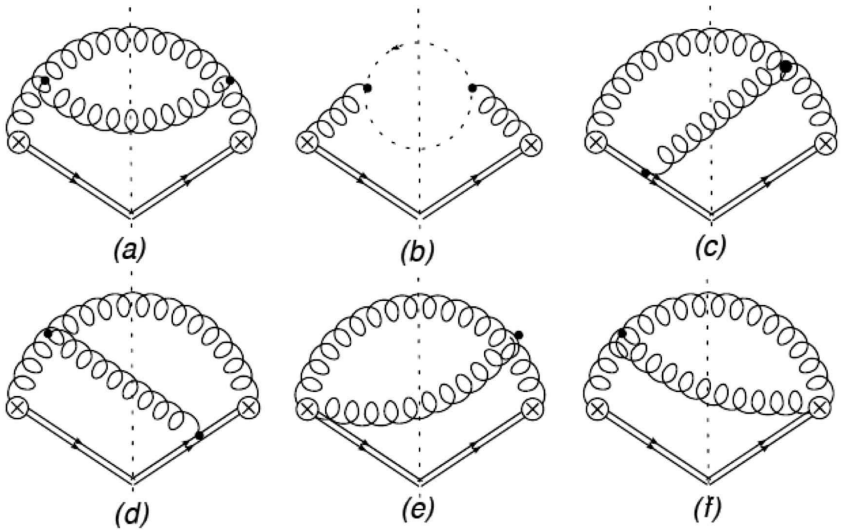

Figure C.4: Real non-vanishing contributions to the gluon jet function in Feynman gauge at NLO.

vector ξ is light-like and in a direction opposite to the jet,

$$p_{J_i} = p_{0,J_i}(1, \beta_i, 0, 0) \quad \xi = \frac{1}{\sqrt{2}}(1, -1, 0, 0)\,, \tag{C.9}$$

where $\beta_i = \sqrt{1 - m_{J_i}^2/p_{0,J_i}^2}$ is the velocity of the jet. In this frame we parametrize the momenta p and k above by

$$p = p^0(1, \cos\theta_p, \sin\theta_p, 0) \quad k = k^0(1, \cos\theta_k, -\sin\theta_k, 0)\,, \tag{C.10}$$

where $\theta_{p,k}$ represents the angle of each particle to the jet axis $\hat{n}$. The path ordered exponentials are expanded order-by-order in g_s, related to the rules in Fig. C.2 by the expansion,

$$\begin{aligned} \Phi_\xi(\infty, 0; 0) &= \mathcal{P}\left\{e^{-ig\int_0^\infty d\eta\, \xi\cdot A(\eta\xi^\mu)}\right\} \\ &= 1 - ig\int \frac{d^4k}{(2\pi)^4}\frac{i}{\xi\cdot k + i\epsilon}\xi\cdot A(k) + \dots\,. \end{aligned} \tag{C.11}$$

We begin with the calculation of the quark jet function, which readily

reduces to an integral over the energy and angle of one of the particles,

$$J_i^{q(1)}(m_J^2, p_{0,J_i}, R) = \frac{\beta_i}{8\sqrt{2}} \int \frac{d\cos\theta_k dk_0 k_0}{\pi(p_{0,J} - k_0)} |\mathcal{M}(p,k)|^2 \times \delta(m_j^2 - 2k^0 p_{0,J}(1 - \beta_i \cos\theta_k)) \Theta(R - \theta_k) \,, \quad \text{(C.12)}$$

where we choose k to represent the gluon and p the quark. For k the softer momentum, we easily see that $\theta_k \geq \theta_p$. Therefore, $p_0 = k_0$ fixes the minimum angle for the softest particle, and we find $\cos(\theta_{S,min}) = \beta_i$. The region $\omega_p < \omega_k$ is found by simply interchanging p and k in $|\mathcal{M}(p,k)|^2$ so that

$$J_i^{q(1)}(m_J^2, p_{0,J_i}, R) = \frac{\beta_i}{16\sqrt{2}} \int_{\cos(R)}^{\beta_i} \frac{d\cos\theta_S}{(2\pi)^2} \frac{m_{J_i}^2/p_{0,J}^2}{\left(2(1 - \beta_i \cos\theta_S) - \frac{m_{J_i}^2}{p_{0,J}^2}\right)} \times \frac{1}{p_{0,J}(1 - \beta_i \cos\theta_S)} \left(|\mathcal{M}_{q_i}(p,k)|^2 + |\mathcal{M}_{q_i}(k,p)|^2\right) \quad \text{(C.13)}$$

The evaluation of $|\mathcal{M}_{q_i}(p,k)|^2$ is straightforward from the diagrams of Fig. C.3, and we find

$$\begin{aligned} J_i^{q(1)}(m_J^2, p_{0,J_i}, R) &= \frac{C_F \beta_i}{4m_{J_i}^2} \\ &\times \int_{\cos(R)}^{\beta_i} \frac{d\cos\theta_S}{\pi} \frac{\alpha_s(k_0)\, z^4}{(2(1 - \beta_i \cos\theta_S) - z^2)\,(1 - \beta_i \cos\theta_S)} \\ &\times \left\{ z^2 \frac{(1 + \cos\theta_S)^2}{(1 - \beta_i \cos\theta_S)} \frac{1}{(2(1+\beta_i)(1 - \beta_i \cos\theta_S) - z^2(1 + \cos\theta_S))} + \right. \\ &\left. \frac{3(1+\beta_i)}{z^2} + \frac{1}{z^4} \frac{\left(2(1+\beta_i)(1 - \beta_i \cos\theta_S) - z^2(1 + \cos\theta_S)\right)^2}{(1 + \cos\theta_S)(1 - \beta_i \cos\theta_S)} \right\} \end{aligned} \quad \text{(C.14)}$$

where $z = \frac{m_{J_i}}{p_{0,J_i}}$, $p_{0,J_i} = \sqrt{m_{J_i}^2 + p_T^2}$, and $k_0 = \frac{p_{0,J_i}}{2} \frac{z^2}{1 - \beta_i \cos\theta_S}$.

The calculation of the gluon jet function proceeds along the same lines, with the exception that both particles in the final states are now identical, and the presence of the field strengths, which appear at the end of each Wilson line. The rules for these vertices, as mentioned before, are shown in Fig. C.1. Once again, we can write the gluon jet function as an integral over the angle of the

softer particle,

$$J_i^{g(1)}(m_J^2, p_{0,J_i}, R) = \frac{\beta_i}{16 m_{J_i}^2} \int_{\cos(R)}^{\beta_i} \frac{d\cos\theta_S}{(2\pi)^2 p_{0,J_i}^2} \times \frac{z^2}{(2(1-\beta_i\cos\theta_S) - z^2)\,(1-\beta_i\cos\theta_S)} |\mathcal{M}_{g_i}(p,k)|^2 \quad \text{(C.15)}$$

where $|\mathcal{M}_{g_i}(p,k)|^2$ is symmetric under the interchange of p and k. We find from the diagrams shown in Fig. C.4, the result

$$\begin{aligned} J_i^{g(1)}(m_J^2, p_{0,J_i}, R) &= \frac{C_A \beta_i}{16 m_{J_i}^2} \int_{\cos(R)}^{\beta_i} \frac{d\cos\theta_S}{\pi} \\ &\times \frac{\alpha_s(k_0)}{(1-\beta\cos\theta_S)^2(1-\cos^2\theta_S)(2(1+\beta)-z^2)} \\ &\times \big(z^4(1+\cos\theta_S)^2 + z^2(1-\cos^2\theta_S)(2(1+\beta_i)-z^2) \\ &+ (1-\cos\theta_S)^2(2(1+\beta_i)-z^2)^2\big)^2. \end{aligned} \quad \text{(C.16)}$$

These one-loop expressions have been used to generate the comparisons to event generator output given in Section 3.

Appendix D: R-dependence

It is of interest to isolate the leading logarithmic contributions in both gluon and quark jets, which can be found from eikonal graphs in the adjoint and fundamental representations respectively,

$$\begin{aligned} J^{(eik),c}(m_{J_1}^2, p_T, R) &= \frac{2\,C_c}{\sqrt{2}p_T} g^2 \int \frac{d^3k}{(2\pi)^3 2\omega_k} \frac{\xi\cdot p_J}{\xi\cdot k}\,\frac{\xi\cdot p_J}{2p_J\cdot k} \\ &\quad \times\delta\left(m_{J_1}^2-(p_1+k)^2\right)\Theta\left(p_T-k_T\right)\,. \end{aligned} \tag{D.1}$$

Parametrizing k as

$$k = k_T\left(\cosh\eta_k, \cos\phi_k, \sin\phi_k, \sinh\eta_k\right)\,, \tag{D.2}$$

this leads to

$$\begin{aligned} J^{(eik),c}(m_{J_1}^2, p_T, R) &= g^2\frac{C_c}{(2\pi)^3}\int dk_T\,k_T\,d\phi_k d\eta_k\,\frac{1}{k_T^2\left(\cosh^2\eta_k-\cos^2\phi_k\right)} \\ &\quad\times\delta\left(2p_T\,k_T\left(\cosh\eta_k-\cos\phi_k\right)-m_{J_1}^2\right)\Theta\left(p_T-k_T\right). \\ &= g^2\frac{C_c}{(2\pi)^3}\int d\phi_k d\eta_k\,\frac{1}{m_{J_1}^2}\frac{1}{k_T^2\left(\cosh^2\eta_k-\cos^2\phi_k\right)} \\ &\quad\times\delta\left(2p_T\,k_T\,r-m_{J_1}^2\right)\Theta\left(\cosh\eta_k-\cos\phi_k-\frac{m_{J_1}^2}{p_T^2}\right) \end{aligned} \tag{D.3}$$

In this expression we can change the variables to

$$\eta_k = r\cos\theta, \quad \phi_k = r\sin\theta\,. \tag{D.4}$$

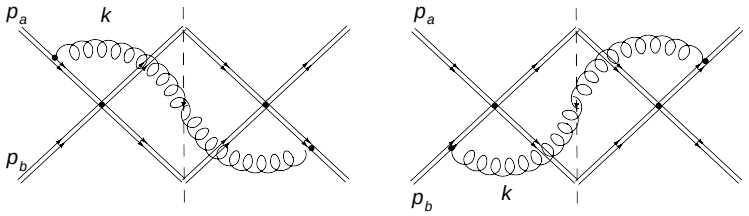

Figure D.1: Contributions to the jet mass from the soft function.

Since we are dealing with highly collimated jets we can expand the integrand in r and integrate over θ, finding

$$\begin{aligned} J^{(eik),c}(m_{J_1}^2, p_T, R) &\simeq g^2 \frac{2C_c}{(2\pi)^2} \int_{m_J/p_T}^{R} dr \, \frac{1}{m_{J_1}^2} \left\{ \frac{1}{r} + \mathcal{O}(r^3) \right\} \\ &\simeq \alpha_s(p_T) \frac{C_c}{m_{J_1}^2 \pi} \left\{ \log\left(\frac{R^2 \, p_T^2}{m_J^2} \right) + \mathcal{O}(R^4) \right\}, \end{aligned} \quad \text{(D.5)}$$

which shows explicitly the logarithmic behavior in R. Leading logarithmic contributions can be exponentiated, giving us a qualitative description of lower jet masses,

$$J^{(eik),c}(m_{J_1}^2, p_T, R) \simeq \frac{\alpha_s}{\pi} C_c \frac{1}{m_J^2} \log\left(\frac{R^2 p_T^2}{m_J^2} \right) \exp\left\{ -\frac{\alpha_s}{2\pi} C_c \log^2\left(\frac{R^2 p_T^2}{m_J^2} \right) \right\}. \quad \text{(D.6)}$$

Without the above approximations, the eikonal jet function is given by

$$J^{(eik),c}(m_J, p_T, R) = \alpha_s(p_T) \frac{4\, C_c}{\pi m_J} \log\left(\frac{p_T}{m_J} \tan\left(\frac{R}{2} \right) \sqrt{4 - \left(\frac{m_J}{p_T} \right)^2} \right). \quad \text{(D.7)}$$

As we have observed above, all R^0 behavior in the cross section can be found from the jet functions. We can also estimate the contribution of soft initial-state radiation on the cone-jet masses. Here we verify that such radiation is sub-leading in powers of R^2. Contributions due to wide angle gluons come from a "soft function" [21], which is defined in terms of an eikonal cross section,

$$S(m_{J_i}^2) \sim \sum_{N_s} \sigma^{(eik)}(N_s) \delta(m_{J_1}^2 - \tilde{m}_J^2(N_s, R)). \quad \text{(D.8)}$$

Diagrams that can contribute to the jet mass are illustrated in Fig. D.1. The

initial state radiation shown behaves as

$$S \sim \int d^4k\delta(k^2)\frac{p_a \cdot p_b}{(p_a \cdot k)(p_b \cdot k)}\delta(m_{J_1}^2 - 2p_1 \cdot k)\Theta(R - \tilde{R}(\eta_k, \phi_k))\,, \qquad \text{(D.9)}$$

with p_a and p_b the momenta of incoming partons, neither of which is in the direction of the observed jets. Choosing a frame where the initial momenta are given by

$$p_a = \frac{\sqrt{s}}{2}(1,0,0,1)\,, \quad p_b = \frac{\sqrt{s}}{2}(1,0,0,-1)\,, \qquad \text{(D.10)}$$

and parametrizing the radiated gluon's momentum k as in Eq. (D.2) above, we find

$$\begin{aligned} S &\sim \int dk_T d\phi_k d\eta_k \frac{1}{k_T}\frac{1}{2p_T(\cosh\eta_k - \cos\phi_k)}\delta\left(k_T - \frac{m_{J_1}^2}{2p_T(\cosh\eta_k - \cos\phi_k)}\right) \\ &\sim \frac{2\pi}{m_{J_1}^2}\int_0^R dr\, r = \frac{\pi R^2}{m_{J_1}^2}\,, \end{aligned} \qquad \text{(D.11)}$$

which is, as expected, power-suppresed in R compared to the logarithmic dependence we get from the jet function.